CONTROLLING SPIN-ORBIT TORQUES THROUGH STRONG CORRELATION

A Dissertation

Presented to the Faculty of the Graduate School

of Cornell University

in Partial Fulfillment of the Requirements for the Degree of

Doctor of Philosophy

by

Neal David Reynolds

August 2018

CONTROLLING SPIN-ORBIT TORQUES THROUGH STRONG CORRELATION

Neal David Reynolds, Ph.D.

Cornell University 2018

This dissertation discusses the generation and measurement of current-induced spin-orbit torques in $4f$ orbital systems. The first three chapters lay out the intuition for understanding the later experimental results and the required experimental considerations to generate data with robust interpretations. The second half discusses the measure of current-induced spin-orbit torques in four rare earth metals (Gd, Dy, Ho, and Lu) and the way in which the presence (or absence) of $4f$ orbital derived states at the Fermi level influences the torques generated. The final chapter discuses the non-trivial temperature evolution of the torques generated by a Kondo lattice system, $YbAl_3$, in light of the understanding gained from the study of the pure rare earth materials. Ultimately, it is argued that the measurement of current-induced spin-orbit torques may be a useful analytical tool for probing the Fermi surface of f-valent and heavy fermion systems.

BIOGRAPHICAL SKETCH

Neal Reynolds was born in Maryland during one of the more auspicious years, 1990. Under the auspices of being able to quickly calculate his current age, Neal made his way through school in growing up in a suburb on the outskirts of Baltimore city. Driven to succeed by his desire for bling, he filled his schedule in high school with as many advanced classes as possible in order to achieve the rank of valedictorian. Through much toil he achieved his dream and got to wear the valedictorian mantle. So tempered by the fires of academic rigor in high school, he sought a hotter crucible of learning for college to continue to be challenged. This lead him to Reed College in Portland, OR and the Reed Research Reactor Program in 2008. Driven by an uncompromising desire to learn, he undertook a chemistry and physics double major while working at the reactor as a Senior Reactor Operator. After Reed successfully finishing his undergraduate thesis on the spectroelectrochemistry of ZnSe quantum dots in 2012, Neal felt the need to finish the story and decided to apply to Cornell University to do a physic Ph.D. At Cornell University, he was fortunate to work for Prof. Daniel Ralph on what is the work contained herein.

This document is dedicated to whomever comes across it. I hope whatever search term led you to this document is suitably expounded upon in a manner that is useful. Also to my partner, Guen.

ACKNOWLEDGEMENTS

The number of people who have helped me reach this point are many. In roughly chronological order, I am particularly indebted to my family for their constant support. To my undergraduate thesis advisors, John Essick and Margaret Gesselbracht. To all of the chemistry, physics, and Reactor students at Reed college whose commiseration and enthusiasm helped me to flourish at Reed, specifically my thesis officemate, Nate Hermann, and my good friend, Wes Erickson. To Jay Ewing, for being down to PTL with a PSL and for offering so much sage advice. To Nate Ellis, the wise and benevolent ruler of the graduate machine shop for his invaluable assistance in making many of the parts that enabled this thesis and the parts that have lead me to give the world of wearable tech a try. To my lab mates, specifically Greg Stiehl, J.T. Heron, Dave Macneill, Marcos Guimarães, and Colin Jermaine whose advice and mentorship made me a better physicist. To my advisor, Dan Ralph, for being willing to put up with my shenanigans and offer sage advice. To my friends who have played so many board games with me and engaged in other crazy adventures and in particular Jordan, Jen, Alex, William, Matt, Azar. To my partner, Guen, for keeping me grounded and supporting me with my shenanigans. To everyone else with whom I have interacted, invariably I am lead to this point because of it. Cornell has been great. Would recommend.

TABLE OF CONTENTS

LIST OF TABLES

LIST OF FIGURES

CHAPTER 1

INTRODUCTION

The story of this dissertation is the story of the Berry curvature, of peering into the mess of spaghetti that is a band structure and trying to divine meaning. In less lofty terms, this dissertation is a discussion of the origin of torques acting upon a magnet arising from the application of an electric field to a different material next to said magnet. These so-called "spin transfer torques" can be used to precisely control the orientation of the magnetization of nanomagnets much more efficiently and locally than switching through the generation of a magnetic field from an electric current alone. As such, the understanding and generations of these torques is of immense practical relevance for new memory applications and computational paradigms[1–3].

Indeed, many papers [4–13] open with their introduction stating similar to the above. It is a fine motivation, and a pragmatic one too. However, I will leave it to those references to titillate those who pine after concrete utility. In this author's view, the field is sufficiently far advanced that the study of these spin orbit torques can be interesting enough for their own right. In particular, the spin-orbit torques generated by the spin Hall effect (torques generated by spin accumulations at interfaces transverse to an applied electric field) can be understood as a potentially deep statement about the electronic structure of generating material. The details of how and why this is the case will be covered at length in the following chapters, but given that spin Hall effect reflects the electronic structure of a material, this potentially offers a new avenue for the spin Hall effect measurements as analytical tool for probing the Fermi surface in addition to being an effect useful for technological ends. It is under this aegis that the story of this Ph.D. is cast. Specifically, I will cover measurements two measurements of the spin Hall effect in systems with novel electronic structures. The first experiment in the pure rare earth metals serves as corrob-

oration of the utility of the spin Hall effect as a probe of electronic structure and in particular $4f$ orbital states. The second experiment on $YbAl_3$ extends this result to a system with possessed of Kondo lattice that alters the Fermi surface as function of temperature in a characteristic way.

In the following chapter, the physics behind the intuition one may gain about the spin Hall effect from a band structure is laid out in pedantic detail. First I discuss origin of the "intrinsic" spin Hall effect as the anomalous velocity that arises due to the Berry curvature and comment on the "extrinsic" spin Hall effect for completeness. With intuition as to the origin of the spin Hall effect I move to discussing features observable in electronic structures to gain intuition for the spin Hall effect as an analytical tool especially in light of the symmetry of the system.

The third chapter focuses on the intricacies of the actual measurement of the spin Hall effect. It is not necessarily straightforward to measure electron spin and such measurements are complicated further by the necessity of performing these experiments at cryogenic temperatures to examine the evolution of the electronic structure. To overcome these challenges we will use several techniques to confirm our results. Specifically, I will cover spin torque-ferromagnetic resonance (ST-FMR) and direct imaging of the magnetization with the magneto-optical Kerr effect (MOKE).

The fourth chapter details the combined theoretical and experimental room temperature measurements of the spin Hall effect in four late rare-earth metals (Gd, Dy, Ho, and Lu). Through this experiment and the theoretical calculations we come to understand the strong effect that $4f$ states have on the band structure. The excellent qualitative agreement between the trend of the experimental measurements and theoretical calculation of the spin Hall effect vs element also reveals the potential utility of the spin Hall effect for validating theoretical calculations of strongly correlated strongly correlated $4f$ physics.

The fifth chapter extends the results of the rare earth study to an experimental study of a heavy fermion system, $YbAl_3$, in which the strength of the $4f$ orbital interaction at the Fermi level can be tuned with temperature owing to the strong correlations between the local Yb $4f$ moments. Our preliminary results reveal a scaling of the spin Hall effect with temperature consistent with the scaling of the $4f$ orbital hybridization at the Fermi level measured via angle-resolved photoemission spectroscopy. This agreement suggests a similar origin and offers a new experimental signature against which theoretical explanations may be potentially be verified. Beyond this characteristic temperature scaling, we also find evidence of current induced spin orbit torques with symmetry beyond the semiclassical interpretation of the spin Hall effect that are nominally forbidden by the crystal symmetry (Neumann's principle).

This document is meant to pedantic. It is my wish that it be mostly self-contained and accessible to a first year graduate student.

CHAPTER 2

THEORY

This chapter is meant to be a self contained review of the physics relevant to understand the story that I will tell later to understand the behavior observed in the systems I have studied. I have endeavored to make it accessible and explicit.

2.1 The Spin Hall Effect

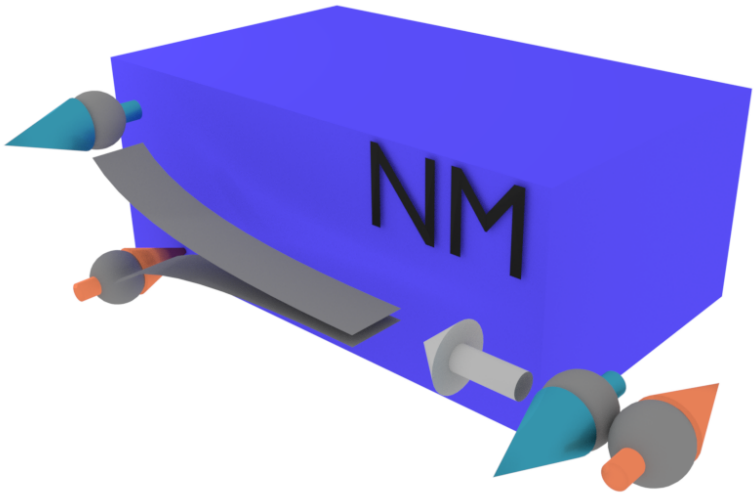

Figure 2.1: A schematic representation of the spin Hall effect in a normal (*i.e.* non-magnetic) material. Electrons driven by an electric field are deflected in opposite directions according to their spin.

To begin, let us consider a rectangular bar of some non-magnetic[1] material in the ab-

[1]This restriction of non-magnetic is not to say the same physics isn't present in magnetic materials, it is. However, because the spin populations are unequal in a magnet, the associated physics gives rise to the anomalous Hall effect (*i.e.* a net flow of charge). The spin polarization of the anomalous Hall current is also

sence of any external magnetic field. If we apply an electric field along one axis of this bar, electrons with opposite spins may be deflected in opposite directions transverse to the applied electric field. Because there is an equal amount of all spin populations, this flow of angular moment is not associated with a net flow of charge resulting in a *pure spin current*. In the simplest case, the direction of those spins will be perpendicular to the electric field and the direction the electron is deflected in what as known as the spin Hall effect (Fig. 2.1).[2] This effect was first predicted over 45 years ago by Dyakonov and Perel[15] and then later rediscovered by Hirsch in 1999[16] as an extension of the theory of anomalous Hall effect generation in magnets[17–21] to non-magnetic materials. As with the anomalous Hall effect, the origin of the spin Hall effect is intimately tied to spin orbit coupling and can be *intrinsic*, arising from the shape of the electronic structure of the material itself, or *extrinsic*, arising from asymmetric spin-dependent scattering off of impurities. Both intrinsic and extrinsic effects are likely present in all materials to some degree, and it is not necessarily clear which will dominate in a given system.

Historically, the community has reported the strength of the spin Hall effect as dimensionless ratio of the spin Hall conductivity to the charge conductivity with a factor of $\frac{\hbar}{2e}$ to convert the dimensions of spin Hall conductivity from angular moment flow to charge flow. Again with analogy to the anomalous Hall effect this ratio has been ascribed the letter θ or α and called the spin Hall angle. It is really the tangent of the "spin Hall angle" but the first materials studied had spin Hall effects sufficiently small that the small angle approximation $\tan\theta \approx \theta$ was still valid[22–32]. More recently, reports of larger spin Hall ratios such as -0.33 in the β form of W[9] and greater than one in the topological insulator Bi_2Se_3[33] meaning that even the semblance of an excuse for calling the spin Hall ratio an angle is no longer valid. Rather, the field (the author included[34]) is shifting towards

somewhat murky owing to the likely precession of the component of the spin current perpendicular to the magnetization around the internal magnetic field[14].

[2]Other directions of spins may be allowed in certain cases, and this possibility will be discussed at the end of the chapter.

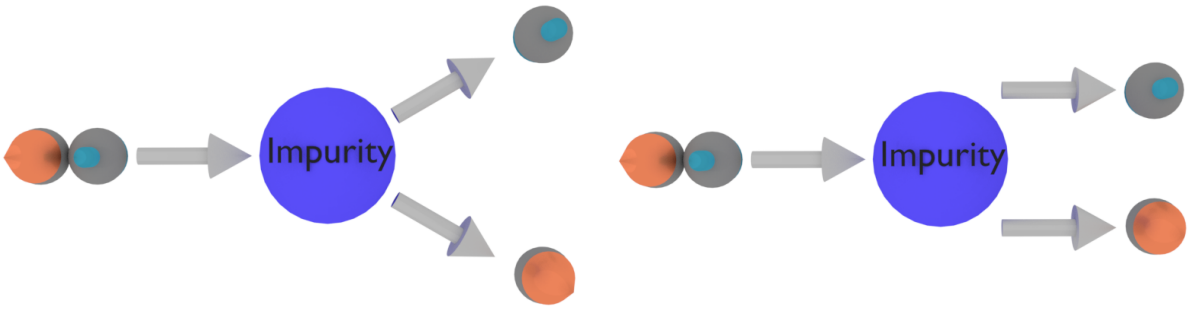

Figure 2.2: Schematic representation of the two processes giving rise to the extrinsic spin Hall effect: skew scattering (left) and side jump scattering (right).

calling the ratio what it really is, an efficiency of charge to spin current conversion. On top of this there is also the note that what the experimentalist measures as the spin Hall effect is actually not the whole spin Hall effect, the actually charge to spin current efficiency is reduced by the transparency of the interface, T. What is typically report then is given and using the symbol ξ.

Semantics aside, how does each effect arise?

2.2 Extrinsic Spin Hall Effect

The extrinsic spin Hall effect arises from two types of asymmetric spin scattering off of impurities[21], skew scattering[18, 19] and side-jump scattering[20]. Neither of these effects are particularly intuitive. Skew scattering, however, seems the more intuitive to understand of the two as it is looks like a classical scattering process. An electron comes in with wavevector, $\vec{k}$, and is scattered into some other wavevector, $\vec{k}'$, at some angle with respect $\vec{k}$ (schematically illustrated in Fig. 2.2). Owing to spin-orbit coupling,[3] the scattering cross section is spin-dependent with opposite spins being scattered into oppo-

[3] In the sense that one can think of the electron passing by the approximately spherical potential of the impurity and feeling an effective magnetic field in its reference frame.

site θ's. Side-jump scattering (schematically illustrated in Fig. 2.2) is a bit more nuanced. It turns out that spin-orbit coupling may also cause a shift of the wavepacket perpendicular to the incident direction which is also spin dependent[20]. Quantum mechanically, the origin of the effect is the movement of a wavepacket through the scattering potential introduces a time delay in the phase of component of the wavefunction perpendicular to the incident direction. Phrased more suggestively, the scattering potential makes it seem like more or less time has elapsed in directions perpendicular to $\overrightarrow{k}$ than parallel to $\overrightarrow{k}$. Thus if t=0 at the scattering event, then already the perpendicular component has a phase $e^{iE\Delta t}$ which is equivalent to already having traveled in the perpendicular direction.

In order to distinguish between the two effects, we note that the resulting spin Hall conductivity from skew scattering, σ_{sk} and from side jump scattering, σ_{sj} have different temperature dependences. σ_{sk} scales as $\propto \rho^{-1}$[21, 35] (where ρ is the resistivity of the material and will typically vary with temperature). Because skew scattering is fairly analogous to a classical scattering process we may understand this temperature dependence as a statement about how far the electron travels with its new trajectory after being skew scattered. If the resistivity is lower then the electron will maintain its skew-scattered trajectory containing a component perpendicular to the applied electric field for longer before the electron gets scattered into some other angle by another process which is not necessarily going to be a skew scattering event (phonon scattering or electron-electron scattering, for instance). The longer the skew scattered trajectory is maintained, the more perpendicular displacement the electron accrues. This argument does not apply to side jump scattering. The total perpendicular displacement as a result of side jump scattering happens immediately as a result of the scattering event and so in the clean limit there is no dependence of on the resistivity, (*i.e.* $\sigma_{sj} \propto \rho^0$). If, however, the sample is very resistive, $\sigma_{sj} \propto \rho^{-2}$[21, 36]. The intuition for this is less classical but nonetheless attainable: If the sample is very resistive then the lifetime of the quasi-particles that make up the excita-

tions on the Fermi surface becomes very short. Owing to the uncertainty principle, this has the effect increasing the uncertainty of the energy of the quasi-particle as well. Thus if the quasiparticle life time $\tau_{qp} \leq \Delta t$ then the phase of the perpendicular component in the previous paragraph $e^{iE\Delta t}$ gets smeared energy and the relevance of the time Δt reduced, giving us two factors of ρ.

Both of these effects are maximized if there is strong spin-orbit coupling present and the host element and impurity have dramatically different potentials (*i.e.* light element in a heavy host or heavy element in a light host)[37]. This is why large spin Hall effects have been observed in materials systems such as Bi-doped copper [38] or Ir-doped copper[39]. Because of this sensitivity to the dopant and host elements, one could imagine probing the electronic structure of the host by changing the dopant in a given host. However, one is limited to the space of accessible elements, thermodynamic considerations, and the patience of the experimentalist to fabricate such a series of different samples. Thus it is not through the extrinsic spin Hall effect that we will carry out the suggested program of probing the electronic structure of a material through the spin Hall effect. No, it will be through the intrinsic spin Hall effect.

2.3 Intrinsic Spin Hall Effect

The intrinsic spin Hall effect is statement about the electronic structure of the material at its Fermi level. In particular, it is convenient[4] to think of the intrinsic spin Hall effect as the integrated Berry curvature of the Fermi surface. But just what exactly is the Berry curvature? In 1984, Michel Berry sought to upturn conventional wisdom by commenting on the nature of the phase of a wave function if it dragged through a parameter space[40].

[4]But not entirely correct

The conventional wisdom had been asserted by Fock[5] was that even though this sojourn through parameter space does give rise to a phase, the dynamical phase we all know well from the solution to the time dependent Schröedinger equation, it doesn't matter. Or, rather, it's unobservable. A suitable choice of gauge can make the wavefunction appear as though it had not actually endeavored on its trip.

Berry's luminous insight was to ask what would happen if we consider returning to the same place after our walk through parameter space, is there a phase we can't gauge away? Put another way, his question was "does the wavefunction have any memory of its trip?" The answer is maybe. Berry found that we pick up an extra phase that cannot be entirely gauged away, it must be there up to a multiple of 2π. This so-called "geometric" phase is gauge invariant[6], which means that it's going to have an effect on systems. It turns out that the curl of what is integrated to get the phase is also gauge invariant. This so-called "Berry curvature" will turn out to be what interests us most in the context of condensed matter systems. In order for this document to be self contained, a derivation of the Berry phase is warranted. I prefer the notation given in [41], but the ultimate responsibility for its elegance comes from Berry's original paper[40].

2.3.1 Berry('s) Phase

Consider a Hamiltonian H($\mathbf{R}$) that depends on some parameter $\mathbf{R}(t)$ which is evolving in time. At every time t and assuming that we have a discrete spectrum of states, we thus have the eigenvalue problem

$$H(\mathbf{R})|\psi_n(t)\rangle = E_n|\psi_n(t)\rangle \tag{2.1}$$

[5]This assertion is the one made in [41]. I'll give you the citation for the paper that [41] cites: V. Fock, *Zeritschrift fuer Physik* **49**, 323 (1928), but it's in german and I am content to take [41] at his word

[6]and thus observable

If we imagine that the evolution of $|\psi_n(\mathbf{R}(t))\rangle$ is adiabatic[7], then at every time t the system will remain in the same eigenstate it was initially prepared in.

Now we ask, "what happens to it's phase?" Of course we are going to have the 'dynamical' phase due to the fact the state has energy and time has passed. We are also allowed a phase due to the freedom we are allowed in choosing a gauge so we should include that as well to make sure we capture all of the physics. This gives

$$|\psi(t)\rangle = e^{\frac{-i}{\hbar}\int_0^t dt' E_n(\mathbf{R}(t'))} e^{i\gamma(t)} |\phi_n(\mathbf{R}(t'))\rangle \tag{2.2}$$

If we then insert Eqs. 2.2,2.1 into the time-dependent Schrödinger equation

$$H(\mathbf{R})|\psi(t)\rangle = i\hbar|\dot{\psi}(t)\rangle \tag{2.3}$$

(where a dot denotes a time derivative) and move the $i\hbar$ to the other side, we get

$$\begin{aligned} \frac{-i}{\hbar} E_n(\mathbf{R})|\psi(t)\rangle = e^{\frac{-i}{\hbar}\int_0^t dt' E_n(\mathbf{R}(t'))} e^{i\gamma(t)} \times & \qquad (2.4) \\ \left(\frac{-i}{\hbar} E_n(\mathbf{R})|\phi_n(t)\rangle + i\dot{\gamma}|\phi_n(\mathbf{R}(t))\rangle + \partial_t|\phi_n(\mathbf{R}(t))\rangle\right) & \\ -i\dot{\gamma}|\phi_n(\mathbf{R}(t))\rangle = \frac{\partial}{\partial t}|\phi_n(\mathbf{R}(t))\rangle & \\ \dot{\gamma} = i\langle\phi_n(\mathbf{R}(t))|\frac{\partial}{\partial t}|\phi_n(\mathbf{R}(t))\rangle & \qquad (2.5) \end{aligned}$$

At this point, Berry's insight was to ask what happens if we come back to the same point as we started at some time T, what is the total phase we accrue? To set things up we note that $\frac{\partial}{\partial t}$ is $\frac{\partial}{\partial \mathbf{R}}\frac{\partial \mathbf{R}}{\partial t}$ or, in three dimensions, $\nabla_{\mathbf{R}}\dot{\mathbf{R}}$ giving

$$\dot{\gamma} = i\langle\phi_n(\mathbf{R}(t))|\nabla_{\mathbf{R}}|\phi_n(\mathbf{R}(t))\rangle\dot{\mathbf{R}} \tag{2.6}$$

[7] i.e. that $\mathbf{R}$ doesn't vary too quickly with t and that there are no degenerate states in our walk through the parameter space $\mathbf{R}$

Then

$$\gamma = i \int_{t=0}^{t=T} \langle \phi_n(\mathbf{R}(t'))|\nabla_{\mathbf{R}}|\phi_n(\mathbf{R}(t'))\rangle \dot{\mathbf{R}}\, dt' \tag{2.7}$$

$$= i \oint \mathrm{A}(R) d\mathbf{R} \tag{2.8}$$

$$\mathrm{A}(R) \equiv \langle \phi_n(\mathbf{R})|\nabla_{\mathbf{R}}|\phi_n(\mathbf{R})\rangle \tag{2.9}$$

where A(R) is the so-called Berry connection.[8]

We can't gauge this γ away. We predicated this whole derivation on the notion that we were doing the parameter space walk adiabatically. If $\mathbf{R}(0)$=$\mathbf{R}$(T), our wavefunction better be the same as it was when we started or else it won't be single valued. Now, we can throw around factors of 2π all day, but we can't rightly get rid of this accrued phase. Furthermore, γ is gauge invariant so it should be observable.[9] So, where did it come from?

To quote the paper that started it all[40],

> "In general one may expect such effects whenever an isolated system is considered as being divided into two interacting parts, each slaved to a different aspect of the other (in the molecular case, electron states are slaved to nuclear coordinates, and nuclear states are slaved to the electronic states and wavefunctions)."

This is an important and subtle point. The effects that can be described by the Berry phase are not overtly mysterious. In a full quantum mechanical treatment of the system, they

[8]Note that A($\mathbf{R}$) must be purely imaginary so that γ is purely real or else we would be leaking probability. One important implication is the identity $\langle \phi_m(\mathbf{R})|\nabla_{\mathbf{R}}|\phi_n(\mathbf{R})\rangle \equiv \langle \phi_n(\mathbf{R})|\nabla_{\mathbf{R}}|\phi_m(\mathbf{R})\rangle^* = -\langle \phi_n(\mathbf{R})|\nabla_{\mathbf{R}}|\phi_m(\mathbf{R})\rangle$

[9]The same is not true of A(R). This makes some sense in that a gauge change results in a change of our boundary conditions. When we integrate around the closed loop we encounter the shifted boundary conditions in addition to the changed A(R) and the sum of both ultimately gives us the same γ

would be predicted. It is when we make simplifying approximations in our treatment of quantum mechanical systems that reduce complexity that we pick up this extra phase. In that sense, then, the Berry phase is a manifestation of the interactions of all of the other states we have neglected in our simplified picture that would have otherwise influenced whatever we are calculating if we did a full non-simplified treatment. It is also somewhat miraculous that it's this easy that those states we neglect enter in this easily. The Berry phase affords us a convenient way to describe more fully the system under consideration while making use of the assumptions we have historically made to make systems computationally tractable.

2.4 Implications

Because of the nature of when the Berry phase shows up is so common in physics, many effects described in other ways are easily recast in terms of the Berry phase. Examples of this include an unambiguous calculation of the electric polarization [42, 43], and an explanation of the anomalous velocities in the semiclassical theory of electrons transport that arise in ferromagnetic metals[44]. The Berry phase effects in 3D non-magnetic metals with inversion symmetry are in what we are most interested as that is what gives rise to the intrinsic spin Hall effect. To see how we get there, we need to do a bit more math.

2.4.1 Wave Packet dynamics

Let us consider the motion of an electron wave packet in a crystal composed of some collection of frequencies defined by an envelope function $a(k,t)$ [41, 45]:

$$|w_o\rangle = \int_{BZ} d\mathbf{k} a(\mathbf{k},t)|\psi_{n,\mathbf{k}}(\mathbf{r},t)\rangle \tag{2.10}$$

We would like our wave packet to be pretty tightly focused in k space so we can make reasonable statements about how fast it is moving so we require

$$\overrightarrow{k_c} = \int_{BZ} d\mathbf{k}|a(\mathbf{k},t)|^2\mathbf{k} \tag{2.11}$$

$$\approx \int_{BZ} \delta(\mathbf{k}-\mathbf{k}_c)\mathbf{k}d\mathbf{k} \tag{2.12}$$

The price we pay is that our wave packet will, by uncertainty, be pretty distributed in space. This means that if we want to make statements about semiclassical motion we should restrict ourselves to fields that vary on long length scales. Now we would like to know where we expect to find the center of our wave packet in real space, given our demands on $a(\mathbf{k},t)$. I present the derivation in all its gory detail because I could not find it laid out in this level of detail anywhere else and I want this document to be as transparent as possible.

$$\begin{aligned} r_c &\equiv \langle w_0|r|w_0\rangle \\ &= \int_{\mathbf{k}'}\int_{\mathbf{k}} d\mathbf{k}' \, d\mathbf{k} a^*(\mathbf{k}',t)\langle\psi_{n,\mathbf{k}'}|r|\psi_{n,\mathbf{k}}\rangle a(\mathbf{k},t) \end{aligned}$$

[Invoking the definition of Bloch states]

$$= \int_{\mathbf{k}'\in BZ}\int_{\mathbf{k}\in BZ} d\mathbf{k}' \, d\mathbf{k} \, a^*(\mathbf{k}',t)\,\langle u_{n,\mathbf{k}'}|e^{-i\mathbf{k}'\cdot\mathbf{r}} r e^{i\mathbf{k}\cdot\mathbf{r}}|u_{n,\mathbf{k}}\rangle a(\mathbf{k},t)$$

[Since $\frac{\partial}{\partial\mathbf{k}}e^{-i(\mathbf{k}'-\mathbf{k})\cdot\mathbf{r}} = \frac{r}{i}e^{-i(\mathbf{k}'-\mathbf{k})\cdot\mathbf{r}}$]

$$= -i\int_{\mathbf{k}'\in BZ}\int_{\mathbf{k}\in BZ} d\mathbf{k}' \, d\mathbf{k} \, a^*(\mathbf{k}',t)\,\langle u_{n,\mathbf{k}'}|\left[\frac{\partial}{\partial\mathbf{k}}e^{-i(\mathbf{k}'-\mathbf{k})\cdot\mathbf{r}}\right]|u_{n,\mathbf{k}}\rangle a(\mathbf{k},t)$$

[Integrating by parts to get the $\frac{\partial}{\partial\mathbf{k}}$ off of the exponential]

$$= i\int_{\mathbf{k}'\in BZ}\int_{\mathbf{k}\in BZ} d\mathbf{k}' \, d\mathbf{k} \, a^*(\mathbf{k}',t)\,\langle u_{n,\mathbf{k}'}|e^{-i(\mathbf{k}'-\mathbf{k})\cdot\mathbf{r}}\frac{\partial}{\partial\mathbf{k}}\left[|u_{n,\mathbf{k}}\rangle a(\mathbf{k},t)\right]$$

[Noting $e^{-i(\mathbf{k}'-\mathbf{k})\cdot\mathbf{r}}$ is a delta function and doing the $\mathbf{k}'$ integral]

$$
\begin{aligned}
&= i\int_{\mathbf{k}\in BZ} d\mathbf{k}\,|a(\mathbf{k},t)|^2\frac{1}{a(\mathbf{k},t)}\,\langle u_{n,\mathbf{k}}|\frac{\partial}{\partial\mathbf{k}}\left[|u_{n,\mathbf{k}}\rangle a(\mathbf{k},t)\right]\\
&= i\int_{\mathbf{k}\in BZ} d\mathbf{k}\,|a(\mathbf{k},t)|^2\frac{1}{a(\mathbf{k},t)}\,\langle u_{n,\mathbf{k}}|\left[a(\mathbf{k},t)\frac{\partial}{\partial\mathbf{k}}|u_{n,\mathbf{k}}\rangle + \frac{\partial a(\mathbf{k},t)}{\partial\mathbf{k}}|u_{n,\mathbf{k}}\rangle\right]\\
&= i\,\langle u_{n,\mathbf{k}_c}|\frac{\partial}{\partial\mathbf{k}_c}|u_{n,\mathbf{k}_c}\rangle + i\int_{\mathbf{k}\in BZ} d\mathbf{k}\,\frac{1}{a(\mathbf{k},t)}\frac{\partial a(\mathbf{k},t)}{\partial\mathbf{k}}\langle u_{n,\mathbf{k}_c}|u_{n,\mathbf{k}}\rangle\\
&= \underbrace{i\,\langle u_{n,\mathbf{k}_c}|\frac{\partial}{\partial\mathbf{k}_c}|u_{n,\mathbf{k}_c}\rangle}_{\equiv\text{Berry connection, A}(\mathbf{k})} + i\int_{\mathbf{k}\in BZ} d\mathbf{k}\,\frac{\partial\ln(a(\mathbf{k},t))}{\partial\mathbf{k}}\\
&= \mathrm{A}(\mathbf{k}) + i\int_{\mathbf{k}\in BZ} d\mathbf{k}\,\frac{\partial\ln(|a(\mathbf{k},t)|e^{i\arg(a(\mathbf{k},t))})}{\partial\mathbf{k}}
\end{aligned}
$$

[Again making use of the fact that $a(\mathbf{k},t)$ is very localized]

$$
\begin{aligned}
&= \mathrm{A}(\mathbf{k}) + i\,\frac{\partial\ln(e^{i\arg(a(\mathbf{k},t))})}{\partial\mathbf{k}}\bigg|_{\mathbf{k}=\mathbf{k}_c}\\
&= \mathrm{A}(\mathbf{k}) - \frac{\partial}{\partial\mathbf{k}}\arg(a(\mathbf{k},t))\bigg|_{\mathbf{k}=\mathbf{k}_c}
\end{aligned}
$$

It is then at this point that the presence of the Berry phase effects are made manifest, but how did they get there? We sealed our fate when we invoke Bloch's theorem.

It's clear in symbols that's when that devilish $\mathbf{k}$ derivative entered our equations. More abstractly, invoking Bloch's theorem allowed us to narrow our focus from the ostensibly infinite crystal to just the unit cell. Unfortunately, as [41] puts it, in doing this we traded "in a huge Hilbert space for a multitude of little ones" indexed now by $\mathbf{k}$, each with their own boundary conditions. To deal with the $\mathbf{k}$-dependent boundary conditions we explicitly include it in the states themselves via a unitary transformation, $e^{i\mathbf{k}\cdot\mathbf{r}}$. The price we pay is that we also have to transform our Hamiltonian, Eq. 2.13 [41]

$$H(\mathbf{k}) = e^{-i\mathbf{k}\cdot\mathbf{r}}He^{i\mathbf{k}\cdot\mathbf{r}} \tag{2.13}$$

$$\implies \left[\frac{1}{2m}(\mathbf{p}+\hbar\mathbf{k})^2 + V(\mathbf{r})\right]u_{n,\mathbf{k}}(\mathbf{r}) = E_n(\mathbf{k})u_{n,\mathbf{k}}(\mathbf{r}) \tag{2.14}$$

and as a result of this transformation our Hamiltonian now has explicit **k** dependence (Eq. 2.14). As the earlier quote from Berry's original paper points out that is when we an expect Berry phase effects to come up.

To see how this Berry connection[10] manifests itself as an observable quantity we continue in our semiclassical approach and derive the equations of motion for the wave packet under the influence of applied electric and magnetic fields. As is the case in the semiclassical treatment, the magnetic field enters in the Hamiltonian as the so-called Peierls substitution[46] wherein we replace the momentum operator $\hat{P}$ with the canonical momentum operator $[\hat{P} + eA(\mathbf{r}, t)/c]$ where $A(\mathbf{r}, t)$ is the magnetic vector potential. In what was a poor choice of notation, one must be careful not to mix this up with A(**k**), the Berry connection. The static electric field enters as a scalar potential $eV(\mathbf{r})$. This gives us our Hamiltonian

$$\hat{H} = \frac{1}{2m}\left[\hat{P} + \frac{eA(\mathbf{r}, t)}{c}\right]^2 + U(\mathbf{r}) - eV(\mathbf{r}) \tag{2.15}$$

Concerns may be raised about the scalar potential breaking translational symmetry. I prefer the phrasing of [45] on the matter, "Because the focus is on wave packets, which are localized in space, one does not have to worry about the impossibility of incorporating the scalar potential rigorously into periodic boundary conditions." We want to figure out equations of motions so we should form a Lagrangian and then minimize the action[41, 45, 47].

$$L = \langle W | i\hbar \frac{\partial}{\partial t} | W \rangle - \langle W | \hat{H} | W \rangle \tag{2.16}$$

The actual calculation of L and application of the Euler-Langrange equations is tedious and unenlightening. We play more of the same games that we played in figuring out where r_c above and nothing too deep can be gleaned from the vector calculus. All the

[10] Recall from a previous footnote A(R) is not gauge invariant and is thus not observable

interesting physics happened when we decided to include a vector and scalar potential to mess with our wave packet, the rest is just turning the crank. For those who enjoy the mechanical advance of geared systems, I refer you to Chapter 16 of [45], pages 17-19 of [41], and page 1981 of [47].

Ultimately we get

$$\hbar\dot{\mathbf{k}}_c = -e\mathbf{E}(\mathbf{r}_c) - e\dot{\mathbf{r}}_c \times \mathbf{B}(\mathbf{r}_c) \tag{2.17}$$

$$\dot{\mathbf{r}}_c = \frac{1}{\hbar}\frac{\partial}{\partial \mathbf{k}_c}\left[E_n(\mathbf{k}_c) + \frac{e}{2m}\mathbf{B}(\mathbf{r}_c)\cdot \mathbf{L}_n(\mathbf{k}_c)\right] - \dot{\mathbf{k}}_c \times \Omega_n(\mathbf{k}_c) \tag{2.18}$$

where $\mathbf{E} = \nabla V$, $\mathbf{B} = \nabla \times A$, $\mathbf{L}_n(\mathbf{k}_c)$ is the orbital magnetic moment of the wave packet, and Ω_n is the Berry curvature given by

$$\Omega_n \equiv \nabla_{\mathbf{k}} \times \mathrm{A}_n(\mathbf{k}) \tag{2.19}$$

$$= \left\langle \frac{\partial u_{n,\mathbf{k}}}{\partial_{\mathbf{k}}}| \times |\frac{\partial u_{n,\mathbf{k}}}{\partial_{\mathbf{k}}} \right\rangle \tag{2.20}$$

$\mathbf{L}_n(\mathbf{k}_c)$ is interesting in its own right–it is also a property that arises from Berry phase effects–but for the purposes of understanding the spin Hall effect it is not the most interesting.[11] We are more interested in the term that arises due to the Berry curvature as it give us motion of the center of the wave packet that is traverse to the applied electric field.[12] This term is ultimately the origin of the spin Hall effect in this formalism.

We'll get to actually calculating the spin Hall effect in a later section, but right now it behooves us to massage Eq. 2.20 using the relation from footnote 4 and the Feynman-Hellman theorem. Eq. 2.20 then becomes [41, 47, 48]

$$\Omega_{\mathbf{n}} = \sum_{m\neq n} \frac{\left\langle u_{n,\mathbf{k}}|\frac{\partial H}{\partial_{\mathbf{k}}}|u_{m,\mathbf{k}}\right\rangle \times \left\langle u_{m,\mathbf{k}}|\frac{\partial H}{\partial_{\mathbf{k}}}|u_{n,\mathbf{k}}\right\rangle}{(E_n - E_m)^2} \tag{2.21}$$

[11] As we can see in Eq. 2.18, $\mathbf{L}_n(\mathbf{k}_c)$ serves to mess with longitudinal transport given the application of a magnetic field.

[12] Ω_n's appearance in the equation for an observable also serves to highlight the fact that Ω_n must be gauge invariant–it would otherwise be unobservable.

This massaging does two things. The first is offer a much more tractable way of calculating the Berry curvature numerically, by putting the derivative on the Hamiltonian we can take an analytical derivative and then evaluate at a given k point. Having the derivative on the Bloch states themselves would require taking a numerical derivative, a much less fun computational task. The second thing is to recast the Berry curvature in a manner that makes manifest its origin. Eq. 2.21 has its largest contributions when there are states nearby in energy. That proximity in energy allows them to interact strongly with the state we are considering and so, again, the Berry curvature is a measure of the residual interactions with other states that our simplified picture would have otherwise neglected.

2.4.2 The Effect of Symmetry

One last critical point we need to consider is the requirement placed on the Berry curvature based on the symmetries of the system[47]. Focusing on Eq. 2.18, we note that under time reversal symmetry $\dot{\mathbf{r}} \to -\dot{\mathbf{r}}$ and $\mathbf{k} \to -\mathbf{k}$ while $\mathbf{E}$ remains unchanged. This forces the contribution from $\Omega(\mathbf{k}) \to -\Omega(-\mathbf{k})$.[13] Under inversion symmetry, $\dot{\mathbf{r}} \to -\dot{\mathbf{r}}$, $\mathbf{k} \to -\mathbf{k}$, and $\mathbf{E} \to -\mathbf{E}$ which forces $\Omega(\mathbf{k}) = \Omega(-\mathbf{k})$. In symbols:

$$\begin{aligned} &\text{T: } \Omega(\mathbf{k}) \to -\Omega(-\mathbf{k}) \\ &\text{I: } \Omega(\mathbf{k}) \to \Omega(-\mathbf{k}) \\ \implies &\text{TI: } \Omega(\mathbf{k}) = -\Omega(\mathbf{k}) = 0 \end{aligned} \tag{2.22}$$

The above would seem to assert that the only time we can have non-zero Berry curvature is when time or inversion symmetry is broken. This presents a problem for systems

[13] This, of course, neglects the spin of the electron. This fact is the punchline of the following paragraph. This deliberately incorrect presentation is for effect.

like non-magnetic transition metals which have both time reversal and inversion symmetry and still display a spin Hall effect. The way out it is that we neglected something important and in doing so violated a key assumption in our derivation.

The something important we neglected was the spin of the electron. The presence of both time reversal symmetry[14] and inversion symmetry enforces a degeneracy between spin states such that

$$|\Psi_{\uparrow}(\mathbf{k})\rangle = TI|\Psi_{\downarrow}(\mathbf{k})\rangle \tag{2.23}$$

This is important because the adiabatic theorem, the thing upon which we predicated our original derivation, fails if we have degenerate states because there is nothing to stop the electron from hopping all willy nilly between the two degenerate states in which it finds itself. The solution is that we need to consider all the degenerate states simultaneously in our description of the Berry curvature and extend the Berry curvature to be a tensor of dimension equal to the number of states in our degenerate subspace[41, 47]. For a Kramer's degenerate system with inversion symmetry, that means our degenerate subspace is of the electron spin (*i.e.* two states) so the Berry curvature will take the form of a 2x2 vector value matrix[15]. Because we are discussing symmetries, I should also note that the group theoretic term for what has happened to the Berry curvature is that it has become non-Abelian (*i.e.* operations on the now tensorial Ω are no longer necessarily commutative).

[14]The symmetry enforced by time reversal has a special name: Kramer's degeneracy

[15]So then a tensor of rank three, but it makes more intuitive sense phrased that way

The extension of the formalism to a tensor theory is fairly straightforward[48, 49]:

$$\mathrm{A}(\mathbf{R}) = i\langle\psi(\mathbf{R})|\nabla_{\mathbf{R}}|\psi(\mathbf{R})\rangle \tag{2.24}$$

$$\rightarrow \mathrm{A}_{ij}(\mathbf{R}) = i\langle\psi_i(\mathbf{R})|\nabla_{\mathbf{R}}|\psi_j(\mathbf{R})\rangle$$

$$\Omega(\mathbf{R}) = \nabla_{\mathbf{R}} \times \mathrm{A}(\mathbf{R}) \tag{2.25}$$

$$\rightarrow \Omega_{ij}(\mathbf{R}) = \underbrace{i\langle\nabla_{\mathbf{R}}\psi_i(\mathbf{R})| \times |\nabla_{\mathbf{R}}\psi_j(\mathbf{R})\rangle}_{\text{Like } \Omega(\mathbf{R})} + \underbrace{i\sum_{k\in\Sigma}\langle\psi_i(\mathbf{R})|\nabla_{\mathbf{R}}|\psi_k(\mathbf{R})\rangle \times \langle\psi_k(\mathbf{R})|\nabla_{\mathbf{R}}|\psi_j(\mathbf{R})\rangle}_{\text{Extra piece not in scalar } \Omega}$$

where Σ contains the indices of all states in the degenerate subspace.[16]

Why is there now an extra piece in $\Omega_{ij}(\mathbf{R})$? The definition of a tensor is that it transforms like a tensor. Unfortunately, naively trying to apply the curl operator to our now tensorial $\mathrm{A}(\mathbf{R})$ would result in an Ω that would not transform properly (*i.e.* covariantly). [17] To sort this out we just add in a correction so that Ω tensor object transforms appropriately.[18] From a more intuitive perspective, that extra piece accounts for the fact that at each point in walk through the parameter $\mathbf{R}$ the eigenvectors of our degenerate subspace maybe changing. It wouldn't be sensical to compare $\Omega_{ij}(\mathbf{R})$ at one $\mathbf{R}$ to another if $\Omega_{ij}(\mathbf{R})$ was being represented in a different basis so we keep track of how the basis vectors have changed with the extra piece.[50].

Unfortunately, this means that $\overline{\Omega}_{ij}(\mathbf{R})$ is no longer gauge invariant[19]. Two gauge invariant quantities we can derive from $\overline{\Omega}_{ij}(\mathbf{R})$ are its trace and its determinant.[20] This brings us to the way out of Ω being identically zero in our discussion of symmetry. The symmetry requirement is actually a requirement on $\mathrm{Tr}\overline{\Omega}_{ij}$ to be zero. In the case of our two-dimensional Kramer's degenerate subspace that means that the diagonal terms must be

[16] To make it more concrete, in our case of Kramer's degeneracy plus inversion symmetry, $\Sigma = \{\uparrow\uparrow, \uparrow\downarrow, \downarrow\uparrow, \downarrow\downarrow\}$

[17] Why? The gauge freedom allows application of a unitary matrix transformation. Trying to take the derivatives would lead to extra pieces through the chain rule

[18] In the language of differential geometry, we are taking the covariant derivative

[19] And thus not observable

[20] There is nothing deep going here, this is just a statement about the effect of unitary transformations.

equal and opposite but not necessarily zero. This also hints as to why the spin Hall effect exists: the Berry curvature for one basis state has to be opposite the other. If we have chosen a gauge such that the basis states are eigenstates of, say, S_z then this statement means opposite spins travel in opposite directions with the same magnitude push from the $\dot{\mathbf{k}}_c \times \Omega_n(\mathbf{k}_c)$ term in Eq 2.18.

2.5 Calculating the Intrinsic Spin Hall Effect

These past few sections of mathematical prestidigitation have been fun, but let us now see how exactly we go from Berry curvature to intrinsic spin Hall effect in doing so gain the intuition I promised for interpreting a band structure with respect to the spin Hall effect. We have already laid most of the ground work so this exercise should be fairly straightforward, but not without nuance.

2.5.1 The Simple Approach

In the previous section we applied a semiclassical rational to a wavepacket to find that we pick up an anomalous velocity term proportional to a quantity we identified as the Berry curvature tensor. Our goal is to find the spin Hall current so we might try to operate with the spin operator the anomalous velocity given by the Berry curvature tensor in 2.18 and take the trace to get a gauge invariant object[49]. In this case the spin Hall conductivity of a $\hat{z}$ directed spin diffusing towards $\hat{y}$ as a result of an $\hat{x}$ directed electric field in the semiclassical formalism is given by

$$\sigma^z_{xy;n}(\mathbf{k}) = \mathrm{Tr}[S^z_n(\mathbf{k})\Omega^z_n(\mathbf{k})] \tag{2.26}$$

at each momentum $\mathbf{k}$ for each band n where

$$S_n^z(\mathbf{k}) = \begin{pmatrix} \langle \psi_{n\uparrow\mathbf{k}} | \sigma^z_{\uparrow\uparrow} | \psi_{n\uparrow\mathbf{k}} \rangle & \langle \psi_{n\uparrow\mathbf{k}} | \sigma^z_{\uparrow\downarrow} | \psi_{n\downarrow\mathbf{k}} \rangle \\ \langle \psi_{n\downarrow\mathbf{k}} | \sigma^z_{\downarrow\uparrow} | \psi_{n\uparrow\mathbf{k}} \rangle & \langle \psi_{n\downarrow\mathbf{k}} | \sigma^z_{\downarrow\downarrow} | \psi_{n\downarrow\mathbf{k}} \rangle \end{pmatrix} \tag{2.27}$$

with σ^z the s_z Pauli matrix. In a suitable choice of gauge where the basis states are approximately eigenstates of S_z this gives

$$S_n^z(\mathbf{k}) \approx \begin{pmatrix} 1 & 0 \\ 0 & -1 \end{pmatrix} \tag{2.28}$$

This is how we solve the problem of the trace of Ω_n^z being zero. The effect of the spin operator is to make the diagonal components of Ω_n^z the same sign and thus the trace not identically zero.

2.5.2 The More Correct Approach

Unfortunately the allure semiclassical physics in the case of the calculation spin Hall effect is a siren song which threatens to dash upon the rocks of ignorance. What we really need to do is break out the full machinery of linear response in quantum mechanics and calculate using the Kubo formula. One reason the semiclassical approach is so seductive is that in the case of Abelian Berry curvature, the semiclassical approach ends up being equivalent to the Kubo formula. As Refs. [48, 51] point out, this is not the case for non-Abelian Berry curvature. The reason is that in the semiclassical approach we throw away the off-diagonal pieces in the Berry curvature tensor.

The spin Hall conductivity of a $\hat{z}$ directed spin diffusing towards $\hat{y}$ as a result of an $\hat{x}$ directed electric field is given in the Kubo formalism as

$$\sigma^z_{xy;n}(\mathbf{k}) = -\hbar^2 \Sigma_{m\neq n} \frac{\Im[\langle \psi_{n\mathbf{k}} | \hat{j}_s | \psi_{m\mathbf{k}} \rangle \langle \psi_{m\mathbf{k}} | \hat{v}_y | \psi_{n\mathbf{k}} \rangle]}{(E_{n\mathbf{k}} - E_{m\mathbf{k}})^2} \tag{2.29}$$

where $\hat{j}_s$ is the spin current operator and $\hat{v}_y$ is the velocity operator. As mentioned above, in the case of Abelian Berry curvature, the $\hat{j}_s$ becomes another velocity operator and the conductivity tensor agrees exactly with the semiclassical approach. This is to say, the anomalous Hall conductivity is literally the Berry curvature integrated over Brillioun zone. The correct choice of spin current operator is debated[52], but a mostly correct version is $\hat{j}_s \equiv \{\hat{\sigma}^z, \hat{v}_x\}$. Clearly there is a velocity operator involved, but the full linear response tensor is no longer exactly identified with the Berry curvature. So, where does this leave us? The whole goal of this section was to lay the foundation for understanding the spin Hall effect through this object known as the Berry curvature. Is that still valid for generating intuition? Most likely yes. Careful calculation using the semiclassical approach yields results similar to the full Kubo formalism in at least Pt and Au [51].

2.5.3 Fermi level location and temperature dependence

One last question we should ask is what is the temperature dependence of the spin Hall conductivity. In analogy to side jump scattering, the effect of the Berry curvature is to cause a sideways motion by virtue of accruing some extra phase and should not depend on the the resistivity in the clean limit[21, 36]. Similarly to side jump scattering as well, $\sigma_{int} \propto \rho^{-2}$ in the high resistivity limit. The intuition is a bit more opaque than in the side jump case, but it is still approachable. The key is to note that the majority of the contribution to the spin Hall effect is due parts of band structure where the Fermi level lies within a gap opened by spin-orbit coupling. Certainly the existence of such gaps lead to large contributions to Eq. 2.29,[21] but their mere existence is not enough. If one examines the Berry curvature (or, more correctly, the contribution to Eq. 2.29) on opposites sides of an avoided crossing, one finds that the Berry curvature is opposite[48]. This means that

[21] Because at gaps, the denominator of Eq. 2.29 is minimized

if the Fermi level is above both sides of the gap then the contribution to the Eq. 2.29 from each side of the gap cancels. Thus to maximize the intrinsic spin Hall effect we want to engineer system where the Fermi lies within gaps opened by spin orbit coupling. In light of this, suppose we have very resistivity and thus short quasi-particle lifetimes and as a consequence a large energy uncertainty, $\hbar/\tau$, of the quasiparticle. If the energy scale $\hbar/\tau$ is comparable to the size of the gap, Δ in which the Fermi level might lie, then one begins to sample both negative and positive contributions to Eq. 2.29. Because the denominator of Eq. 2.29 is squared it is not too far of a stretch to see why we might expect ρ^2 when $\Delta \ll \hbar/\tau$. This story is of course not particularly rigorous. Ref. [21] lays out the computation in exquisite detail for those who desire a more rigorous explanation.

2.6 Reading a Bandstructure

Let's recap what we have learned. There is a mathematical object, the Berry curvature, that arises naturally in the semiclassical calculation of the motion of a wave packet. This object gives rise to a velocity transverse to the applied electric field and is spin dependent. It is not deep that it exists, when we invoked Bloch's theorem in our semiclassical calculation we "traded boundary conditions at infinity, for an infinity of boundary conditions"[41]. Less abstractly that's when a derivative with respect to $\mathbf{k}$ entered our equations and lead to the appearance of this mathematical object. We have found that the contributions to the Berry curvature; and thus the transverse, spin-dependent velocity; are maximized near avoided crosses in the band structure of a given material. It is not enough, however, for these avoided crossing to exist to merely exist. To avoid a cancellation in the summation of the Berry curvature over all occupied states the Fermi level must lie in between a gap opened by spin-orbit coupling.

In the case of a 3D material[22] with time reversal and inversion symmetry, two important things happen. The symmetry imposed equivalence of electrons at inverse k points means that the Berry curvature becomes non-Abelian, i.e. a tensor, with a basis that spans the degenerate subspaces of electrons with opposite spins. This has the effect of requiring the trace of the now Berry Curvature tensor to be zero. The second is that it is infinitely unlikely to find an accidental degeneracy in the band structure according to the codimension theorem of Wigner and Von Neumann. The consequence of this is that in the bulk of any 3D material with time reversal and inversion symmetry, the Berry curvature can never be quantized. [23]

The fact that contributions to the Berry Curvature are maximal near (avoided) band crossings helps provide more intuition as to what it actually is. That is, these band crosses are locuses where multiple states are similar enough that they may interact strongly. In the semiclassical picture of dynamics, we neglect this and assume a single band transport picture. Of course that is incorrect, the other bands nearby in energy can and do interact with the electron wavepacket. Two papers by Kontani and Tanaka *et al.*[36, 53] offer an alternative intuition in terms of orbital hopping picture (summarized in Fig. 2.3) that highlights this.

The argument is that if we consider an electron hopping around a path from say a d or f in on the starting atom (0 in Fig. 2.3) to s orbitals on a neighboring atoms (1 and 2 in Fig. 2.3) then back to a different d or f orbital on the staring atom (3 in Fig. 2.3), then spin-orbit coupling can potentially allow a transition back to the starting d or f orbital. In the concrete case of a transition from d_{xy} to $d_{x^2-y^2}$ for an $\uparrow$ spin, the matrix element yields a factor of $-i\hbar\lambda$[36]. This is equivalent to picking up a phase of $-\frac{\pi}{2}$ as $-i = e^{-i\frac{\pi}{2}}$. Kontani and

[22] Which is to say, a material in which we are considering an appreciable number of unit cells in all three directions

[23] This is not to say that there can't be degeneracies in the band structure of such a material, it is just that if they exist, they are symmetry protected and thus part of a degenerate subspace.

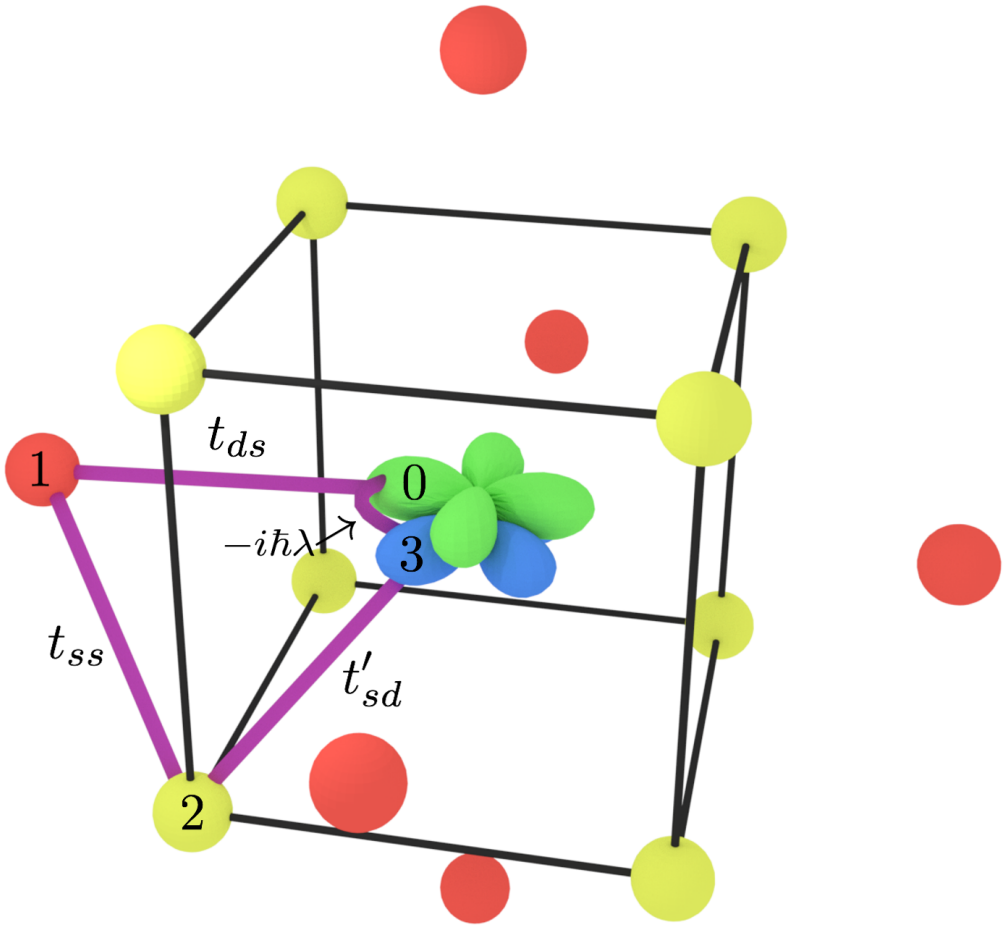

Figure 2.3: Hopping picture of the spin Hall effect in a BCC crystal of a transition metal after the diagrams in [36, 53] . Yellow (red) spheres represent the s orbitals of nearest (next-nearest) neighbor atoms of the central atom for which only the d_xy and $d_{x^2-y^2}$ is shown. A possible closed loop for an electron to hop is given by the purple lines ($d_{x^2-y^2} \rightarrow s \rightarrow s \rightarrow d_{xy} \rightarrow d_{x^2-y^2}$) with matrix elements give by t and λ. The key is that spin-orbit coupling (with strength λ lets us go from $d_{xy} \rightarrow d_{x^2-y^2}$ with matrix element $\pm i\lambda\hbar$ where the sign is spin dependent.

Tanaka [36] suggestively rewrite this phase factor as

$$-\frac{\pi}{2} = -\frac{\phi_0}{4}\frac{2\pi}{\phi_0} \tag{2.30}$$

where $\phi_0 = \frac{hc}{e}$ is magnetic flux quantum. We can then think of this close loop as arising from the effect of a magnetic vector potential such that

$$\oint_0^3 A(\mathbf{r})d\mathbf{r} = -\frac{\phi_0}{4} \tag{2.31}$$

in analogy to the Aharonov-Bohm effect [54].

In section 2.4.1, I feigned concern that it was a poor choice of notation have the magnetic vector potential, A, and the Berry connection, A, be represented by similar symbols. The implied indignation was all a ruse. The similarity in symbols is not accidental; both A (the magnetic vector potential) and A (the Berry connection) are deep statements about geometry, *connecting* how the underlying shape of the parameter space affect the motion of things through it. Eq. 2.31 looks *exactly* like a Eq. 2.8.[24] The Aharonov-Bohm effect is just a special case of the Berry phase. Rumination on notation aside, this argument provides a real space picture of how the spin Hall effect arises and cleanly points out the necessity of the participation of other states (s) and the spin-orbit coupling strength, λ.

Lastly, we noted that in the low resistivity limit that $\sigma_{sk} \propto \rho^{-1}$, $\sigma_{sj} \propto \rho^{0}$, and $\sigma_{int} \propto \rho^{0}$. In the high resistivity limit,[25] we instead have $\sigma_{sj} \propto \rho^{-2}$, and $\sigma_{int} \propto \rho^{-2}$. These resistivity dependences give us a method by which to discern the dominant effect by varying the resistivity. The most common way to do this is by varying the temperature. In a normal metal, this would mean that σ_{sk} would increase with decreasing temperature, while σ_{sj} and σ_{int} would remain constant (in the low resistivity limit).

2.7 Symmetry: Round II

Thus far we have focused on a microscopic picture of the spin Hall effect. Doing so naturally leads to the spin Hall effect identified as arising from the Berry curvature present in a non-magnetic metal. However, it only leads to the spin Hall effect. Phrased even

[24] *modulo* a factor of i

[25] Recall from the discussion at the end of the previous section that what sets the scale of "high" resistivity is when the quasi-particle lifetimes are so short that the associated energy uncertainty is comparable to the size of gaps opened by spin-orbit coupling.

more explicitly, the microscopic picture only leads to the diffusion of spins transverse to both the electric field and the spin direction. It behooves us to ask is this consistent with Neumann's principle.[26] More industrious minds than me have already answered this question in this beautiful paper[55]. I will not reproduce any of the derivations because I don't think I can add anything. The symmetry imposed shape of the tensor which considers spins point along $\hat{z}$ for a cubic, non-magnetic, material such as Pt (magnetic Laue group $m\bar{3}m$ omitting the time reversal operation) has the form

$$\overline{\sigma^z} = \begin{pmatrix} 0 & \sigma^z_{xy} & 0 \\ -\sigma^z_{xy} & 0 & 0 \\ 0 & 0 & 0 \end{pmatrix} \tag{2.32}$$

This is simultaneously heartening and disheartening. This is indeed the form of the semiclassical result, but it is only the form of the semiclassical result. We could look at the tensors for $\overline{\sigma}^x$ and $\overline{\sigma}^y$, but we don't need to; the high symmetry of the Pt crystal structure enforces this only spin Hall like behavior in every direction with no anisotropy. Evidently in this high symmetry system we should only expect to see the "classical" spin Hall effect with spins perpendicular to electric field and diffusion direction. Let's examine a system with lower symmetry, one that is orthorhombic (magnetic Laue group *mmm* omitting the time reversal operation).

$$\overline{\sigma^z} = \begin{pmatrix} 0 & \sigma^z_{xy} & 0 \\ \sigma^z_{yx} & 0 & 0 \\ 0 & 0 & 0 \end{pmatrix} \tag{2.33}$$

It may not look like anything deep has happened, but something deep has, the two nonzero elements are now no longer forced to be related by symmetry. This allows a spin Hall effect with spins having Rashba-like *and* Dresselhaus-like symmetry. That is,

[26] The statement that the symmetry of the linear response tensor is consistent with the symmetry operations of the crystal.

spins are no longer forbidden to be collinear with the current flow direction for certain crystal directions. If we lower the symmetry to monoclinic then there are no symmetry restrictions on the torques and any spin direction is possible for the spin Hall effect. Of course all of these statements are to the effect of necessary but not sufficient. Just because symmetry allows a certain type of spin Hall effect, it does not guarantee it will be detectable or non-zero.

There is even more to the story too, because the above statements have been predicated on an examination of the bulk crystal symmetry. Putting a magnetic material on top of the crystal at the very least locally breaks inversion symmetry and may reduce the symmetry of the crystal at the interface substantially. This could potentially allow a high symmetry material to generate novel spin Hall effects at just the interface.

CHAPTER 3

EXPERIMENTAL DESIGN

With our sojourn through the wilds of pure theory out of the way, we can now do even more theory to figure out how to measure the spin Hall effect. In the broadest terms, our fundamental goal is to measure the spin of an electron in a material. Spin is a magnetic degree of freedom so our measurements will have to couple to magnetism in some way. In the purest sense, one could imagine measuring the spin accumulation due to the spin Hall effect directly via the magneto-optical Kerr effect (MOKE)[56]; however, the signal in a such an experiment in a metallic system is exceptionally small and has only recently been realized[57]. No, more commonly we[1] have endeavored to measure the spin Hall effect and other current-induced spin orbit torques by examining the effect of those torques on a thin magnetic layer deposited on a surface of the magnet.[2] We may then determine the magnitude and origin of the torques acting on the magnet by examining the motion of the magnet via the magnet's anisotropic magnetoresistance, the anomalous Hall effect, or optically through MOKE.

In this thesis, I will cover three techniques in detail. The first utilizes a high frequency (≈5-40 GHz) current to produce oscillating current-induced spin torques to drive the adjacent ferromagnetic layer in a normal metal/ferromagnet bilayer system. The oscillation of the magnetization can then be read out through a combination of the magnet's anisotropic magnetoresistance and the high frequency current. This is known as spin-torque ferromagnetic resonance and the strength of the current-induced torques can be determined from the amplitude. The second is a variation on the first wherein a DC-bias is applied on top of the RF excitation and the magnitude of the torques may be derived from the

[1] In sense of the scientific community

[2] This is also the more technologically relevant as the utility of the current induced spin torques for technological purposes is to switch the magnetizations of tiny magnets.

evolution of the resonance lineshape with current. The last is using MOKE in a clever[3] way to quantitatively extract current-induced torques optically.

Each of the aforementioned techniques is not new. However, previous treatments of the analysis in the literature have been less than general. In particular, most of the literature excludes in their derivations the possibility of torques with arbitrary symmetry. This is for good reason, most systems that have been studied are too constrained by symmetry to admit more than one type of torque. Recent work on single crystal flakes of the transition metal dichalcogenides has revealed that in sufficiently low symmetry systems, torques with different symmetries are possible [58, 59]. To this end, I do think I can contribute something to the sum of knowledge by tedious by explicitly re-deriving the equations governing the analysis of each of these experiments, and so I shall.

3.1 Spin Torque Ferromagnetic Resonance

Treatments of spin torque ferromagnetic resonance in the literature[5, 33, 60–63] have been in such a way that is not necessarily the most transparent, nor naturally includes the possibility of torques in arbitrary directions. To this end, I will re-derive the solutions for motion of the ferromagnet with moment $\overrightarrow{M}$ and saturation magnetization M_s in a thin film normal metal/ferromagnet bilayer. We will assume that the ferromagnetic layer has it's equilibrium position in-plane, but nothing else about any possible anisotropies. The coordinate system we will use is defined in Fig. 3.1 with $\hat{x}'$ along the charge current flow direction, $\hat{x}$ along equilibrium direction of the magnetization, and $\hat{z} = \hat{z}'$ perpendicular to the plane of the bilayer. Given the magnitude of the driving torques (i.e. small), only minor excursions will be made from this equilibrium direction so that we may write the unit moment $\hat{m} \equiv \overrightarrow{M}/M_s$ as $\hat{m} \approx (1, m_y, m_z)$. Our quarry is then to solve the Landau-Lifshitz-

[3] I think it's clever, at least

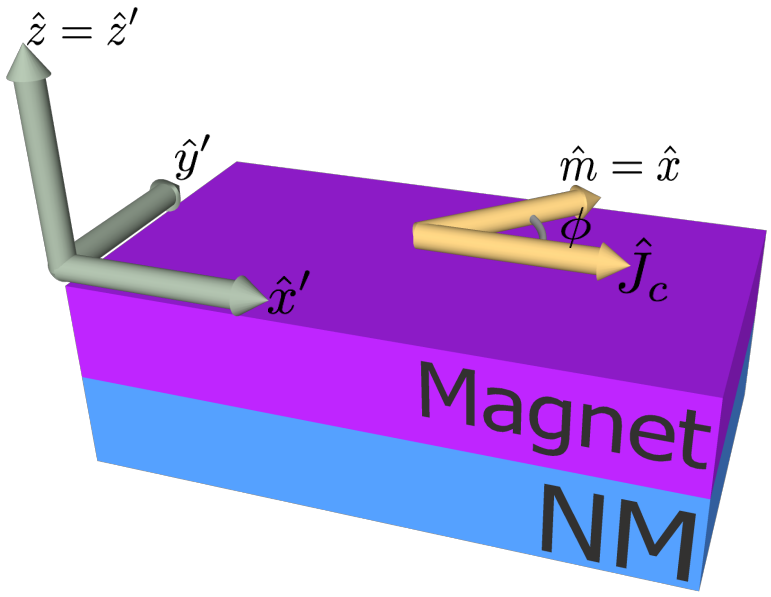

Figure 3.1: Schematic illustration of the conventions used in the following derivations of ST-FMR. The primed basis is aligned to the edges of the sample. The unprimed basis is given by in-plane rotation by an angle ϕ such that the $\hat{x}$ lies parallel the equilibrium direction of the magnetization of the magnet.

Gilbert equations with the Slonczewski spin transfer torque term (LLGS equations)[64] for the motion of a ferromagnet under GHz excitation:

$$\dot{\hat{m}} = \alpha \hat{m} \times \dot{\hat{m}} + \overrightarrow{\tau}_{eq} + \overrightarrow{\tau}_{neq} \tag{3.1}$$

where α is the phenomenological Gilbert damping parameter, $\overrightarrow{\tau}_{eq}$ are those torques which arise from the effective fields generated in response to the magnet deviating from its equilibrium position, and $\overrightarrow{\tau}_{neq}$ are those torques arising from the application of current to normal metal/ferromagnet bilayer through effects such as the spin Hall effect.

3.1.1 The Equilibrium Torques

Strictly, what I mean by equilibrium torques is $\gamma\hat{m}$ crossed with the effective field resulting from deviating from the equilibrium direction along an orthogonal direction. That is,

$$\overrightarrow{\tau}_{eq} = -\left(\gamma\hat{m} \times -\frac{dF}{d\hat{m}}\right) \tag{3.2}$$

where $\times$ is the cross product, and $-\frac{dF}{d\hat{m}}$ is the negative derivative of the magnetic free energy (divided by M_s) with respect to the direction of the magnetization (which is to the say the effective field). As I mentioned at the start, our goal is the most general solution to these equations. So, what is the most general form of the free energy for the system we are examining?

$$F(\overrightarrow{B})/M_s = \underbrace{-\hat{m}\cdot\overrightarrow{B}_{ext}}_{\text{dipole}} + \underbrace{\frac{1}{2}M_s\hat{m}\cdot\overrightarrow{N}_{demag}\cdot\hat{m}}_{\text{demagnetization}} + \underbrace{A(\hat{m})}_{\text{anisotropy}} \tag{3.3}$$

where $\overrightarrow{B}_{ext}$ is the externally applied magnetic field, $\overrightarrow{N}_{demag} = \begin{pmatrix} 0 & 0 & 0 \\ 0 & 0 & 0 \\ 0 & 0 & 1 \end{pmatrix}$ is the demagnetization tensor for a thin film, and $A(\hat{m})$ contains any terms owing to crystalline anisotropy or other effects. If $\frac{A(\hat{m})}{d\hat{m}}$ were zero then $\frac{dF}{d\hat{m}}$ would reduce to (remembering that in this case the magnetization and external field would be parallel)

$$\overrightarrow{\frac{dF}{d\hat{m}}} = \begin{pmatrix} -B_{ext} \\ 0 \\ m_z M_s \end{pmatrix} \tag{3.4}$$

the resulting equilibrium torques are then familiar

$$\overrightarrow{\tau}_{eq} = \gamma \begin{pmatrix} m_y(-m_z M_s) \\ m_z(-B_{ext}) - m_x(m_z M_s) \\ -m_y(-B_{ext}) \end{pmatrix} \tag{3.5}$$

Now, our choice of coordinate basis means $m_x \approx 1$ so we can ignore that factor in $\hat{y}$ component. Furthermore, the $\hat{x}$ equilibrium torque component has two factors of m which are not m_x so it will oscillate at twice the natural frequency. Since we will be looking at the magnetic response at the driving frequency, we do not care about this component so we will neglect it, as before.

This is great and all, but it is not actually the most general form of the equilibrium torques. In the case we just worked we explicitly neglected the piece the contains the possibility for arbitrary corrections, $A(\hat{m})$. We *could* figure out what the most general forms of $A(\hat{m})$ are and generate explicit solutions, but that would be tedious and unenlightening with regards to our current goal (which will just be tedious). Inspired by [63], let us instead say, "Well, we know how to figure it out if we are given an arbitrary $(\hat{m})$, so let's hide that fact in a succinct piece of notation so that we can understand the effects of these equilibrium torques on the equations of motion." To do that, we note that in these units the dimension of τ is just frequency so we'll write

$$\overrightarrow{\tau}_{eq} = \begin{pmatrix} 0 \\ -m_z\omega_2 \\ m_y\omega_1 \end{pmatrix} \tag{3.6}$$

Again, we won't concern ourselves with the $\hat{x}$ piece as we are assuming that the p with $\omega_1 \equiv \gamma B_{ext}$ and $\omega_2 \equiv \gamma(B_{ext} + M_s)$ (for the case of no in-plane anisotropy).

3.1.2 The Damping Term $\alpha\hat{m} \times \dot{\hat{m}}$

We'll tackle the damping term next as it is pretty straightforward. Doing the cross product we get

$$\alpha\hat{m} \times \dot{\hat{m}} = \alpha \begin{pmatrix} m_y\dot{m}_z - m_z\dot{m}_y \\ m_z\dot{m}_x - m_x\dot{m}_z \\ m_x\dot{m}_y - m_y\dot{m}_x \end{pmatrix} \tag{3.7}$$

$$\approx \alpha \begin{pmatrix} m_y\dot{m}_z - m_z\dot{m}_y \\ -\dot{m}_z \\ \dot{m}_y \end{pmatrix} \tag{3.8}$$

Using the approximations that $m_x = 1$ and thus $\dot{m}_x = 0$. For this same reason we won't concern ourselves with the $\hat{x}$ component, we don't expect any meaningful changes along the $\hat{x}$ direction.[4]

3.1.3 The non-equilibrium torques

Lastly, we need to discuss the non-equilibrium torques. For the purposes of solving the LLGS equations, we do not care about the explicit form for these torques. All we need to note to move forward is that the most general form for the torques is one that acts out of the plane of the thin film we are considering, $\tau_{OOP}\hat{z}$, and one that acts in-plane but perpendicular to the magnetization direction, $\tau_{IP}\hat{y}$.Thus

$$\overrightarrow{\tau}_{neq} = \begin{pmatrix} 0 \\ \tau_{IP} \\ \tau_{OOP} \end{pmatrix} \tag{3.9}$$

[4]In fact, you'll recall, we predicated this whole derivation on that assumption

We do in general care, however, about the form of these torques and there is deep physics associated with the allowed forms of these torques. To that end, let us examine exact their form and possible origin.

In analogy with the equilibrium torques, we could imagine treating the non-equilibrium torques as an oscillatory effective magnetic field pointing in a given direction. In the case of the so-called Ørsted field generated via the current flowing through the normal metal in the bilayer, this effective field is literally a field. One could also imagine an accumulation of spins at the normal metal/ferromagnet interface giving rise to an exchange field parallel or anti-parallel to the spin accumulation direction. Lastly, there is the possibility of an electron with spin non-collinear to the magnetization of the ferromagnet impinging on the ferromagnet from the normal metal, and precessing about the magnetization of the ferromagnet. In this last case, electron deposits it angular momentum into the magnet and thus drives it out of equilibrium via what is known as spin transfer torque. These last two torques rely on a mechanism that gives rise to spin current and are thus the torques that contain information about effects such as the spin Hall effect.

The analytic form for the magnitude of the spin transfer torque is given by

$$\overrightarrow{\tau}_{neq} = \frac{\hbar}{2e}\frac{\gamma}{M_s t_{mag}} J_s \hat{m} \times (\hat{m} \times \hat{\sigma}) \tag{3.10}$$

where e is the charge of the electron, t_{mag} is the thickness of the magnetic layer, J_s is the spin current density, and $\hat{\sigma}$ is the direction of the impinging electron spin. We define a dimensionless efficiency, θ, such that $J_s \equiv \theta J_c$ where J_c is the charge current density through the spin Hall material layer.[5] Thus Eq. 3.10 becomes

$$\overrightarrow{\tau}_{neq} = \frac{\hbar}{2e}\frac{\gamma}{M_s t_{mag}} \xi J_c \hat{m} \times (\hat{m} \times \hat{\sigma}) \tag{3.11}$$

[5]There is a geometric subtlety here.J_s is measured through the surface of the film adjacent to the magnetic, whereas J_c is measured through the cross section of the film.

What is ξ? In the case of spin transfer torque, it is the product of how effective the material is at generator spin current, a dimensionless efficiency Θ_{SH}, and the transparency T of the interface to absorbing the angular momentum from the impinging spin current. If the spins are generated via the spin Hall effect (*i.e.* the spin current travels transverse to the charge current), then ξ is also the tangent of a Hall angle (times the interface transparency). As such, there is no reason that ξ cannot be greater than one, it just means that the spin Hall current is very large.[6] The spin Hall conductivity, σ_{SH} is then given by $\Theta_{SH}\sigma_c$ where σ_c is the charge conductivity of the normal metal. If you recall from chapter 2, σ_{SH} is what we can actually calculate from the electronic structure of a given material, and is thus our goal if we are trying to compare experiment to theory. However, figuring out the interface transparency is no small feat and may be confounded by things such as magnetic dead-layering or a lack of suitable control samples[65]. The job of the experimentalist is then to deal with this problem and will be discussed in the context of actual experiments in the second half of this thesis.

3.1.4 Solving the LLGS equation

With all the piece worked out now we can start solving the LLGS equation itself. Putting everything in:

$$\begin{pmatrix} 0 \\ \dot{m}_y \\ \dot{m}_z \end{pmatrix} = \begin{pmatrix} 0 \\ -\alpha\dot{m}_z - m_z\omega_2 + \tau_{IP} \\ \alpha\dot{m}_y + m_y\omega_1 + \tau_{OOP} \end{pmatrix} \tag{3.12}$$

To move forward toward a solution we need to deal with those pesky time derivatives. Since we have a notion of what the magnetization is going to do (precess), lets take a

[6] Microscopically this could correspond to an electron being polarized by the spin Hall effect, bouncing off of the magnet and depositing its angular momentum, then getting repolarized and so on, skipping across the metal/magnet interface.

guess that the solutions are some static amplitude times $e^{-i\omega t}$ where the unadorned ω is the frequency of the driving torques. This makes the time derivatives trivial, just pulling down $-i\omega$. The remaining factors of $e^{-i\omega t}$ cancel. This leaves

$$\begin{pmatrix} 0 \\ -i\omega m_y \\ -i\omega m_z \end{pmatrix} = \begin{pmatrix} 0 \\ i\omega\alpha m_z - m_z\omega_2 + \tau_{IP} \\ -i\omega\alpha m_y + m_y\omega_1 + \tau_{OOP} \end{pmatrix} \tag{3.13}$$

Rearranging,

$$\begin{pmatrix} 0 \\ -i\omega m_y \\ -i\omega m_z \end{pmatrix} = \begin{pmatrix} 0 \\ m_z(i\omega\alpha - \omega_2) + \tau_{IP} \\ -m_y(i\omega\alpha - \omega_1) + \tau_{OOP} \end{pmatrix} \tag{3.14}$$

Now we need to pick one of m_y or m_z to solve for initially. Because the piece we care about for electrical detection in a "standard" ST-FMR experiment is m_y, I will solve for that here.[7] We can of course get m_z if we want it later by plugging m_y into $\dot{m}_z$.

$$-i\omega m_y = \frac{1}{-i\omega}(i\omega\alpha - \omega_2)(-m_y(i\omega\alpha - \omega_1) + \tau_{OOP}) + \tau_{IP} \tag{3.15}$$

Distributing the $(i\omega\alpha - \omega_2)$

$$-i\omega m_y = \frac{1}{i\omega} m_y(i\omega\alpha - \omega_1)(i\omega\alpha - \omega_2) + \frac{1}{-i\omega}\tau_{OOP}(i\omega\alpha - \omega_2) + \tau_{IP} \tag{3.16}$$

Collecting all of the m_y terms

$$-m_y(i\omega + \frac{1}{i\omega}(i\omega\alpha - \omega_1)(i\omega\alpha - \omega_2)) = \frac{1}{-i\omega}\tau_{OOP}(i\omega\alpha - \omega_2) + \tau_{IP} \tag{3.17}$$

Multiplying through by $i\omega$

$$-m_y(-\omega^2 + (i\omega\alpha - \omega_1)(i\omega\alpha - \omega_2)) = -\tau_{OOP}(i\omega\alpha - \omega_2) + i\omega\tau_{IP} \tag{3.18}$$

[7] Just what a "standard" ST-FMR experiment looks like I will discuss at the end of this section.

Further expanding

$$-m_y(-\omega^2 - \omega^2\alpha^2 - i\omega\alpha(\omega_1 + \omega_2) + \omega_1\omega_2) = -\tau_{OOP}(i\omega\alpha - \omega_2) + i\omega\tau_{IP} \tag{3.19}$$

Isolating m_y

$$m_y = \frac{-\tau_{OOP}(i\omega\alpha - \omega_2) + i\omega\tau_{IP}}{\omega^2(1 + \alpha^2) + i\omega\alpha(\omega_1 + \omega_2) - \omega_1\omega_2} \tag{3.20}$$

Here we are going to make an approximation[8]. The gilbert damping parameter, α, is typically around 10^{-2} or less in commonly used thin film magnet choices. Thus α^2 is going to be $\approx 10^{-4}$ or less which is very small compared to 1 so $(1 + \alpha^2) \approx 1$. Rearranging after that:

$$m_y = \frac{-\tau_{OOP}(i\omega\alpha - \omega_2) + i\omega\tau_{IP}}{(\omega^2 - \omega_1\omega_2) + i\omega\alpha(\omega_1 + \omega_2)} \tag{3.21}$$

Now let's make the denominator purely real by multiplying both numerator and denominator by the complex conjugate of the denominator

$$m_y = \frac{((\omega^2 - \omega_1\omega_2) - i\omega\alpha(\omega_1 + \omega_2))(-\tau_{OOP}(i\omega\alpha - \omega_2) + i\omega\tau_{IP})}{(\omega^2 - \omega_1\omega_2)^2 + \omega^2\alpha^2(\omega_1 + \omega_2)^2} \tag{3.22}$$

3.1.5 Prescient Definitions

Let us pause a moment and consider what we have. The denominator has the form of a Lorentzian denominator so let's make that explicit. We will define

$$\omega_0^2 \equiv \omega_1\omega_2 \tag{3.23}$$

and

$$\omega^+ \equiv \omega_1 + \omega_2 \tag{3.24}$$

This gives:

[8] Alas

$$m_y = \frac{((\omega^2 - \omega_0^2) - i\omega\alpha\omega^+)(-\tau_{OOP}(i\omega\alpha - \omega_2) + i\omega\tau_{IP})}{(\omega^2 - \omega_0^2)^2 + \omega^2\alpha^2(\omega^+)^2} \tag{3.25}$$

Clearly, then, ω_0 is the resonant frequency of the system. It is also the geometric mean of ω_1 and ω_2. This makes sense, these are the two characteristic frequencies of this system. This is also why I stated early that it would be instructive to do the derivation this way, not worrying about the explicit forms of the equilibrium torques, this result falls out manifestly. That is not to say that the same thing won't happen in a less abstract derivation, but it is perhaps not as quite clear that the components of the resonant frequency were somewhat deep statements about the system.

Does it make sense that we ended up a with a Lorentzian? I would argue yes. The LLGS equations for a given vector direction have the form of damped (literally the Gilbert damping), driven (the non-equilibrium torques) harmonic oscillator (this would be more clear if we had tried to decouple the equations of motion for m_y and m_z before inserting our ansatz). The solutions are then naturally Lorentzian in nature. This also gives us some indication of what we might expect with regards to phase of the magnet oscillation as a result of the two non-equilibrium torques. The effect of τ_{IP} is to rotate the moment out of plane (corresponding to an out of plane field), while the effect of τ_{OOP} is to rotate the moment in-plane (corresponding to an in-plane field). It this sense, τ_{OOP} is closer to giving rise to a classical damped driven harmonic oscillator as it is supplying a drive in the same direction as the motion of m_y. Thus we expect that at resonance the motion of the m_y component of the moment due to τ_{OOP} should be completely out of phase with the driving current. The opposite is true of τ_{IP}. The energy deposited due to τ_{IP} is in a direction perpendicular to m_y so the effect of τ_{IP} on the amplitude of m_y is only felt $\pi/2$ of a period later when all of m_z converts to m_y as the moment precesses. Thus at resonance, the motion of m_y due to τ_{IP} should be completely in phase.

3.1.6 The in-phase component

The last paragraph of the preceding section was laid out in tedious detail to set up the story of this section, how we actually detect the motion of the magnet. Magnets exhibit anisotropic magnetoresistance (AMR) in which their longitudinal resistance varies with the direction of the moment relative the current flow direction. At room temperature, the dominant form for the AMR to take is $(R_\perp - R_\parallel)\sin(\phi)^2\sin(\theta)^2$ where $\perp$ and $\parallel$ refer to the relative orientation of the current and the magnetization. We are considering only in-plane ferromagnets $\theta = \pi/2$ so the AMR reduces to $\Delta R \sin(\phi)^2$ with $\Delta R \equiv R_\perp - R_\parallel$.

How is this useful to us? The motion of m_y is small and orthogonal to the equilibrium direction and can thus be treat as a small time dependent angular perturbation on top of ϕ. If we Taylor expand about ϕ this gives $2\Delta\phi\Delta R\sin(\phi)\cos(\phi)$ for the linear part with $\Delta\phi \equiv (m_y + \phi) - \phi = m_y$. Ultimately, this means that the motion of the magnetization causes a change in longitudinal resistance of the ferromagnet layer at the same frequency of the current applied giving rise to the torques which are driving the system. This gives rise to $2\Delta R\sin(\phi)\cos(\phi)\Delta\phi(\omega t)I(\omega t) = \frac{1}{2}(2\Delta R\sin(\phi)\cos(\phi)\Delta\phi(0) + 2\Delta R\sin(\phi)\cos(\phi)\Delta\phi I(2\omega t))$ through standard trigonometric identities.[9] $\Delta R\Delta I(0) \equiv V_{mix}$ is a DC voltage and is thus pretty straightforward to detect. I'll discuss the actually experimental implementation in a later section, but the key take away is that we need the in phase (real) part of the motion of m_y as that is what is mixed down to a DC voltage by the product of the resistance and the current. Doing that we get

$$\Re[m_x] = \frac{((\omega^2 - \omega_0^2)\omega_2 - \alpha^2\omega^2\omega^+)\tau_{OOP} - \alpha\omega^2\omega^+\tau_{IP}}{(\omega^2 - \omega_0^2)^2 + \omega^2\alpha^2(\omega^+)^2} \tag{3.26}$$

You may have noticed it earlier and it is perhaps glaringly obvious at this point, but I have not made an assumption normally done at this stage or earlier in other deriva-

[9] This is the same principle used in lock in amplification.

tions: that $\omega\alpha \ll \omega_2$ in the part multiplying τ_{OOP} in the numerator. It is pretty typically a good assumption, especially in the simple case, and the modifications to the lineshape are small. I leave it in at this stage in and comment on it in case a system with crazy anisotropies changes the validity of the inequality just mentioned. To really get a really good handle on things lets rewrite:

$$\Re[m_x] = \underbrace{\frac{(\omega^2 - \omega_0^2)\omega_2\tau_{OOP}}{(\omega^2 - \omega_0^2)^2 + \omega^2\alpha^2(\omega^+)^2}}_{\text{Antisymmetric Lorentzian}} - \underbrace{\frac{\alpha\omega^2\omega^+(\alpha\tau_{OOP} + \tau_{IP})}{(\omega^2 - \omega_0^2)^2 + \omega^2\alpha^2(\omega^+)^2}}_{\text{Symmetric Lorentzian}} \tag{3.27}$$

Now we see that the resulting signal should be the sum of a symmetric and antisymmetric Lorentzian, and that if the stars align (figuratively) then the out of plane torque could lead to a symmetric component (literally). This is also corroborates our intuition from earlier concerning the phase of response. The out of plane torques lead to a completely out of phase oscillation at resonance so the in phase component of the signal must go through zero at resonance while the opposite is true of the in-plane torques.

3.1.7 Expansion about the resonant field

So we've made it, but did we really? The above equation is still "phrased" wrong, everything is in terms of frequencies. We want something in terms of B_{ext} because that is going to be the parameter most sensible to sweep in the physical experiments discussed later. We still don't want to assume anything about the B-dependence of ω_1 or ω_2, though. So, we Taylor expand about the resonant field. That's the region around which our signal will be maximal and, because the linewidth should be pretty sharp, we can get away with linear order terms only to excellent approximation.

$$\omega_0^2 \approx \omega_0^2\big|_{B=B_0} + (B - B_0)\left.\frac{d(\omega_0^2)}{dB}\right|_{B=B_0} \tag{3.28}$$

What is $\omega_0^2\big|_{B=B_0}$? At the resonant field, it is literally the driving frequency squared ω^2, that is what it means to be resonant.

$$\left.\frac{d(\omega_0^2)}{dB}\right|_{B=B_0} = \omega_1 \left.\frac{d(\omega_2)}{dB}\right|_{B=B_0} + \omega_2 \left.\frac{d(\omega_1)}{dB}\right|_{B=B_0} \tag{3.29}$$

Now we are at somewhat of an impasse. We need to know what the derivatives of the natural frequencies are. We could keep them entirely general, but do we really need to? Looking back to the derivation of the equilibrium torques in the case of no anisotropy, note that the field dependence only enters the equilibrium torques as a γB_{ext} term. If there were anisotropy terms with field dependence, that field dependence would likely come in as a reorientation of the magnetization with field, meaning that it would be suppressed by a factor of at least the external field. Thus, to a pretty general approximation, we get

$$\left.\frac{d(\omega_0^2)}{dB}\right|_{B=B_0} = \gamma\ \omega_1|_{B=B_0} + \gamma\ \omega_2|_{B=B_0} \tag{3.30}$$

$$\left.\frac{d(\omega_0^2)}{dB}\right|_{B=B_0} = \gamma\omega_{B0}^{+} \tag{3.31}$$

with

$$\omega_{B0}^{+} \equiv \omega^{+}\big|_{B=B_0} \tag{3.32}$$

To be more accurate, we could then to do the same Taylor expansion for the remaining "bare" ω^+ terms in $\Re[m_x]$ as well as the ω_2 next to the τ_{OOP}. However, given the fact that α is typically small (we predicated several previous assumptions on that basis already), the Lorentzian line shape is pretty sharply peaked. In that regard, we can to a reasonable approximation treat it as a delta function about resonant field, B_0. Thus the "bare" ω^+'s become ω_{B0}^+'s and the ω_2 becomes $\omega_{2,B0}$.

Putting everything together, we get

$$\Re[m_x] = \underbrace{\frac{(B-B_0)\gamma\omega_{B0}^{+}\omega_{2,B0}\tau_{OOP}}{\gamma^2(\omega_{B0}^{+})^2(B-B_0)^2 + \omega^2\alpha^2(\omega_{B0}^{+})^2}}_{\text{Antisymmetric Lorentzian}} - \underbrace{\frac{\alpha\omega^2\omega_{B0}^{+}(\alpha\tau_{OOP}+\tau_{IP})}{\gamma^2(\omega_{B0}^{+})^2(B-B_0)^2 + \omega^2\alpha^2(\omega_{B0}^{+})^2}}_{\text{Symmetric Lorentzian}} \tag{3.33}$$

Lets make one more definition and rearrange slightly

$$\Delta \equiv \frac{\alpha\omega}{\gamma} \tag{3.34}$$

so that

$$\Re[m_x] = \frac{\omega}{\gamma\Delta\omega^{+}_{B0}} \frac{(B-B_0)\frac{\omega_{2,B0}}{\omega}\Delta\tau_{OOP} + \Delta^2(\alpha\tau_{OOP}+\tau_{IP})}{(B-B_0)^2+\Delta^2} \tag{3.35}$$

To finish it out let's explicitly write out what the experimentally measured signal will be:

$$\begin{aligned} V_{mix} &= (\Delta R)\sin(\phi)\cos(\phi)\Delta\phi(0)I_0 && (3.36)\\ &= \frac{(\Delta R)\sin(\phi)\cos(\phi)I_0\omega}{\gamma\Delta\omega^{+}_{B0}}\left[\frac{(B-B_0)\frac{\omega_{2,B0}}{\omega}\Delta\tau_{OOP} + \Delta^2(\alpha\tau_{OOP}+\tau_{IP})}{(B-B_0)^2+\Delta^2}\right] && (3.37)\\ &\approx \frac{(\Delta R)\sin(\phi)\cos(\phi)I_0\omega}{\gamma\Delta\omega^{+}_{B0}}\left[\frac{(B-B_0)\frac{\omega_{2,B0}}{\omega}\Delta\tau_{OOP} + \Delta^2\tau_{IP}}{(B-B_0)^2+\Delta^2}\right] && (3.38) \end{aligned}$$

The form to which we will actually fit is given by

$$V_{mix} = \frac{A\Delta(B-B_0) + S\Delta^2}{(B-B_0)^2+\Delta^2} \tag{3.39}$$

where A is the amplitude of antisymmetric Lorentzian and S is the amplitude of the symmetric Lorentzian. If the only contribution to the out of plane torques is the the Ørsted field then to an excellent approximation[5], the field felt by the magnet due to the current flowing through the non-magnet is that of an infinite sheet of current. Thus

$$\tau_{Ø,OOP} \approx \frac{\gamma\mu_0 J_c t_{nm}}{2} \tag{3.40}$$

recalling that J_c is the current density through only the non-magnetic layers. If the Ørsted field is the thing contributing to τ_{OOP} (***this is almost never true***) then we now have a path to 'self calibration' of the RF current. That is, we can relate on amplitude directly to the charge current and thus determine how much RF current actually reaches the device. This method is referred to as S/A. If we plug everything in we get (***again, this is rarely correct***)

$$\frac{S}{A} = \frac{\hbar}{2e}\frac{\gamma\xi_{SH}J_c}{M_s t_m a g}\frac{\omega}{\omega_{2,B0}}\frac{2}{t_{nm}\gamma\mu_0 J_c} \tag{3.41}$$

$$= \frac{\hbar}{e}\frac{\xi_{SH}}{\mu_0 M_s t_{mag} t_{nm}}\frac{\omega}{\omega_{2,B0}} \tag{3.42}$$

Rearranging

$$\xi_{SH} = \frac{S}{A}\frac{e\mu_0 M_s t_{mag} t_{nm}}{\hbar}\frac{\omega_{2,B0}}{\omega} \tag{3.43}$$

If we note that $\omega = \omega_0 \equiv \sqrt{\omega_{1,B0}\omega_{2,B0}}$ at resonance, then we can write the above equation as

$$\xi_{SH} = \frac{S}{A}\frac{e\mu_0 M_s t_{mag} t_{nm}}{\hbar}\sqrt{\frac{\omega_{2,B0}}{\omega_{1,B0}}} \tag{3.44}$$

If we plug in equilibrium torques for an in-plane ferromagnetic thin film with no in-plane anisotropy ($\omega_1 = B_{ext}$ and $\omega_2 = B_{ext} + M_{eff}$), we recover the form that matches [5]

$$\xi_{SH} = \frac{S}{A}\frac{e\mu_0 M_s t_{mag} t_{nm}}{\hbar}\sqrt{1 + \frac{M_{eff}}{B_{ext}}} \tag{3.45}$$

3.1.8 Symmetry Round III

One last thing to comment on here is angular dependences of τ_{OOP} and τ_{IP}. There are summarized in Table. 3.1. The results in Table. 3.1 then suggest that it is possible to separate the contribution of each symmetry of torque to each torque direction by looking at the angular dependence of the amplitudes of the symmetric and antisymmetric Lorentzians. As a reminder, the symmetry of the torque due to the Ørsted field is Rashba-like and so at the very least we expect a total angular dependence $\cos^2\phi\sin\phi$ in the antisymmetric component (Fig. 3.2(a)). As was discussed at the end of the previous chapter, the only direction of spins allowed in linear response to an electric field in high symmetry materials such as Pt is with Rashba-like symmetry. Thus, we expect for Pt to see an angular dependence of

Table 3.1: Functional form of the angular dependence of each type of possible torque.

τ_{IP}		τ_{OOP}	
Symmetry	Angular Dependence	Symmetry	Angular Dependence
$\underbrace{\hat{m} \times (\hat{y} \times \hat{m})}_{\text{Rashba-like}}$	$\cos\phi$	$\underbrace{\hat{m} \times \hat{y}}_{\text{Rashba-like}}$	$\cos\phi$
$\underbrace{\hat{m} \times (\hat{x} \times \hat{m})}_{\text{Dresselhaus-like}}$	$\sin\phi$	$\underbrace{\hat{m} \times \hat{x}}_{\text{Dresselhaus-like}}$	$\sin\phi$
$\underbrace{\hat{m} \times \hat{z}}_{\text{Z}}$	constant	$\underbrace{\hat{m} \times (\hat{z} \times \hat{m})}_{\text{Z}}$	constant

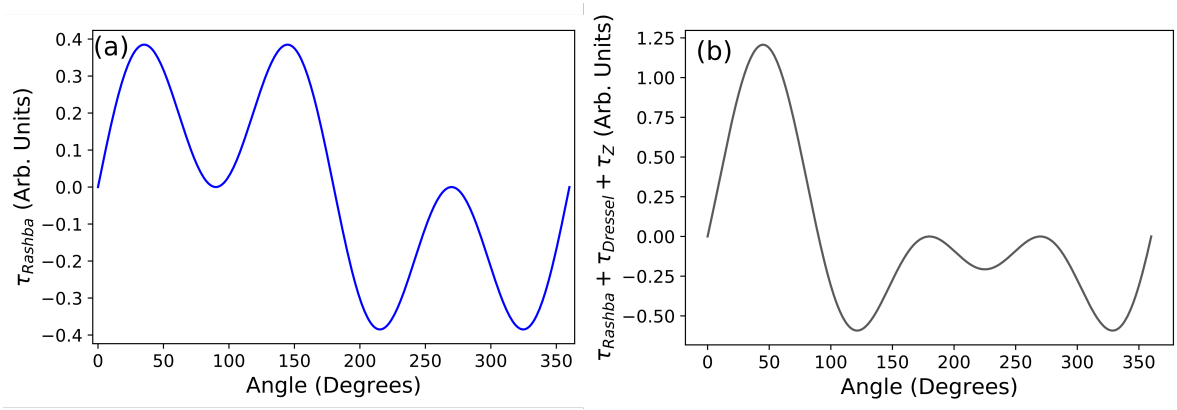

Figure 3.2: Angular dependence of Lorentzian amplitude as a result of a torque with (a) Rashba-like symmetry and (b) equal amounts of Rashba-like, Z, and Dresselhaus-like symmetry.

$\cos^2\phi \sin\phi$ in both the symmetric and antisymmetric amplitudes. Fig. 3.2(b) shows what the angular dependence would look like in the presence comparable amounts of both the Dresselhaus-like and Z symmetry torques.

3.1.9 Reality

This abstract formulation has been fun, but how do we actually use it to do experiments? The natural frequencies associated with ferromagnetic resonance are on the order of gigahertz. This should have been expected as the free electron gyromagnetic ratio is ≈ 28

GHz/T. At this frequency, the electrical wavelength is sufficiently short that standard "lumped element" is no longer sufficient to understand the behavior of electrical transmission.[10] Because of this the transmission properties of the cabling and connectors used can vary wildly with frequency. Sweeping magnetic field is then a better choice: sweeping frequency would mean that the resulting signal is convolved with the frequency dependence of the cabling. A magnet field sweep should have a marginal effect at most on the transmission of the network and thus make the interpretation of a single scan simpler.

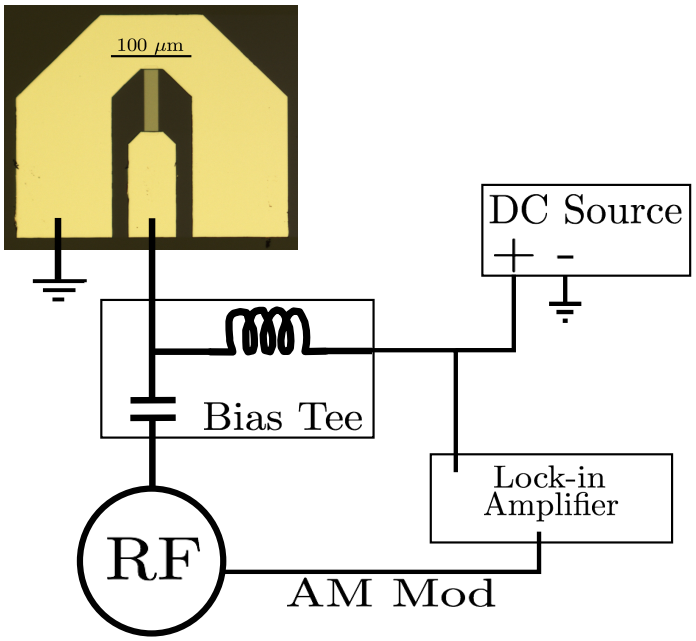

Figure 3.3: Schematic illustration of the circuit for (DC-biased) ST-FMR. RF (5-40 GHz) current is sourced from typically an Agilent (Keysight) E8254A signal generator through a bias tee to the sample. The mixing voltage is read out through the low frequency channel of the bias tee via lockin amplification (typically Signal Recovery 7265) to the amplitude modulation of the RF current. If a DC-bias is desired on top of the RF excitation (as described in the next section), a DC source can be added (typically a linear current source such as the venerable Keithley 220).

The most general circuit schematic for our measurement set up is shown in Fig. 3.3. The bias tee serves as a gate keeper, keeping the high frequency signal from uselessly flowing into the detection circuitry via an inductor, and preventing the DC voltage we

[10] *i.e.* not only does it matter *what* components you use, but also *where* you put them in circuit

are trying to detect from shorting across the low impedance output of the signal generator. The device itself is a bar of the ferromagnet/normal metal bilayer tens of microns wide and long. Ti/Pt ($\approx$ 150 nm thick) leads arranged in a ground/signal/ground (GSG) configuration form a terminated coplanar waveguide structure with the sample bar as terminal load. This symmetric configuration ensures that the any magnetic fields generated by current flowing in the leads approximately cancel at the sample. The distance between the sample and ground leads is fairly large and the magnitude of the current small so any such fields should be small anyway, but this choice requires little extra work on the part of the experimentalist and provides an experimental geometry that simplifies interpretation.

The minutiae of how to make contact to such a device and sweep a magnetic field at a given angle is discussed in Appendix. A

3.2 DC-Biased ST-FMR

While we have just seen that ST-FMR is a powerful tool for extracting the size and symmetry of the various current-induced torques generated by material, it is hamstrung by the limitation that it can be non-trivial to determine the scattering parameters of the RF cabling network and thus the amount of RF current that reaches the device. To circumvent this problem, one can apply a DC bias on top of the RF signal (a fairly minor experimental modification) and then sweep field normally. As we will see, this DC bias will shift the resonant field based on the out of plane torques present in the system and the apparent damping based on some of the in-plane torques. The key in the previous sentence is *some* in-plane torques. The ultimate conclusion of the following derivation is not necessarily intuitive given the effect of the torques on the symmetric and antisymmetric amplitudes of un-biased ST-FMR. Furthermore, I level a similar criticism at previous derivations in the literature, that they have not been completely general and/or sparse in terms of steps.

3.2.1 The non-equilibrium torques

Luckily for us, the derivation in the previous section did most of the heavy lifting. To take advantage of this we will use the same coordinate system and device geometry. The most difficult part of our task in the DC bias ST-FMR derivation is then to identify what changes about the non-equilibrium torques in presence of the DC bias. To be the most general, this will require us to actually consider all possible forms of the non-equilibrium torques explicitly. To keep the notation concise, torque components that oscillate with the RF driving current will have a subscript RF and torques arising from the DC bias will have a subscript DC. We will need to pick out the pieces that will resonant at only one multiple of the frequency as those are the only terms that get mixed down to a DC voltage

via the AMR. This means we need to discard terms either don't oscillate (have no factor m_y, m_z, or an RF torque) and terms which oscillate at more then one multiple of the driving frequency (have more than one factor m_y, m_z or an RF torque). Let's begin.

$$\overrightarrow{\tau}_{neq} = \frac{\hbar}{2e}\frac{\gamma}{M_s Vol_{mag}}\hat{m}\times(\overrightarrow{\sigma}_1\times\hat{m}+\overrightarrow{\sigma}_2) \tag{3.46}$$

where $\overrightarrow{\sigma}_1$ is a vector containing both the RF and DC spin currents for the anti-damping-like torques and $\overrightarrow{\sigma}_2$ is a vector containing both the RF and DC effective fields for the field-like torques. Doing all of the cross products yields

$$\overrightarrow{\tau}_{neq} = \frac{\hbar}{2e}\frac{\gamma}{M_s Vol_{mag}}\hat{m}\times\begin{pmatrix}\sigma_{y1}m_z-\sigma_{z1}m_y+\sigma_{x'2}\\ \sigma_{z1}m_x-\sigma_{x1}m_z+\sigma_{y'2}\\ \sigma_{x1}m_y-\sigma_{y1}m_x+\sigma_{z'2}\end{pmatrix} \tag{3.47}$$

$$= \frac{\hbar}{2e}\frac{\gamma}{M_s Vol_{mag}}\begin{pmatrix}m_y(\sigma_{x1}m_y-\sigma_{y1}m_x+\sigma_{z2})-m_z(\sigma_{z1}m_x-\sigma_{x1}m_z+\sigma_{y2})\\ m_z(\sigma_{y1}m_z-\sigma_{z1}m_y+\sigma_{x2})-m_x(\sigma_{x1}m_y-\sigma_{y1}m_x+\sigma_{z2})\\ m_x(\sigma_{z1}m_x-\sigma_{x1}m_z+\sigma_{y2})-m_y(\sigma_{y1}m_z-\sigma_{z1}m_y+\sigma_{x2})\end{pmatrix} \tag{3.48}$$

$$\approx \frac{\hbar}{2e}\frac{\gamma}{M_s Vol_{mag}}\begin{pmatrix}m_y(\sigma_{x1}m_y-\sigma_{y1}+\sigma_{z2})-m_z(\sigma_{z1}-\sigma_{x'1}m_z+\sigma_{y2})\\ m_z(\sigma_{y1}m_z-\sigma_{z1}m_y+\sigma_{x2})-(\sigma_{x1}m_y-\sigma_{y1}+\sigma_{z2})\\ (\sigma_{z1}-\sigma_{x1}m_z+\sigma_{y2})-m_y(\sigma_{y'1}m_z-\sigma_{z1}m_y+\sigma_{x2})\end{pmatrix} \tag{3.49}$$

where in the last step I have applied the assumption m_x=1, *i.e.* that the magnetization does not deviate much from its equilibrium direction (which is defined to be parallel to $\hat{x}$. Of critical note as well is that I have written all of the in-plane components of σ_1 and σ_2 with un-primed coordinates (that is, in the coordinates defined by the equilibrium position of the magnetization). This is to maintain consistency with the wording people use to describe the various torques. Practically, this means that we will need to replace the in-plane components of σ_1 and σ_2 in the un-primed basis with the their new projections onto the primed basis (coordinates defined by the device geometry). For notational cleanliness,

I will not do that step just yet so we don't have to carry around factors of sine and cosine throughout the whole derivation.

Next we keep only the components which respond at one multiple of the driving frequency as laid out earlier.

$$\overrightarrow{\tau}_{neq} = \frac{\hbar}{2e}\frac{\gamma}{M_s Vol_{mag}}\begin{pmatrix} m_y(-\sigma_{y1}+\sigma_{z2}) - m_z(\sigma_{z1}+\sigma_{y2}) \\ m_z(\sigma_{x2}) - (\sigma_{x1}m_y - \sigma_{y1} + \sigma_{z2}) \\ (\sigma_{z1} - \sigma_{x1}m_z + \sigma_{y2}) - m_y(\sigma_{x2}) \end{pmatrix} \tag{3.50}$$

$$= \tau_0 \begin{pmatrix} -m_y\sigma_{y1,DC} + m_y\sigma_{z2,DC} - m_z\sigma_{z1,DC} - m_z\sigma_{y'2,DC} \\ m_z\sigma_{x2,DC} - \sigma_{x1,DC}m_y + \sigma_{y1,RF} - \sigma_{z2,RF} \\ \sigma_{z1,RF} - \sigma_{x1,DC}m_z + \sigma_{y2,RF} - m_y\sigma_{x2,DC} \end{pmatrix} \tag{3.51}$$

where I have defined $\tau_0 \equiv \frac{\hbar}{2e}\frac{\gamma}{M_s Vol_{mag}}$. There is no avoiding what comes next, we need to insert the $\hat{y}$ (=τ_{IP}) and $\hat{z}$ (=τ_{OOP}) pieces into Eq. 3.14.

$$\begin{pmatrix} 0 \\ -i\omega m_y \\ -i\omega m_z \end{pmatrix} = \begin{pmatrix} 0 \\ m_z(i\omega\alpha - \omega_2) + m_z\tau_0\sigma_{x2,DC} - \tau_0\sigma_{x1,DC}m_y + \tau_0\sigma_{y1,RF} - \tau_0\sigma_{z2,RF} \\ -m_y(i\omega\alpha - \omega_1) + \tau_0\sigma_{z1,RF} - \tau_0\sigma_{x1,DC}m_z + \tau_0\sigma_{y2,RF} - m_y\tau_0\sigma_{x2,DC} \end{pmatrix} \tag{3.52}$$

Collecting terms,

$$\begin{pmatrix} 0 \\ m_y(-i\omega + \tau_0\sigma_{x1,DC}) \\ m_z(-i\omega + \tau_0\sigma_{x1,DC}) \end{pmatrix} = \begin{pmatrix} 0 \\ m_z(i\omega\alpha - \overbrace{\omega_2 + \tau_0\sigma_{x2,DC}}^{\equiv\omega_2'}) + \overbrace{\tau_0\sigma_{y1,RF} - \tau_0\sigma_{z2,RF}}^{\equiv\tau_{IP}'} \\ -m_y(i\omega\alpha - \underbrace{\omega_1 + \tau_0\sigma_{x2,DC}}_{\equiv\omega_1'}) + \underbrace{\tau_0\sigma_{y2,RF} + \tau_0\sigma_{z1,RF}}_{\equiv\tau_{OOP}'} \end{pmatrix} \tag{3.53}$$

The effect of the DC bias is starting to become apparent at this point. Most glaringly it is serving to renormalize the equilibrium torques. Our choice of abstract notation is unfortunately hiding the more intuitive explanation for what is happening. As a reminder, $\sigma_{x2,DC}$ corresponds to a static in-plane (effective) field generate by the current (*i.e.* a static out of plane torque), if there is a finite projection of that field along the external magnetic

field direction then the resonance field will be shifted by that amount. One subtle point here is that is statement only applies to in-plane (effective) fields, current-generated effective fields along $\hat{z}$ (*i.e.* σ_{z1}) do not shift the resonant field. So, the statement that *any* out-of-plane torque shifts the resonant field is strictly incorrect. We'll see what the other effects are further on down in our derivation.

Plugging m_z into m_y gives

$$m_y(-i\omega + \tau_0\sigma_{x1,DC}) = \frac{i\alpha\omega - \omega_2'}{-i\omega + \tau_0\sigma_{x1,DC}}(-m_y(i\alpha\omega - \omega_1') + \tau_{OOP}') + \tau_{IP}' \tag{3.54}$$

Rearranging

$$m_y(-\omega^2 - 2i\omega\tau_0\sigma_{x1,DC} + \overbrace{(\tau_0\sigma_{x1,DC})^2}^{\approx 0}) = (i\alpha\omega - \omega_2')(-m_y(i\alpha\omega - \omega_1') + \tau_{OOP}') + \tau_{IP}'(-i\omega + \tau_0\sigma_{x1,DC}) \tag{3.55}$$

Again assuming α^2 is negligible, making the definitions $\omega_0^{2'} \equiv \omega_1'\omega_2'$ and $\omega^{+'} \equiv \omega_1' + \omega_2'$, and collecting all the m_y terms on the left hand side

$$m_y(-\omega^2(1 + \overbrace{\alpha^2}^{\approx 0}) - 2i\omega\tau_0\sigma_{x'1,DC} - i\alpha\omega\overbrace{(\omega_1' + \omega_2')}^{\equiv\omega^{+'}} + \overbrace{\omega_1'\omega_2'}^{\equiv\omega_0^{2'}}) = (i\alpha\omega - \omega_2')\tau_{OOP}' + \tau_{IP}'(-i\omega + \tau_0\sigma_{x1,DC}) \tag{3.56}$$

This will finally take us to a more recognizable form:

$$m_y = \frac{(i\alpha\omega - \omega_2')\tau_{OOP}' + \tau_{IP}'(-i\omega + \tau_0\sigma_{x1,DC})}{-\omega^2 - 2i\omega\tau_0\sigma_{x1,DC} - i\alpha\omega\omega^{+'} + \omega_0^{2'}} \tag{3.57}$$

Some suggestive manipulation yields,

$$m_y = \frac{(i\alpha\omega - \omega_2')\tau_{OOP}' + \tau_{IP}'(-i\omega + \tau_0\sigma_{x1,DC})}{\omega_0^{2'} - \omega^2 - i\omega\omega^{+'}\underbrace{\left(\alpha + \frac{2\tau_0\sigma_{x1,DC}}{\omega^{+'}}\right)}_{\equiv\alpha'}} \tag{3.58}$$

Defining $\alpha' = \alpha + \frac{2\tau_0\sigma_{x1,DC}}{\omega^{+'}}$ finally completes the story. Now we can see that the effect of an in-plane, damping-like spin torque is to modify the damping proportion to the DC bias.

Of critical note is that torques that rely on what would be out of plane (effective) field do not modify the damping. The statement that *any* in-plane torque modifies the damping is incorrect.

We are not done yet, we really should find the real part and then expand out the resonant field in terms of field so that we can apply this experimental data. Making the denominator real we get

$$m_y = \frac{\tau'_{OOP}(i\alpha\omega - \omega'_2)(\omega_0^{2'} - \omega^2 + i\omega\omega^{+'}\alpha') + \tau'_{IP}(\omega_0^{2'} - \omega^2 + i\omega\omega^{+'}\alpha')(-i\omega + \tau_0\sigma_{x1,DC})}{(\omega_0^{2'} - \omega^2)^2 + \omega^2\omega^{+2'}\alpha^{2'}} \tag{3.59}$$

Finally taking the real part we get

$$\Re[m_y] = \frac{\tau'_{OOP}(\omega'_2(\omega^2 - \omega_0^{2'}) - \overbrace{\cancel{\alpha\alpha'\omega^{+'}\omega^2}}^{\approx 0}) + \tau'_{IP}(\omega\omega^{+'}\omega\alpha' + \tau_0\sigma_{x1,DC}(\omega_0^{2'} - \omega^2))}{(\omega_0^{2'} - \omega^2)^2 + \omega^2\omega^{+2'}\alpha^{2'}} \tag{3.60}$$

$$\approx \frac{\tau'_{OOP}\omega'_2(\omega^2 - \omega_0^{2'}) + \tau'_{IP}(\omega^{+'}\omega^2\alpha' + \tau_0\sigma_{x1,DC}(\omega_0^{2'} - \omega^2))}{(\omega_0^{2'} - \omega^2)^2 + \omega^2\omega^{+2'}\alpha^{2'}} \tag{3.61}$$

To expand about the resonant field we should note, as I have done early in this derivation, that the effect of the DC is relatively minor. The only thing that really merits explicit discussion is expansion of $\omega_0^{2'}$:

$$\omega_0^{2'} \approx \omega_0^{2'}\Big|_{B=B_0} + (B - B_0)\left.\frac{d(\omega_0^{2'})}{dB}\right|_{B=B_0} \tag{3.62}$$

The second term on the right hand side is the same as before. The perturbations due to the DC bias are small and so the corrections are minor. The more nuanced consideration here is what B_0 is.

In the derivation for unbiased ST-FMR the result was intuitive, B_0 was the field at which $\omega_0^2\big|_{B=B_0} == \omega^2$, but now each equilibrium torque is modified by $\tau_0\sigma_{x'2,DC}$. Because each equilibrium torque is modified in the same way we can think of this as a modification to the external field (which it literally is in the case of the Ørsted field). Thus, B_0 becomes

$B_0' = B_0 + \tau_0\sigma_{x2,DC}/\gamma$. Finally putting everything together we get

$$\Re[m_y] \approx \frac{\tau'_{OOP}\gamma\omega_{B0}^{+'}\omega'_{2,B0}(B - B_0') + \tau'_{IP}\omega_{B0}^{+'}(\omega^2\alpha' + \tau_0\sigma_{x1,DC}\gamma(B - B_0'))}{\gamma^2\omega_{B0}^{+2'}(B - B_0)^2 + \omega^2\omega_{B0}^{+2'}\alpha^{2'}} \tag{3.63}$$

3.2.2 Implications

Before discussing experimental realities, let's first consider the implications above formula. By doing a "normal" ST-FMR experiment multiple times at different DC biases, we should be able to extract the in-plane torques with Rashba or Dresselhaus symmetry from $\frac{d\alpha'}{dI}$ and the out-of-plane torques with Rashba or Dresselhaus symmetry from $\frac{dB_0'}{dI}$. For a thin film system without any magnetic anisotropy this leads to

$$\frac{d\alpha'}{dI_{DC}} = \frac{\gamma\hbar(\xi_{IP,Rashba}\sin(\phi) + \xi_{IP,Dressel}\cos(\phi))}{eM_sVol_{mag}(2B_0 + M_{eff})} \tag{3.64}$$

where $\xi_{IP,Rashba}$ and $\xi_{IP,Dressel}$ correspond to the spin Hall efficiencies for in-plane (anti-damping) torques with Rashba-like and Dresselhaus-like symmetries, respectively. Typically one actually gets $\frac{d\Delta}{dI_{DC}}$ from the experiment. If we assume that any inhomogenous broadening of the linewidth doesn't have a DC-bias dependence then we can use the original definition of Δ (Eq. 3.34), to write $\frac{d\alpha'}{dI_{DC}} = \frac{\gamma}{\omega}\frac{d\Delta'}{dI_{DC}}$. Solving for the spin Hall efficiencies gives

$$\xi_{IP,Rashba}\sin(\phi) + \xi_{IP,Dressel}\cos(\phi) = \frac{d\Delta}{dI_{DC}}\frac{eM_sVol_{mag}\omega(2B_0 + M_{eff})}{\hbar} \tag{3.65}$$

From the resonant field shift we get

$$\frac{dB_0}{dI_{DC}} = \frac{\hbar(\xi_{OOP,Rashba}\sin(\phi) + \xi_{OOP,Dressel}\cos(\phi))}{2eM_sVol_{mag}} \tag{3.66}$$

Solving this for the spin Hall efficiencies yields

$$\xi_{OOP,Rashba}\sin(\phi) + \xi_{OOP,Dressel}\cos(\phi) = \frac{dB_0}{dI_{DC}}\frac{2eM_sVol_{mag}}{\hbar} \tag{3.67}$$

These equations are wonderful in theory in that do not depend on the amplitude of the ST-FMR signal nor the RF current which reaches the device. Thus we do not need to figure out the scattering parameters of the cable network to get at the spin Hall effect from ST-FMR measurement, we can just watch how the resonance lineshape changes and the resonance field moves. This also has the added benefit of allowing us to correct the S/A ratio for extra out of plane torques beyond the Ørsted field. Because we can be reasonably confident that all of the DC bias reaches the device we can calculate what the resonant field shift due to only the Ørsted field should be. Then to get the antisymmetric amplitude due to only the Ørsted field $A_{Ø}$

$$A_{Ø} = A\frac{\tau_{OOP,Ø}}{\tau_{OOP,Ø} + \tau_{OOP,extra}} \tag{3.68}$$

we get $\tau_{Ø} + \tau_{extra}$ from the resonant field shift we measure, and we can calculate $\tau_{Ø}$. Thus the corrected S/A ratio is given by

$$\frac{S}{A_{Ø}} = \frac{S}{A}\frac{\tau_{OOP,measured}}{\tau_{Ø,calculated}} \tag{3.69}$$

3.2.3 Reality

Not too much changes from an experimental design stand point when doing DC-bias ST-FMR compared to ST-FMR. The biggest and most critical change is that the effects of heating become markedly relevant. Normally to get excellent signal to noise we amplitude modulate the RF excitation current and lock in to the result oscillation of the mixing voltage. Because RF is already an oscillatory signal, the way amplitude modulation works (at full depth) is to oscillate from no power delivered to max power delivered. One practical consequence of this is that the heating of the sample occurs at the same frequency into which the lock in is locking as opposed to the more tradition case where the AC excitation oscillates about zero and the effects of heating are at twice the frequency. Luckily, the

effect of heating does not seem to too strongly affect the measurement and interpretation of ST-FMR. However, in the case of DC-bias ST-FMR, the DC-bias gets multiplied by the resistance change at the lock in frequency due to heating. This gives rise to a large background voltage that contaminates the lock in signal. For sufficiently high currents, the lock in amplifiers we use do not have enough dynamic range to sort out the μV mixing voltage signal from the potential mV heating signal. This sets an experimental limit on the highest current one can go to (which may be less than what the device can handle).

In addition, the presence of a digital current source (*i.e*. not a battery) adds a non-trivial amount of noise to the measurement. This is especially noticeable in the switched-mode current sources[11] which dominate the market today. However, the 1980's were a halcyon time and the linear current sources[12] that dominated at the time are substantially less noisy. Luckily, the Ralph group has several digital current sources from that era (Keithley 220) and switching to using them has helped ameliorate some of the added noise issue.

[11]That is, generating the current by filtering a square wave signal with varying duty cycle

[12]That is, using a network of transistors to control the output current. Thanks to Brad Ramshaw for sharing this gem of information with me

3.3 Magneto-Optical Kerr Effect Measurements

We motivated the previous section on DC bias ST-FMR by pointing out that it can be difficult to determine the RF scattering parameters the cabling and noting that by applying a DC bias on top of the RF we can in some cases extract current induced torques from the ST-FMR lineshape alone. While that is useful, it still is an RF technique,[13] and there are still some questions as to the interpretation of the result of the DC bias results which will be discussed in the results sections later. It would be wonderful if we could avail ourselves of at least one another technique that is not resonance based and fundamentally different in its read out. Of course the section heading has spoiled the punchline, one such technique is using the magneto-optical Kerr effect (MOKE) to directly image the motion of the magnetization of the ferromagnet.

In addition to being a quasi-DC technique, MOKE also offers a readout that is immune to any artifacts associated with read out through resistance changes or Hall voltages. Unfortunately with MOKE, we trade one experimental problem for another. Whereas it was difficult to quantitatively determine the scattering parameters of the RF cabling for ST-FMR, it is difficult to quantitatively relate the absolute Kerr rotation measured to magnetic motion. Luckily, in the case of an in-plane ferromagnetic thin film, we can somewhat trivially get around this problem[66]. As has been the case for the previous two experiments, the math has already been presented in the literature but lacks generalization to arbitrary torques. For this reason, I will again drag the curious reader through a tedious forest of integrals and approximations.

[13] Which is to say it requires precision, care, and expensive components

3.3.1 Magneto-Optics

So, what is MOKE? Over 100 years ago, John Kerr found that the polarization of light reflected off a ferromagnetic magnetic can be rotated according to the orientation of the magnetization of the magnet[67]. This effect arises from complex, off-diagonal elements in the relative permitivity tensor, $\overline{\epsilon}$, of the magnetic material[68].

$$\overline{\epsilon} = \begin{pmatrix} \epsilon_{xx} & \epsilon_{xy} & \epsilon_{xz} \\ -\epsilon_{xy} & \epsilon_{yy} & \epsilon_{yz} \\ -\epsilon_{xz} & -\epsilon_{yz} & \epsilon_{zz} \end{pmatrix} \tag{3.70}$$

If we define $\hat{z}$ to be perpendicular to the surface of the magnet then we can simplify our analysis by focusing only on light that is perpendicularly incident onto the surface of the magnet (the so-called polar MOKE or p-MOKE geometry). In this case, we need only concern ourselves with the upper left 2×2 part of $\overline{\epsilon}$.[14] For consistency with the *corpus* of optics literature, we will also identify $\hat{x}$ with the direction perpendicular to the plane of incidence (relabeled s) and identify $\hat{y}$ with the direction parallel to the plane of incidence (relabeled p).[15]

$$\overline{\epsilon} \to \begin{pmatrix} \epsilon_{ss} & \epsilon_{sp} \\ -\epsilon_{sp} & \epsilon_{pp} \end{pmatrix} \tag{3.71}$$

These off-diagonal components are proportional to m_z and indicate that s and p are not eigenstates of polarization inside the magnet. Furthermore, since the resulting eigenvalues are not degenerate, the eigenstates (which happens to be right and left circularly polarized light) have different indices of refraction. In the case of linear polarized light (equal parts right and left circularly polarized light), this then has the effect of rotating

[14] Because light has no longitudinal mode

[15] s is from the German *senkrecht* meaning perpendicular, and p is from the German *parallel* meaning parallel. One may also note that the geometry I have described (p-MOKE) suffers from what amounts to gimbal lock with respect to these definitions: one cannot define a plane with a single line. In this thesis, the plane of incidence will be defined as the plane parallel to the plane of optics table.

Table 3.2: Jones matrices for relevant optical elements. For the polarizers and half wave plates, the angle θ is the polarization axis and the fast axis, respectively.

Component	Matrix
Polarizer	$\begin{pmatrix} \cos^2\theta & \sin\theta\cos\theta \\ \sin\theta\cos\theta & \sin^2\theta \end{pmatrix}$
$\frac{1}{2}$ plate	$\begin{pmatrix} \cos 2\theta & \sin 2\theta \\ \sin 2\theta & -\cos 2\theta \end{pmatrix}$
MOKE	$\begin{pmatrix} r_{ss} & r_{sp} \\ -r_{ps} & r_{pp} \end{pmatrix}$

the polarization and making the polarization elliptical. This has the effect of the giving rise to off diagonal elements$\propto m_z$ in the reflectivity tensor

$$\bar{r} = \begin{pmatrix} r_{ss} & r_{sp} \\ -r_{sp} & r_{pp} \end{pmatrix} \tag{3.72}$$

If we consider s-polarized light in particular, then the Kerr rotation is given by

$$\phi = \phi' + i\phi'' = \frac{r_{sp}}{r_{pp}} \tag{3.73}$$

where ϕ' is the Kerr rotation and ϕ'' is the Kerr ellipticity. This is in direct analogy to the magneto-conductivity where such off diagonal elements in the conductivity tensor give rise to the Hall effect[62].

3.3.2 Using MOKE

To extract the spin Hall effect using MOKE, first we need to devise an experimental geometry that will be sensitive to small rotations of reflected linearly polarized light to which MOKE gives rise.[16] One such geometry is shown in Fig. 3.4. To see how this gives rise

[16]One concern might be that our films are composed of multilayer thin films with film thickness less than skin depth of the material for visible light. It turns our that the modification is minor and doesn't

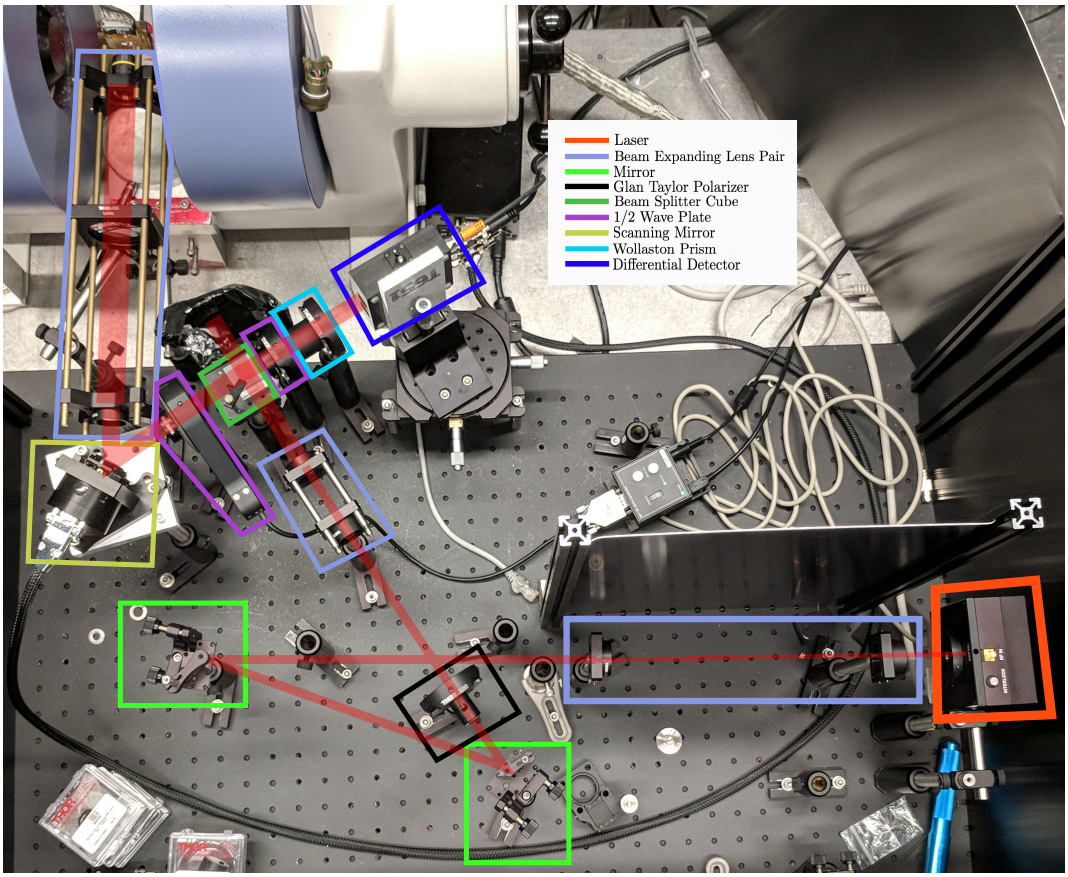

Figure 3.4: Annotated picture of the Ralph Group MOKE set up. Laser light from a diode laser in a thermo-electrically cooled (TEC) laser diode mount with an anamorphic prism pair (red). The laser then passes through a beam expanding set of lenses (teal), bounces off of two mirrors (lime green) and then gets polarized by the Glan Taylor polarizer (black). The light then passes through another beam expanding lens set and is sent through a beam splitter cube. 10% of the light if reflected through a half wave plate (purple) on a motorized mount and then is bounced off of the scanning mirror (dark yellow). The beam is goes through one final beam expansion through a 4f lens pair and is focused on the sample with a 20x objective. The reflected light retraces its steps and 90% goes through the un-motorized half wave plate at 22.5 degree to the *s* polarization and through the the Wollaston prism (teal) to final reach the detector (blue).

to a useful experiment, let us make use of the Jones matrix formalism for optical components (summarized in Table. 3.2). In the Jones calculus we note that the polarization can be represented by a two component vector of two perpendicular polarized waves. The polarizer in Fig. 3.4 takes the unpolarized light from the laser and makes it purely[17]

appreciably change our analysis [62, 69]

[17]The extinction ratio on our polarizer is 10^5:1

s polarized

$$E_{initial} = \begin{pmatrix} 1 \\ 0 \end{pmatrix} \tag{3.74}$$

To this initial state we apply a $\frac{1}{2}$-wave plate at θ_1=22.5 degrees to rotate the *s* polarized light to be equal parts *s* and *p* in order to avoid quadratic MOKE (QMOKE) effects. Then the light hits the sample and the beam gets reflected and Kerr rotated. Passing through the $\frac{1}{2}$-wave plate again undoes the initial rotation then a $\frac{1}{2}$ wave plate at θ_2=22.5 degrees (the analyzer) rotates the polarization to be nearly equal parts *s* and *p modulo* the Kerr rotation. In explicit symbols for posterity

$$E_{final} = \begin{pmatrix} \cos 2\theta_2 & \sin 2\theta_2 \\ \sin 2\theta_2 & -\cos 2\theta_2 \end{pmatrix} \begin{pmatrix} \cos 2\theta_1 & \sin 2\theta_1 \\ \sin 2\theta_1 & -\cos 2\theta_1 \end{pmatrix} \begin{pmatrix} r_{ss} & r_{sp} \\ -r_{ps} & r_{pp} \end{pmatrix} \begin{pmatrix} \cos 2\theta_1 & \sin 2\theta_1 \\ \sin 2\theta_1 & -\cos 2\theta_1 \end{pmatrix} \begin{pmatrix} 1 \\ 0 \end{pmatrix} \tag{3.75}$$

$$= \begin{pmatrix} r_{ss}\cos 2\theta_2 + r_{sp}\sin 2\theta_2 \\ r_{sp}\cos 2\theta_2 - r_{ss}\sin 2\theta_2 \end{pmatrix} \tag{3.76}$$

plugging in θ_2=22.5 degrees

$$E_{final} = \begin{pmatrix} \frac{r_{ss}-r_{sp}}{\sqrt{2}} \\ \frac{r_{ss}+r_{sp}}{\sqrt{2}} \end{pmatrix} \tag{3.77}$$

So now we have the electric field of the Kerr rotated beam just before it hits the Wollaston prism. After the light passes through the prism it gets split into its *s* and *p* components and each component is sent to a separate photodiodes on the split diode detector. The detector then subtracts the intensities ($\propto E_{final}^2$) incident on its photodiodes and that is what we measure. In symbols

$$V_{signal} \propto \begin{pmatrix} \frac{r_{ss}-r_{sp}}{\sqrt{2}} & \frac{r_{ss}+r_{sp}}{\sqrt{2}} \end{pmatrix} \begin{pmatrix} 1 & 0 \\ 0 & -1 \end{pmatrix} \begin{pmatrix} \frac{r_{ss}-r_{sp}}{\sqrt{2}} \\ \frac{r_{ss}+r_{sp}}{\sqrt{2}} \end{pmatrix} \tag{3.78}$$

$$\propto \frac{1}{2}(r_{ss} - r_{sp})^2 - \frac{1}{2}(r_{ss} + r_{sp})^2 \tag{3.79}$$

$$\approx 2r_{ss}r_{sp} \tag{3.80}$$

Recall that r_{sp} is our quarry: it is $\propto m_z$ and thus contains information on the in-plane torques and the Ørsted field. So by applying an oscillating current to the device and locking in to the output of the split diode detector we should be sensitive to the effects of current-induced in-plane torques on the magnet.

Now, to get a reasonable signal one typically needs to apply a pretty substantial current density (on the order of 10^{10} A/m^2). This will definitely lead to heating and non-trivially effect the component r_{ss} with time. However, because heating effects do note care about the sign of the current, that oscillation will occur on the second harmonic and thus our signal on the first harmonic should be immune to heating. If you recall the story of DC-Biased ST-FMR in the previous section, you might note that this outcome is slightly different with regards to heating. In the DC-Biased case and effect of heating ended up on the first harmonic. The difference there is that the parameter being modulated was the amplitude of the RF signal which allowed the resistance change due to heating to oscillate at the same frequency; here we are locking into the driving signal itself.

3.3.3 The Actual Signal

So far in this section we have discussed MOKE in general and the vagaries of heating, but we have yet to actually touch upon what the actual signal will be.[18] To make progress towards that goal, let us break out for the third time the LLGS equations[64] in its pure[19]

[18] In some sense I think this highlights the potential of MOKE, it is a direct probe of the magnetization. We needn't resort to tricks (albeit clever ones) to read out the effect of the torques on the magnet. We can (in theory) just directly measure the magnetization.

[19] *i.e.* before we have formed the *ansatz* of oscillating solutions

form for an in-plane magnet, reproduced below

$$\begin{pmatrix} 0 \\ \dot{m}_y \\ \dot{m}_z \end{pmatrix} = \begin{pmatrix} 0 \\ -\alpha\dot{m}_z - m_z\omega_2 + \tau_{IP} \\ \alpha\dot{m}_y + m_y\omega_1 + \tau_{OOP} \end{pmatrix} \tag{3.81}$$

This time, we will be applying an AC current on the order of 1 KHz at most, far slower than the natural frequency scale of GHz set by γ. Thus we can approximate the time derivatives as 0 and look for static solutions. Without using quadratic MOKE we are also not sensitive to out-of-plane torques so we can ignore those as well.[20] This leaves

$$\begin{pmatrix} 0 \\ 0 \\ 0 \end{pmatrix} = \begin{pmatrix} 0 \\ -m_z\omega_2 + \tau_{IP} \\ m_y\omega_1 \end{pmatrix} \tag{3.82}$$

It almost seems too easy given the veritable algebraic keelhauling we have endured in our previous sorties with the LLGS equations. This is it, though. Wistful reverie complete, we get

$$m_z = \frac{\tau_{IP}}{\omega_2} \tag{3.83}$$

$$= I_{total}\frac{\tau_0(\xi_{Rashba}\cos\phi + \xi_{Dresselhaus}\sin\phi + \xi_Z)X + \tau_{\hat{z},Oe}(x)}{\gamma(B_{ext} + M_{eff})} \tag{3.84}$$

where I have assumed no additional anisotropy in this case, I_{total} is the total current flowing through the device, $\tau_0 \equiv \frac{\hbar}{2e}\frac{\gamma}{M_s Vol_{mag}}$ as a reminder, X is the fraction of the current that flows through just the non-magnetic layer, and $\tau_{\hat{z},Oe}(x)$ is γ times the position-dependent, out-of-plane magnetic field in the bilayer arising from the current flowing through it. Just to be clear, the lack of explicit position dependence on the rest of the terms is deliberate, those terms give rise to uniform shift in $\hat{z}$ everywhere along the bar.

[20] Why have I ignored the possibility of using quadratic MOKE twice now? The reason will be painfully apparent two chapters from now, but for the impatient it's because the experiment for which MOKE served as an essential tool has a negligible QMOKE signal. Furthermore, QMOKE was covered in an earlier thesis (Alex Melnik) in our group and I don't think my retelling offers any unique insight.

Before we head into the breach that is magnetostatics to figure out $\tau_{\hat{z},Oe}(x)$, let's consider the symmetry of the terms in the numerator. If the magnetization is parallel to the current, $\phi = 0$ so $\xi_{Dresselhaus} \sin\phi$ doesn't contribute, whereas ξ_{Rashba}, ξ_Z, and $\tau_{\hat{z},Oe}(x)$ do. If we flip the magnetization 180 degrees, then $\xi_{Rashba} \rightarrow -\xi_{Rashba}$ but every other term remains unchanged. If we were to apply the external field perpendicular to the current the only change is that we would trade sensitivity to ξ_{Rashba} for sensitivity to $\xi_{Dresselhaus}$. This suggests an experimental plan, if we take two traces at opposite fields we should be able to extract each component by its parity.

Now let us deal with $\tau_{\hat{z},Oe}(x)$. Because we are concerned with the magnetic field within the magnetic layer of the film and the film is much thinner than the width and length of the device, we may treat it as composed of infinite lines of current each carrying $I_{wire} = \frac{I_{total}}{tw}$ where I_{total} is the total current through the bilayer, t is the total thickness of the bilayer, and w is the width of the device. Implicit in the above definition is the rather rosy assumption that the current density through the sample is uniform. This is of course almost never going to be the case as the resistivity of the magnetic layer is unlikely to match the resistivity of the material generating the spin torques. But, again, t is normally at least 1000 times w in a given system. Thus, to an excellent approximation, it doesn't matter. For this same reason, the contributions to the magnetic field from the line currents stacked on top of each other in $\hat{z}$ will also all be approximately the same so we can do that integral trivially and it reduces the problem to the sum of infinite line currents aligned next to each other in $\hat{y}$ with current $I'_{wire} = \frac{I_{total}}{tw} t = \frac{I_{total}}{w}$. According to Ampere's law, the magnetic field $\overrightarrow{B}$ arising from an infinite line current is

$$\overrightarrow{B}(\overrightarrow{r}) = \frac{\mu_0 I_{wire}}{2\pi} \frac{\overrightarrow{r} \times \hat{I}}{|r|^2} \tag{3.85}$$

where $\overrightarrow{r}$ is the radial vector from the line current, μ_0 is the permeability of free space, and $\hat{I}$ is the unit vector pointing along the current flow direction. To determine $\overrightarrow{B}(x)$ we just need to integrate Eq. 3.85 across the slab. What we really care about is the magnetic field

in the magnetic layer. If we consider a bar with equal thickness of magnet and spin Hall material then we are interested in the field at t from the center of the slab. If we define our $\hat{x}$ and $\hat{z}$ origin to be the center and middle of the bar, respectively, then the total magnetic field at each point is given by

$$\overrightarrow{B}(x) = \frac{\mu_0 I_{total}}{2w\pi} \int_{-\frac{w}{2}}^{\frac{w}{2}} dx' \frac{(t\hat{y} - (x - x')\hat{z})}{(t^2 + (x - x')^2)} \tag{3.86}$$

Luckily, each of the vector components' integrals has closed form solutions

$$B_y(x) = \frac{\mu_0 I_{total}}{2w\pi} \left(\tan^{-1}\left(\frac{x + w/2}{t}\right) - \tan^{-1}\left(\frac{x - w/2}{t}\right)\right) \tag{3.87}$$

$$B_z(x) = -\frac{\mu_0 I_{total}}{4w\pi} \left(\ln\left(t^2 + (x + w/2)^2\right) - \ln\left(t^2 + (x - w/2)^2\right)\right) \tag{3.88}$$

These are perhaps somewhat difficult to parse by inspection so their graphical forms are shown in Fig. 3.5. B_y should hopefully make sense: except at the edges we have what amounts to an infinite sheet of current and a uniform in-plane-directed field is the necessary result. B_z is a little bit more interesting. As we just noted, we have effectively an infinite sheet of current which we might expect should have no $\hat{z}$ directed field at all. The reason we don't is that we don't have the same cancellation we do in-plane. Near the edges the out of plane fields coherently sum whereas in-plane one has an incoherent mess. This also reveals what sets the scale of this coherent summation. If there was no t^2 in ln then at the edges of the device ($\pm w/2$) then B_z would diverge.

At this stage we should ask if the magnet will even allow a spatial variation of its magnetization out of plane. The answer is of course yes or else this whole section would have been an exercise in futility. The reason is that the exchange length of Py is on the order of a few nm and our device is much larger than that, so we should have no trouble perturbing the magnet.

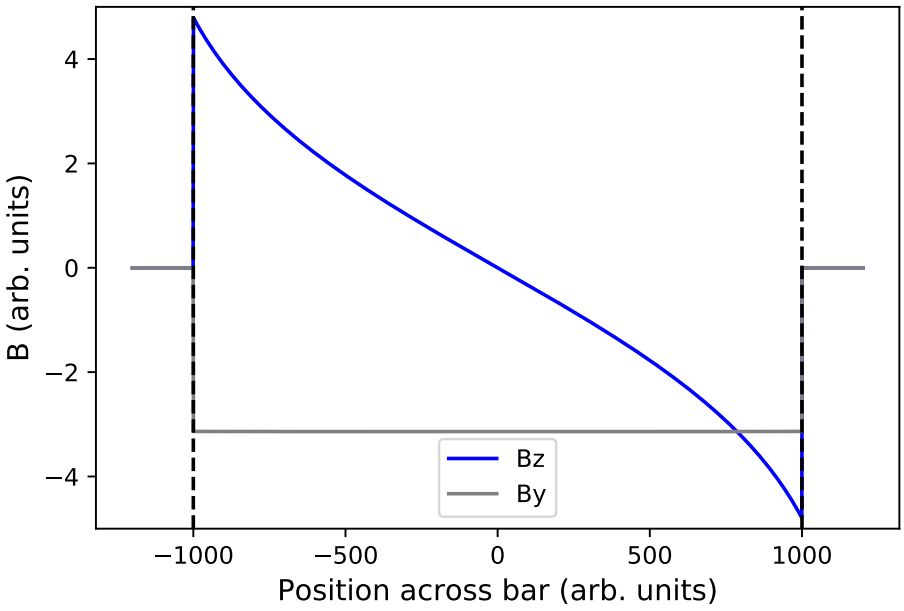

Figure 3.5: Plots of B_z and B_y using the functional forms of Eqns. 3.88 and 3.87, respectively. The vertical dashed lines represent the edges of the device.

Now that we have sorted out what we expected the magnet to do we should briefly consider the physical limitations of MOKE itself. The most important thing is the fact that our beam has a finite size. We assume a 2D gaussian beam of the form

$$G(x,y) = A * e^{(x^2+y^2)/\sigma^2} \tag{3.89}$$

where A is the amplitude and σ is the beam width. Then the resulting MOKE signal at a given point is given by m_z convolved with this beam shape,

$$V_{MOKE} \propto \int\int dxdyG(x,y)m_z(x) \tag{3.90}$$

$$\propto \int\int dxdye^{(x^2+y^2)/\sigma^2}m_z(x) \tag{3.91}$$

$$\propto \int dxe^{(x^2)/\sigma^2}m_z(x) \tag{3.92}$$

$$\propto \int dxG(x)m_z(x) \tag{3.93}$$

where in the last lines we have done the y integral as m_z has no y dependence. The remaining x integral has no closed form solution. The algorithmic way to get around this

is to Fourier transform so the convolution becomes a product, multiply, and then inverse Fourier transform back, all numerically of course. The resulting total MOKE signal is simulated in Fig. 3.6.

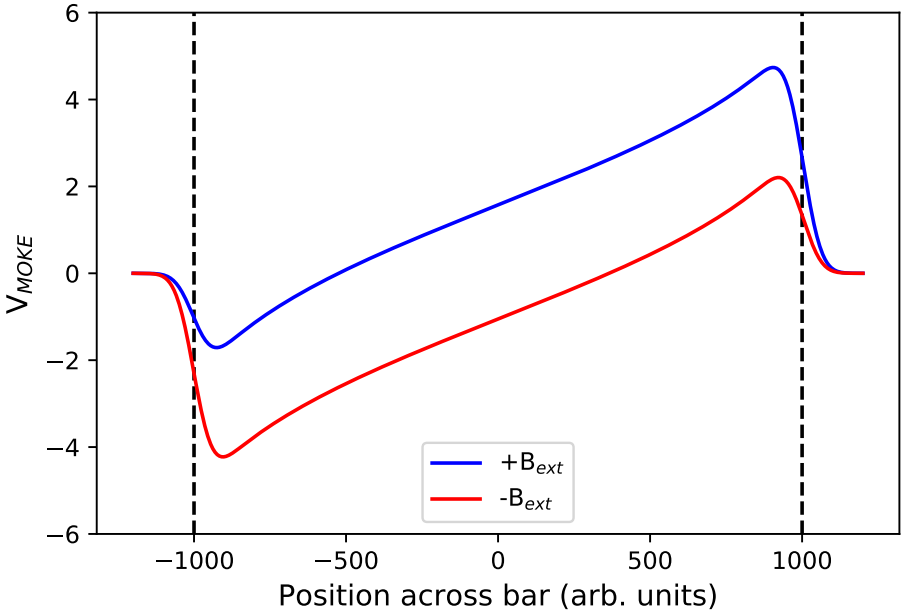

Figure 3.6: Plot of the MOKE signal at opposite external magnetic fields for a magnet experience all three of the torques described in Eq 3.84. To simulate this signal the magnetization is convolved with a gaussian beam with beam width 1/60 of the device width.

3.3.4 The Measurement Scheme

We now have all the ingredients to actually derive a useful experimental plan to extract the magnitude of the in-plane current-induced torques. Key to this is the notion that the spin Hall spin transfer torque changes sign under field reversal while the Ørsted field signal does not. This suggests that a robust way to tell the two apart is to take scans at opposite magnetic fields and take the sum and difference of them. The sum should contain information on $B_z(x)$ and possibly τ_z while the difference should only contain info on τ_{SH}. Since we have an analytic form for $B_z(x)$ we can use the data gained from

$B_z(x)$ component of the sum signal to get the quantitative relationship between m_z and measured signal. This is easier said than done, of course. In our case, our MOKE set up lacks a sufficiently powerful laser to have a high signal to noise. The primary consequence of this is that fitting the resulting data can prove challenging as the fit function is fairly complex and involves a convolution operation. On top of this, we do ourselves no favors noise-wise by taking the difference between two signals.

To overcome these challenges we note that convolution is area preserving. This suggests that if we can come up with an analytical solution to area under the sum and difference curves than we may be able to get away with numerically integrating the resulting signal and comparing areas. The sum signal contains information about $B_z(x)$ and τ_z. For all intents and purposes, τ_z is a constant over the bar and so should represent a DC shift of the sum signal. In practice, this piece is typically extracted by calculating the mean of the sum signal. This has the side effect of also allowing to subtract off this shift to leave behind just the component $\propto \gamma B_z(x)$. If we look at the signal from the left edge of the device to the device midpoint, we can calculate area as

$$A_{sum} = \frac{1}{B_{ext} + M_{eff}} \int_{-w/2}^{0} dx(B_z(x) + B_z(x)) \tag{3.94}$$

$$= \frac{\mu_0 I_{total}}{2\pi w(B_{ext} + M_{eff})} \left[t \tan^{-1}\left(\frac{x - w/2}{t}\right) - t * \tan^{-1}\left(\frac{x + w/2}{t}\right) + \frac{1}{2}(x - w/2)\ln\left(t^2 + (x - w/2)^2\right) - \frac{1}{2}(x + w/2)\ln\left(t^2 + (x + w/2)^2\right) \right]\Bigg|_{-w/2}^{0} \tag{3.95}$$

$$= \frac{\mu_0 I_{total}}{2\pi w(B_{ext} + M_{eff})} \left[t \tan^{-1}\left(\frac{w}{2t}\right) + t \tan^{-1}\left(\frac{w}{t}\right) - \frac{w}{2}\ln\left(t^2 + w^2/4\right) + \frac{w}{2}\ln\left(t^2 + w^2\right) \right] \tag{3.96}$$

$$\approx \frac{\mu_0 I_{total} ln(4)}{4\pi(B_{ext} + M_{eff})} \tag{3.97}$$

where the first line serves as a reminder that this signal is the sum of two curves and the last step we invoke the reality that $t \ll w$. This is of course only half of the device, but the

other half has the opposite sign so that the areas would cancel if we directly added them. If we take the opposite of the remaining half and it it to this one then we get

$$A_{sum} = \frac{1}{B_{ext} + M_{eff}} \int_{-w/2}^{0} dx(B_z(x) + B_z(x)) - \int_{0}^{w/2} dx(B_z(x) + B_z(x)) \tag{3.98}$$

$$= \frac{\mu_0 I_{total} \ln(4)}{2\pi(B_{ext} + M_{eff})} \tag{3.99}$$

The area under the difference curve is much more straight forward as it is the integral of a constant.

$$A_{dif} = \frac{1}{\gamma(B_{ext} + M_{eff})} \int_{-w/2}^{w/2} dx(\tau_{Rasba}) \tag{3.100}$$

$$= \frac{w\tau_{Rasba}}{\gamma(B_{ext} + M_{eff})} \tag{3.101}$$

If we take the ratio of the areas the reason for all of this rigamarole will be clear

$$\frac{A_{dif}}{A_{sum}} = \frac{2\pi w \tau_{Rashba}}{\gamma \mu_0 I_{total} \ln(4)} \tag{3.102}$$

solving for τ_{Rashba}

$$\tau_{Rashba} = \frac{A_{dif}}{A_{sum}} \frac{\gamma \mu_0 I_{total} \ln(4)}{2\pi w \tau_{Rashba}} \tag{3.103}$$

$$\tag{3.104}$$

inserting the definition of τ_{Rasba} from Eq. 3.84

$$\frac{\hbar}{2e} \frac{\gamma \xi_{Rashba} X J_{c,total}}{M_s t_{mag}} = \frac{A_{dif}}{A_{sum}} \frac{\gamma \mu_0 J_{c,total} w t_{total} \ln(4)}{2\pi w} \tag{3.105}$$

$$\xi_{Rashba} = \frac{A_{dif}}{A_{sum}} \frac{e}{\hbar} \frac{\mu_0 M_s t_{mag} t_{total} \ln(4)}{X\pi} \tag{3.106}$$

ξ_z may also be obtain in a similar way as

$$\xi_z = \frac{A_{offset}}{A_{sum}} \frac{e}{\hbar} \frac{\mu_0 M_s t_{mag} t_{total} \ln(4)}{X\pi} \tag{3.107}$$

This was our quarry. This result is great for a few reasons. The primary one from an experimental point of view is that the result depends on a numerical integral which has

the nice effect of averaging out noise naturally. From a convenience perspective, Eq. 3.106 doesn't require us to input any transient experimental parameters such as the applied current or the external magnetic field[21] as these canceled out. This is of course not to say that such things should not be recorded and chosen with care, it is just more robust to accidental mixups with respect to experimental conditions during the analysis.

3.4 Cryo-Variations

All of the analyses of the previous sections are valid at pretty much any temperature. The difficulty in doing cryogenic experiments is largely relegated get the drive signal to the sample and then reading out the response at temperatures from 4 K - 300 K. In the case of ST-FMR and DC-Biased ST-FMR, the problem getting GHz signals down to bottom of a cryostat in a way that is robust to contraction and expansion of the cabling and connectors. Some modicum of luck is afforded to us in this endeavor, however, because we do not need optical access so we may use He vapor to cool the sample and ensure aggressive thermalization. In the case of MOKE, we do require optical access so the sample must be in vacuum and cooled by a cold finger. The case of thermal contraction of the cryostat components is particularly acute in the MOKE case as well as the device must be refocused every 10 K or so. For those interested in the minutiae of the design of such systems, I refer you to Appendix A. The following subsections are to explicitly mention the challenges associated with interpreting the results of each experiment when it is performed in a cryostat as a function of temperature.

[21] During a temperature-dependent MOKE experiment M_s and X could vary with temperature and so would semantically considered transient in this usage, but in a room temperature experiment this is normally not a concern.

3.4.1 Cryo ST-FMR

Provided you can design a system such that the mechanical and high frequency connections are largely temperature independent, the resulting signal will still be temperature dependent. The key considerations are possible changes in the distribution of current through the device, potential changes in the interface transparency of the system, and possible enhancements of the magnetic damping. Let's cover each in turn.

Current Distribution

This one doesn't really need much exposition because it is largely self-evident. The only subtlety I will call attention to explicitly is that owing to the difficulty of determining the amount of RF current that reaches the devices because of the complexity of the cabling and the possible temperature dependent impedance, one typically uses the "self-calibrated" approach to ST-FMR using the ratio of the symmetric and antisymmetric amplitudes. While this self-calibrated approach takes care of changes in current splitting for a bilayer, if one has a trilayer or above the self-calibrated approach may over or underestimate the effect of the Ørsted field. That is, the extra layers may have current flowing through them and thus effect net Ørsted field on the magnet but not contribute to the symmetric component. In this case, one must correct for this current shunting.

Damping and Interface Transparency

The temperature dependence of the damping is intimately linked to the interface transparency. In a bare magnetic layer the damping can already change as a function of temperature through various mechanisms. If the magnetic layer is coupled to another material then the magnet can shed angular momentum into that other material via "spin

pumping" resulting in an enhancement of the apparent damping. The strength of this enhancement is a function of the "spin-mixing conductance," $G^{\uparrow\downarrow}$ of the interface, the spin diffusion length of the spin Hall material, and the conductivity of the spin Hall material as well. The subtleties of this has been explored in [65]. In particular, the damping enhancement is given by

$$\Delta\alpha = \frac{\gamma G_{eff}^{\uparrow\downarrow} e^2}{2\pi M_s t_{mag}} \tag{3.108}$$

where

$$G_{eff}^{\uparrow\downarrow} = \frac{G^{\uparrow\downarrow}}{1 + 2G^{\uparrow\downarrow}\lambda_{sd,NM}/\sigma_{NM}} \tag{3.109}$$

where σ_{NM} is the conductivity of the spin Hall material, and we are in the limit that the thickness of the normal metal is much larger than spin diffusion length of the normal metal, $\lambda_{sd,NM}$. If we assume that $G^{\uparrow\downarrow}$ doesn't change appreciably with temperature, then the damping enhancement will vary with temperature through the temperature dependence of the conductivity. In particular, inspection of Eq. 3.109 reveals that the damping enhancement will get larger as temperature is decreased for a metal since σ_{NM} will go up as temperature is lowered. Intimately tied to the effective spin mixing conductance is the interface transparency, T, which is the percentage of the incident spin current makes it into the magnet

$$T = 2\frac{\lambda_{sd,NM}}{\sigma_{NM}} G_{eff}^{\uparrow\downarrow} \tag{3.110}$$

$$= 2\frac{\lambda_{sd,NM}}{\sigma_{NM}} \frac{G^{\uparrow\downarrow}}{1 + 2G^{\uparrow\downarrow}\lambda_{sd,NM}/\sigma_{NM}} \tag{3.111}$$

The net effect of the temperature dependence of the conductivity for the transparency is to cause it to decrease. Thus cooling down should lead to an enhancement of the damping and a decrease of the apparent spin Hall effect as the interface transparency decreases.

3.4.2 Cryo MOKE

MOKE suffers from the same problems Cryo-ST-FMR but in slightly different ways. One nice thing is that the current splitting correction to the Ørsted field is no longer relevant as the analysis is only sensitive to the total current through the bar. One detriment is that we can't simultaneously measure the damping because MOKE is not a resonant experiment, but the interface transparency still decreases and so does the apparent spin Hall effect.

CHAPTER 4

THE PURE RARE EARTH METALS

The research described in this chapter has been published in Physical Review B[34] in collaboration with P. Jadaun, J. Heron, C. Jermaine, J. Gibbons, R. Collette, R. A. Burhman, D. G. Schlom, and D. C. Ralph. The retelling of the story here has been edited for level and is also more verbose.

At this point we now have the background and intuition to intelligently approach an analysis of the spin Hall effect in real systems. In pure elements, the strongest spin Hall effects observed [70–72] have been found in the 5*d* transition metals, specifically Pt (with $\xi_{SH}^{Pt} = 0.06$ for Pt/Permalloy samples [5] and 0.15 for Pt/FeCoB) [65, 73], β-Ta ($\xi_{SH}^{\beta-Ta} = -0.12$) [4], and β-W ($\xi_{SH}^{\beta-W} = -0.30$) [9]. The SHE in these pure metals is believed to be largely intrinsic in nature, arising from the Berry curvature of the metal's band structure [36, 44, 74]. Work on alloys has shown that extrinsic scattering from defects can also produce a large SHE [20, 21, 37, 75–78]. For example, for Cu(Bi) [38] $\theta_{SH}^{Cu(Bi)} = -0.24$ and for Cu(Ir) [39] $\theta_{SH}^{Cu(Ir)} = 0.021$ [79].

Here we investigate the strength of the spin-Hall torque generated by a class of elements that has been relatively unexplored, the f-electron lanthanide series or "rare-earth" (RE) metals. Our work is motivated by theoretical predictions that the spin Hall effect in metals with partially full f ($l = 3$) orbitals is potentially quite large [53]. In the most naive consideration of the SHE, one might expect that the combination of both large orbital angular momenta and large spins in f-electron atoms might lead to large spin-orbit coupling terms, scaling approximately as $\langle l \cdot s \rangle$, and consistent with the qualitative trend observed in the 3d, 4d, and 5d transition metals [71, 80, 81]. Within this simple ansatz, rare-earths near 1/4 and 3/4 filling of the f orbitals are likely candidates for a strong SHE (Fig. 4.1). We caution, however, that the details of the material band structure and its as-

sociated Berry curvature can be critical, as well, so that one should not expect simply that $\xi_{SH} \propto \langle l \cdot s \rangle$.

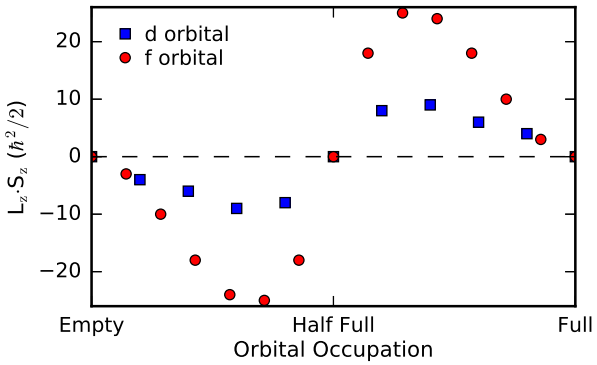

Figure 4.1: A naive estimate of the spin-orbit coupling based on Russel-Saunders or 'LS' coupling for estimates of the orbital and spin angular momentum components of the total angular momentum for Hund's rules for d and f orbital fillings.

We report both experimental measurements of spin-Hall torque ratios and theoretical calculations within density functional theory (DFT) of the spin Hall effect in four rare-earth metals: Gd, Dy, Ho, and Lu which have the f-level configurations f^7 (half-full), f^9, f^{10}, and f^{14} (full), respectively[82, 83]. These metals were chosen due to the range of orbital fillings that they cover, and because of their relative chemical stability and low vapor pressure (relative to the early lanthanides) [84]. To ensure that our measurements are robust, we report spin torque ratios derived from two separate types of measurements: (i) based on the amplitude of spin-torque ferromagnetic resonance (ST-FMR) peaks [4, 5, 33] and (ii) based on the change in the ST-FMR linewidth as a function of an applied DC current [5, 33, 85]. Our results for Gd, Dy, and Ho should be considered lower bounds on ξ_{SH} because the samples for these materials contained a thin Hf spacer layer between the rare-earth and the ferromagnet to reduce the magnetic damping enough for quantitative ST-FMR experiments. This spacer layer likely reduces the transparency factor T_{int} for spin transmission from the rare-earth to the ferromagnet.

What we find experimentally is that the spin Hall effect is small, as expected, in half-filled ($\xi_{SH}^{Gd} \approx 0.04 \pm 0.01$) and fully-filled ($\xi_{SH}^{Lu} \approx 0.014 \pm 0.002$) f-level configurations, while for the materials with partially-filled f-levels the spin torque ratio can be enhanced, $\xi_{SH}^{Dy} \approx 0.05 \pm 0.01$ and $\xi_{SH}^{Ho} \approx 0.14 \pm 0.02$. The magnitude of the value we find for Ho is among the largest for any element (comparable to Pt and Ta and smaller only than β-W [9]). The sign we measure for ξ_{SH} is positive in all four cases (the same as Pt), as expected based on Hund's rules given the orbital filling. Our results for Gd differ from a recent report by the Beach group in both sign and magnitude [86].

Our first-principles calculations suggest that the degree to which f orbitals affect the spin-Hall torque ratio depends on the proximity of the f levels to the Fermi level, ϵ_F. In Lu the f orbitals are well below ϵ_F such that the spin Hall effect is determined entirely by the contributions from the d orbitals. In Dy and Ho, however, the f levels are sufficiently close to ϵ_F as to provide an enhanced spin Hall effect. Our calculations suggest that further f-orbital enhancement of ξ_{SH} may be possible by artificially shifting the f-electron density of states closer to ϵ_F, e.g., by alloying.

4.1 Experiment

4.1.1 Materials Growth and Device Fabrication

For our Lu devices, we used molecular-beam deposition (MBD) to grow multilayer samples consisting of substrate/Fe (5 nm)/Lu (10 nm)/Al (2.5 nm) using a sapphire(0001) substrate. The entire structure was deposited without heating the substrate, *i.e.* at room temperature. The Al protective cap was then oxidized on exposure to air. Fe was chosen as the magnetic layer because of its availability in the MBD system. This stack ordering

is inverted compared to most studies of the SHE in heavy-metal/ferromagnet bilayers, because we found that it was necessary to grow the Fe layer first to produce smooth, continuous films. Attempts to to grow Lu by MBD directly on a sapphire substrate resulted in substantial islanding. For the other rare-earths, we were not able to grow any successful samples by MBD. Growth of Ho directly on sapphire yielded even worse island formation than Lu, and when we attempted to study substrate/Fe/Ho/Al samples grown by MBD the Al did not provide enough protection to keep the Ho sample from oxidizing. This could be directly observed as a progressive color change that propagated inward from the corners of the 10 mm x 10 mm chip to its center over the course of ≈15 seconds as soon as the sample was removed from the loadlock of the MBD system.

To surmount this problem, for our Gd, Dy, and Ho samples we switched to DC magnetron sputtering using a high-vacuum sputter system (base pressure $<5 \times 10^{-9}$ Torr). The rare-earth layers were sputtered from a 1" target positioned directly beneath the center of the sample plate. Depositions were conducted without heating the substrate, *i.e.* at room temperature. Sputtering of the RE metals onto a sapphire substrate at room temperature yielded smooth films with RMS roughness < 500 pm by atomic force microscopy. We were then able to grow smooth, continuous films of Permalloy (Py = $Ni_{80}Fe_{20}$) on top of the RE followed by a 2 nm Al cap. Unfortunately, when we attempted ferromagnetic resonance measurements on the Dy and Ho devices no resonance could be detected, presumably because the damping was very large. Previous studies of Py films containing RE impurities have found a similar trend in the magnitude of damping as a function of varying the RE element – RE elements for which the orbital angular momentum contribution to the RE moment is non-zero (like Dy and Ho, but not Gd) can greatly increase spin relaxation to the lattice [87, 88].

To counteract this increased damping, we grew samples with a Hf spacer layer in-

serted between the RE=Gd,Dy,Ho layer and the Py layer to minimize intermixing and reduce the magnetic damping [89]. While not necessary, the Gd samples also received this Hf spacer layer to enable us to make robust statements about any observed trend in spin Hall effect. Ultimately, for RE=Gd, Dy, and Ho the multilayer stack we used for the measurements was RE (10 nm)/Hf (t_{Hf})/Py (5 nm)/Al (2.5 nm) grown at room temperature by sputtering onto (0001) sapphire, with the Al oxidized in air. Most of our measurements were performed with t_{Hf} = 1.5 nm, although we did perform some tests with other thicknesses as described below. X-ray diffraction experiments of the sputtered samples indicate that both the RE metal and the Py film are polycrystalline with randomly oriented grains. Control samples with thicker Hf layers [both Ho (10 nm)/Hf (4 nm)/Py (5 nm)/Al (2.5 nm) and Hf (5 nm)/Py (5 nm)/Al (2.5 nm)] exhibited Hf films with notable (0001) fiber texture. Atomic force microscopy indicated smooth films with RMS roughness < 500 pm for all of these multilayer samples.

We used optical lithography and Ar ion milling to define bars 30 μm long by 8 μm wide. To finish device fabrication, we made contact pads (Ti (30 nm)/Pt (250 nm)) via optical lithography and liftoff. There was no color change observed in any of the thin film samples upon exposure to air; all remained visibly shiny and metallic throughout fabrication and processing.

4.1.2 Measurement

We performed ST-FMR measurements as described in section 3.1 using a microwave source power of 10 dBm at a fixed frequency in the range 6-12 GHz with the external magnetic field swept at 45 degrees with respect to the current flow direction. The DC mixing voltage from ST-FMR was detected through a bias tee by using lockin detection

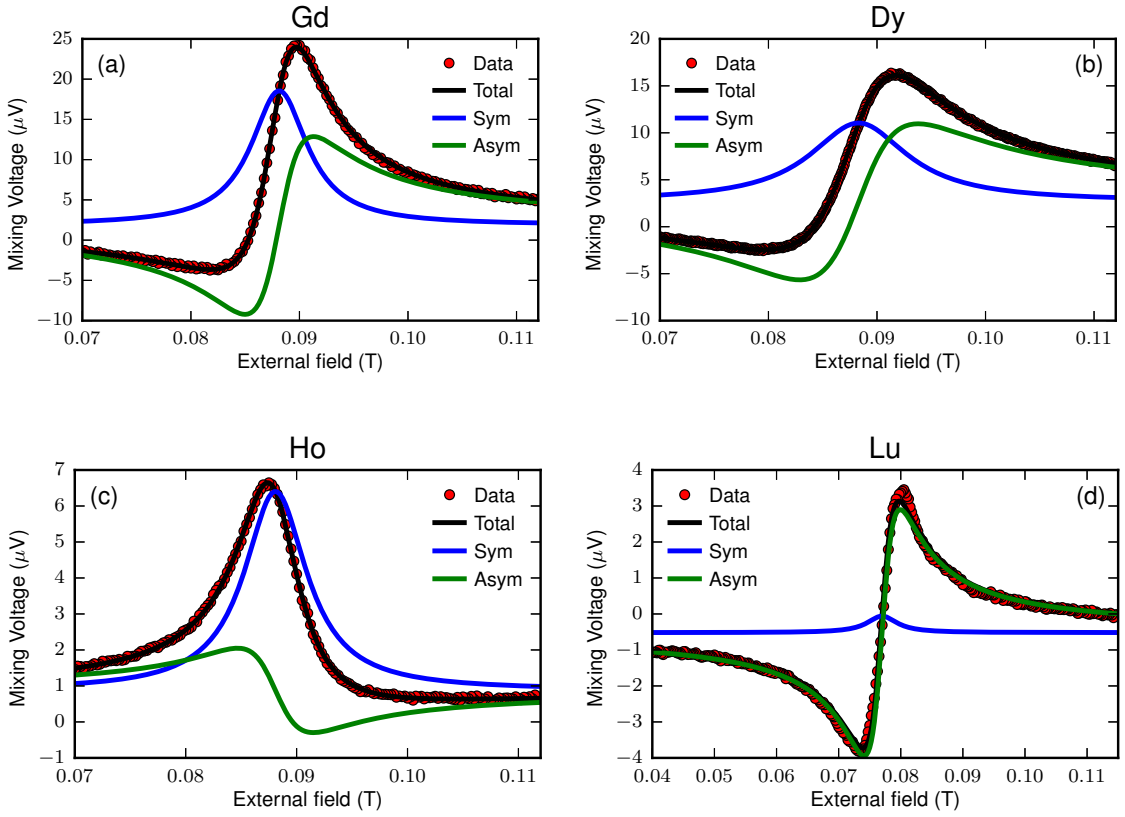

Figure 4.2: Representative ST-FMR resonance curves at 9 GHz for (a) a Gd (10) / Hf(1.5)/ Py(5)/AlO_x sample (numbers in parentheses are thicknesses in nm), (b) a Dy(10)/Hf(1.5)/ Py(5)/AlO_x sample, and (c) a Ho(10)/ Hf(1.5)/ Py(5)/AlO_x sample. (d) Representative trace for a Fe(5)/ Lu(10)/ AlO_x sample at 11 GHz. The higher frequency used for Lu is due to the larger effective magnetization of the Fe layer in the Fe/Lu as compared to the Py used for all other samples. The sign of the signals generated by the Lu sample can be compared directly to the others despite the "inverted" order of the Lu sample (ferromagnet on the bottom, which would ordinarily cause a sign change), because the sign of the anisotropic magnetoresistance in Fe is also reversed relative to the Py in the other samples. The consistent signs of the symmetric components indicate that all four rare-earth systems exhibit a positive spin Hall effect (the same sign as Pt). The sign of the antisymmetric component of the resonance is reversed in the Ho sample relative to the others.

Table 4.1: A summary of the materials parameters that enter into Eq. 3.38 for each sample. The saturation magnetization M_s is measured using vibrating sample magnetometry. (The values of M_s for Gd, Dy, and Ho correspond to Py, and the higher value for Lu corresponds to Fe.).

Element	$\mu_0 M_s$ (T)	I_{rf} (mA)	X	$\frac{dR}{d\phi}$ ($\frac{\Omega}{Rad}$)
Gd	0.88 ± 0.08	6.0 ± 0.3	0.25	3.72
Dy	0.94 ± 0.09	6.3 ± 0.3	0.27	2.93
Ho	1.1 ± 0.1	2.8 ± 0.1	0.13	3.94
Lu	2.3 ± 0.1	9.6 ± 0.2	0.07	-0.30

with amplitude modulation of the RF signal [4, 5]. The microwave power absorbed by the devices, and hence the amplitude of the microwave current in the sample, were calibrated using a vector network analyzer to measure the device S_{11} and cabling S_{21} parameters. Representative ST-FMR traces for each RE are shown in Fig. 4.2.

We determine the spin torque ratios is based on the amplitude of the ST-FMR signal: ξ_{SH} is proportional to the amplitude of the symmetric component of the resonance and $\xi_{\perp}$ is proportional to the antisymmetric part. As noted above, we calibrate the microwave current in the sample using vector network analyzer measurements, to enable a quantitative determination of the individual torque ratios. The other materials parameters required to calculate the spin torque ratios from the ST-FMR data are summarized in Table 4.1.

As a second approach to measure the spin-Hall torque efficiencies, we also performed DC-biased ST-FMR measurements as described in section 3.2 on the same devices for the Gd, Dy, and Ho multilayers. (This measurement was not successful for the Fe/Lu due to small signal levels associated with much smaller AMR signals in Fe compared to Py.) We carried out the DC-biased ST-FMR measurements using field modulation provided by a Helmholtz coil to measure the derivative of the ST-FMR mixing voltage signal. This was done to eliminate a large background offset that arises when locking into an amplitude

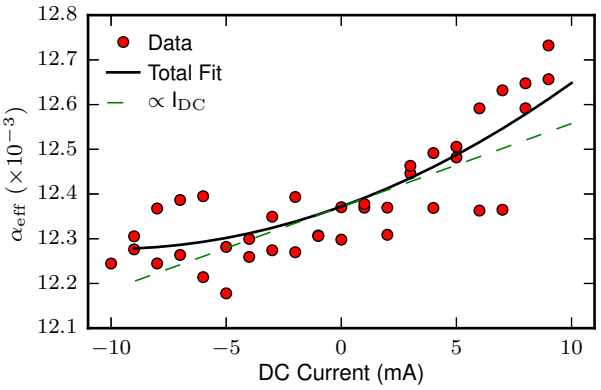

Figure 4.3: Evolution of damping of a Ho(10)/Hf(1.5)/Py(5)/AlO_x stack at 6 GHz with applied DC current. The linear component yields information about the spin Hall effect, while the quadratic background indicates heating.

modulated signal due to heating from the RF current.[1] The field modulation allowed for high sensitivity even at large (10 mA) applied currents. A representative trace for the damping as a function of current for a Ho multilayer is shown in Fig. 4.3. In addition to a linear shift of the damping as a function of DC current, we also observe a quadratic background, which is likely due to Joule heating. For determination of ξ_{SH}, we use only the linear contribution to the current dependence, determined by a least-squares fit.

4.1.3 Analysis of Experimental Results

Our results for ξ_{SH} from both the ST-FMR amplitude measurements and the DC-biased ST-FMR measurements are shown in Table 4.2 for the Gd, Dy, and Ho samples with a 1.5 nm Hf spacer layer, and for the Lu/Fe samples with no Hf spacer. These data are also plotted at the conclusion of the paper in Fig. 4.10a. We find good agreement between the two types of measurements in the samples for which both measurements could be

[1]This has the side effect that the resulting mixing voltage signal is the derivative of what is normally measured (Eq. 3.39). This does not change the analysis in any deep way, it just changes the functional form of the fits.

Table 4.2: Measured spin torque ratios for Gd(10)/ Hf(1.5)/ Py(5)/AlO_x, Dy(10)/ Hf(1.5)/ Py(5)/AlO_x, Ho(10)/ Hf(1.5)/ Py(5)/AlO_x and Fe(5)/ Lu(10)/ AlO_x. $\xi_{\perp,SO}$ refers to the spin-orbit-generated part of the field-like torque, with the contribution from the Oersted field subtracted.

Element	Hf thickness (nm)	ξ_{SH}	$\xi_{\perp,SO}$
		ST-FMR amplitude	
Gd	1.5	0.04±0.01	-0.04
Dy	1.5	0.06±0.01	-0.03
Ho	1.5	0.16±0.04	-0.07
Lu	0	0.014±0.009	-0.03
		DC-biased ST-FMR	
Gd	1.5	0.04±0.01	
Dy	1.5	0.05±0.01	
Ho	1.5	0.12±0.02	

performed. It is important to note that these results do not correspond to intrinsic values of θ_{SH} for each rare-earth due to spin current attenuation in the Hf spacer layer and also due to the likelihood of additional spin relaxation at the interfaces.

For convenience in comparing to theoretical calculations, the strengths of the spin-orbit torques can alternatively be expressed in terms of spin torque efficiencies per unit electric field (or "spin torque conductivity"), $\sigma_{SH}^{\text{exp}} = \xi_{SH}/\rho_{RE}$, where ρ_{RE} is the electrical resistivity of the rare-earth. We have included these values in Table 4.3 as well as the values of ρ_{RE}. For RE=Gd, Dy, and Ho, we determined ρ_{RE} via 4-point resistance measurements on control samples of substrate/RE/AlO_x. For RE=Lu, we used control measurements on substrate/Fe/AlO_x to extract ρ_{Lu} from the full substrate/Fe/Lu/AlO_x bilayer by treating the Fe and Lu layers as parallel resistors. These data are plotted at the conclusion of the paper in Fig. 4.10b as well. We note that given the factor $\hbar/2e$ in our definition of ξ_{SH} there is explicitly a factor of 2 in our definition of σ_{SH}^{exp} that is not used universally in the literature. Just as for our determination of ξ_{SH}, our values of σ_{SH}^{exp} will be diminished by any spin attenuation in the Hf spacer or interface spin relaxation, so these values represent a lower bound on the intrinsic spin Hall conductivity within each rare-earth.

What we find is that the spin-Hall torque ratios for Gd, Dy, and Lu are relatively small. This is to be expected for Gd and Lu because these materials have f-electron occupations f^7 (half-full) and f^{14} (full), respectively, with the consequence that the f-levels are relatively far from the Fermi level and unlikely to contribute any significant Berry curvature. The spin-Hall torque ratio for Ho (f^{10}) is significantly greater. We find for the Ho samples with the 1.5 nm Hf spacer (using the average value of the two measurement techniques) that $\xi_{SHE} = 0.14 \pm 0.03$. This is among the largest known values for any pure material, comparable to β-Ta [4] and Pt (in Pt/CoFeB samples [65, 73]), and less than only β-W [9]. This large value is despite the likelihood, as we will discuss below, of significant spin relaxation at the interfaces in the RE samples. The spin-Hall torque conductivity σ_{SH}^{exp} of Ho is, however, only slightly enhanced relative to Gd and Dy. This is a consequence of the very high resistivity of our sputtered Ho films (see Table 4.3). Due to this high resistivity, Ho is unlikely to be useful for applications despite its relatively large spin-Hall torque ratio.

The amplitude of the antisymmetric component of the ST-FMR signals gives additional information about the strength of the "effective field" component of the current-induced torque oriented perpendicular to the sample plane (see Eq. (2)). The Oersted field produced by the applied current contributes to this torque, but we also find a significant contribution from a spin-orbit torque that is oriented opposite to the Oersted field torque. In the Ho samples, the spin-orbit contribution is actually larger than the Oersted field contribution, so that the sign of the antisymmetric ST-FMR component is reversed relative to the other samples [compare Fig. 4.2c with the other panels in Fig. 4.2]. We can calculate the Oersted field based on our applied current and the measured resistivities of the sample layers, and then estimate from the amplitude of the antisymmetric ST-FMR component the out-of-plane spin torque ratio, with the results shown in Table 4.2. (The negative signs indicate that the direction is opposite to the torque from the Oersted field.)

In all cases the magnitude of $\xi_{\perp,SO}$ is at least comparable to the antidamping spin-orbit torque ratio ξ_{SH}.

For Ho, which provides the strongest spin-Hall torque from among the four elements, we fabricated a series of devices with Hf spacer thicknesses of 0.5, 1, 1.5, 2, and 4 nm, with the results for ξ_{SH} and $\xi_{\perp}^{SO}$ shown in Fig. 4.4. Previous experiments from our research group have indicated that the spin Hall effect in Hf is very weak[89], so we anticipated that both ξ_{SH} and $\xi^{\perp,SO}$ would decay to small values as a function of increasing Hf thickness, over a characteristic scale determined by the spin diffusion length in Hf, ≈ 1-1.5 nm. (We note that other research groups have reported larger in-plane spin-torque ratios from Hf, presumably due to films with different crystal structures or different impurities [90–92], but our sputter chamber has always yielded negligible spin-torque ratios for Hf films.) As a function of increasing Hf thickness we find that $\xi^{\perp,SO}$ behaves consistently with our expectation but, surprisingly, ξ_{SH} does not. Instead, ξ_{SH} decreases only slightly (by about 30%) as the HF thickness is increased from 0.5 nm to 4 nm. In contrast, control samples consisting of Hf(t_{Hf})/Py(5 nm)/AlO_x with no RE layer and with t_{Hf} = 1.5 nm and 5 nm did confirm a small value of ξ_{SH} for Hf (Fig. 4.4), consistent with previous results from our group[89].

Table 4.3: Estimated lower bounds on the spin torque conductivities (σ_{SH}^{exp}) based on this work, along with the measured electrical resistivity (ρ_{RE}) of each RE film. A literature value for Pt measured in a Pt/Py bilayer system is included for comparison. The measured value of resistivity for our Hf films is 72 $\mu\Omega$ cm, and for our Py films is 65 $\mu\Omega$ cm.

Element	t_{Hf} (nm)	σ_{SH}^{exp} ($\hbar/2e$) 1/(Ω cm)	ρ_{RE} ($\mu\Omega$ cm)
Gd	1.5	110	350
Dy	1.5	180	330
Ho	1.5	210	780
Lu	0	160	87
Pt [5]	0	3000	20

We checked using x-ray diffraction whether there was any signficant structural change for the Hf within the Ho(10 nm)/Hf(4 nm)/Py(5 nm)/AlO_x sample compared to the Hf(5 nm)/Py(5 nm)/AlO_x control, and could observe no difference. We therefore suggest that the most likely explanation of of the unexpected behavior shown in Fig. 4.4, the relatively large values of ξ_{SH} for thick Hf spacers in the Ho/Hf/Py/AlO_x samples, is that the Ho and Hf layers may not be well-separated. For example, a thin layer of Ho may migrate preferentially to the Py interface even for relatively thick Hf, or Ho impurities may exist within the Hf and contribute an extrinsic spin Hall effect. Given the weak dependence of ξ_{SH} as the Hf thickness is reduced from 1.5 nm to 0.5 nm (which should be well below the spin diffusion length), we still expect the the contribution from within the RE layer to dominate the spin Hall torque for the data in Fig. II, even if there is some additional extrinsic spin Hall contribution. Still, given this uncertainty with respect to the effect of the Hf spacer layer, we will not attempt in this initial survey to extrapolate our results to zero Hf thickness, but will simply state the measured spin-torque ratios for each of our samples. It is important to note that we are able to rule out any significant contribution to the spin-orbit torques from an interfacial effect at the Py/AlO_x or the Hf/Py interfaces given the absence of any measurable spin-orbit torque in the Hf(5 nm)/Py(5 nm)/AlO_x control sample.

The Ho samples with different Hf spacer thickness can also be used to analyze how the magnetic damping of the ferromagnetic layer is affected by the spacer. We discuss these data in an appendix.

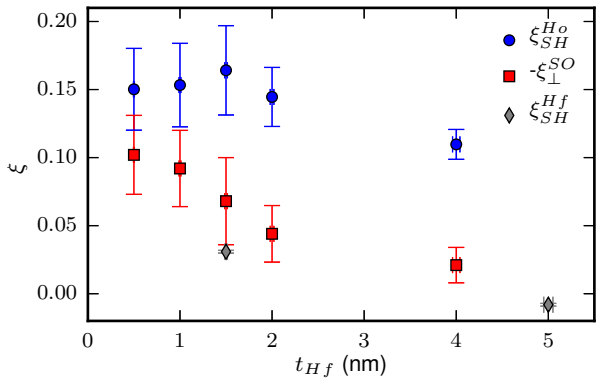

Figure 4.4: Experimental estimates of the in-plane spin Hall (blue circles) and out-of-plane effective field (red squares) torque ratios in the Ho (10 nm)/Hf (t_{Hf} nm)/Py (5 nm)/AlO_x multilayer structure using ST-FMR. For comparison, we also plot the in-plane torque ratios for measurements of a Hf (t_{Hf} nm)/Py (5 nm)/AlO_x multilayer for t_{Hf}= 1.5 nm and 5 nm.

4.2 Theory calculations from first-principles

4.2.1 Theory

Density functional theory (DFT) calculations of the spin Hall conductivity of the four rare earth metals studied we performed by P. Jadaun. We calculate on the intrinsic contribution to the spin Hall conductivity according to the Kubo formula as described in section 2.5.2. It is a non-trivial task to do DFT calculation on the rare earth metals due to the strong correlations of the $4f$ orbitals. This problem is compounded by the computational difficultly of numerically calculating the Berry curvature-like object the Kubo formula produces as its kernel near avoided crossings[2] The computational strategy for dealing with thesis challenges is described more fully in [34].

Because of the hexagonal close packed (HCP) crystal structure of the the rare-earths studied, the intrinsic spin Hall conductivity is predicted to be anisotropic. Since the sam-

[2]Recall that the denominator takes the form of the difference of energies (Eq 2.29).

ples used in experiment are polycrystalline with random orientation, we expect that the experimentally measured spin Hall conductivities are averaged over an isotropic distribution of all orientations of the crystal. To capture this theoretically, we present the average of $\sigma^z_{x,y}$, $\sigma^x_{y,z}$ and $\sigma^y_{z,x}$, which we call σ^{DFT}_s. Furthermore, we note that the quantity calculated theoretically is not identical to the spin Hall torque conductivity $\sigma^{\mathrm{exp}}_{SH}$ measured experimentally. As mentioned above, the experimentally determined value for $\sigma^{\mathrm{exp}}_{SH}$ is a lower bound as it will be reduced by any less-than ideal spin transmission through the sample interfaces and the Hf spacer layer in the real samples. The calculated spin Hall conductivity $\sigma^{\mathrm{DFT}}_{SH}$ does not include any details about transmission of spin current into a ferromagnet and represents the case of perfect spin transmission.

To robustly discern the effect of the $4f$ orbitals on the electronic structure and the resulting intrinsic spin Hall conductivity, two sets of psuedopotentials were created. One set of PsP's posits that $4f$ electrons are highly localized, and as such do not affect the electronic properties of rare-earths [93, 94]. In this case, the $4f$ states are frozen in the core of the PsP and the valence only contains the $6s$, $5d$ and $5p$ electrons. We refer to calculations using these PsP's, which were performed within the LDA, as 'f-in-core'. The second set of PsP's are constructed with the $4f$ states in the valence such that they can in principle affect the electronic properties [95]. We refer to calculations using these PsP's as 'f-in-band'. These were performed within the LDA+U. Since the appropriate values of the Hubbard U_f parameter are uncertain [96, 97], we perform such calculations for a range of U_f values.

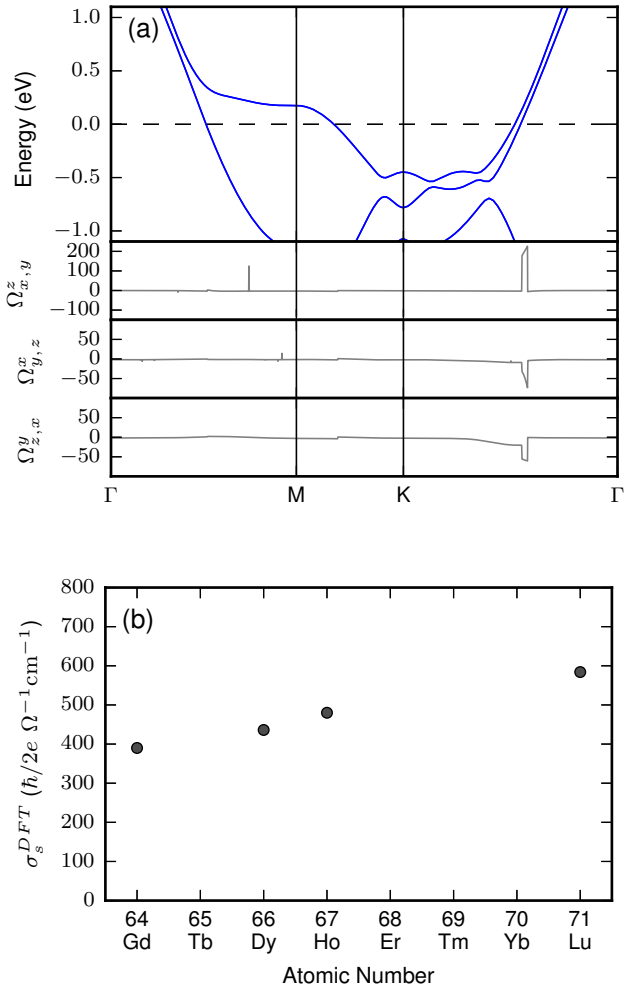

Figure 4.5: For the 'f-in-core' picture: (a) Band structure for Lu (with Fermi energy ϵ_f at 0 eV) and spin Berry curvature $\Omega^s_{\alpha,\beta}(k)$ (b) calculated spin Hall conductivities.

4.2.2 Spin Hall conductivity in the 'f-in-core' picture

Results of the spin Hall conductivity calculations within the 'f-in-core' picture for Gd, Dy, Ho, and Lu are shown in Fig. 4.5b, which shows a monotonic increase in σ_s^{DFT} with atomic number Z. This trend can be understood by first noting that all four elements have the same crystal structure (hcp) and, within the 'f-in-core' picture, have the same electron filling, i.e., $6s^2 5d^1$, resulting in a very similar electronic structure. Therefore, the monotonic increase in spin Hall conductivity from Gd to Lu is consistent with an increase

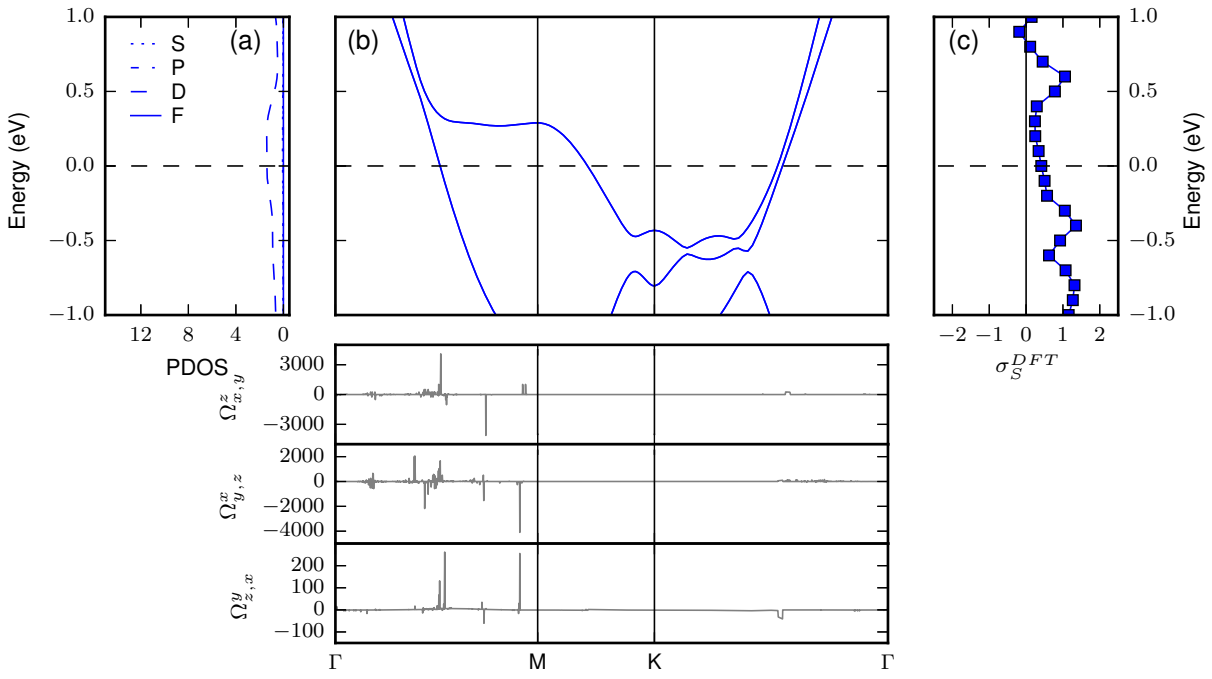

Figure 4.6: For Lu in the 'f-in-band' picture: (a) Projected density of states ('PDOS' (states/eV-atom)) (b) the band structure (top) and spin Berry curvature $\Omega^s_{\alpha,\beta}(k)$ (bottom) with U_f=5.5 eV and Fermi energy ϵ_f at 0 eV (c) calculated spin Hall conductivity (σ_S^{DFT} ($\hbar/2e$ mΩ^{-1}cm^{-1})) vs. Fermi level.

in the strength of spin-orbit coupling, a result shown previously by Ref. [98] for Pt.

To understand the origin of the spin Hall conductivity in the 'f-in-core' picture we focus on the electronic structure of Lu, shown in Fig. 4.5a, as representative. We find that there are $5d, 6s$ bands near the Fermi level ϵ_F, with avoided band crossings between the Γ and K points. These avoided crossings are the primary source of the spin Berry curvature $\Omega^s_{\alpha,\beta}(k)$, also plotted in Fig. 4.5a, which upon integration over all occupied k-states gives the spin Hall conductivity $\sigma^s_{\alpha,\beta}$. These features of the electronic structure do not vary for the different elements within the 'f-in-core' picture.

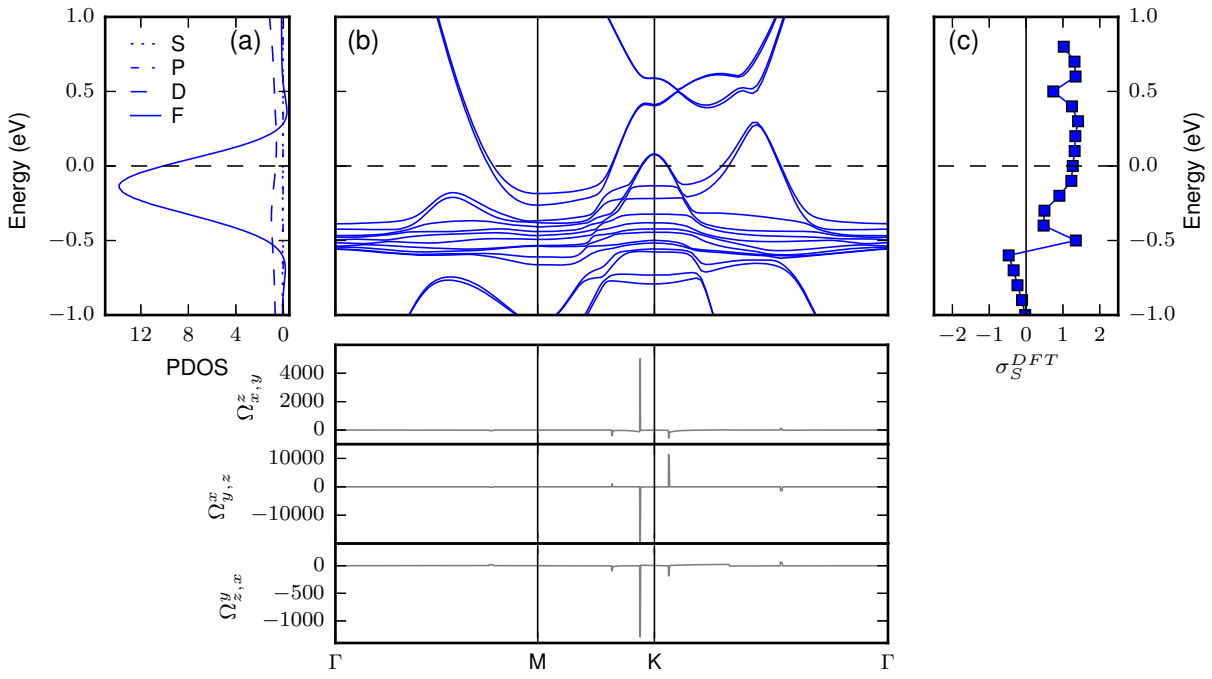

Figure 4.7: For Ho in the 'f-in-band' picture: (a) Projected density of states ('PDOS' (states/eV-atom)) (b) the band structure (top) and spin Berry curvature $\Omega^{s}_{\alpha,\beta}(k)$ (bottom) with U_f=4.9 eV and Fermi energy ϵ_f at 0 eV (c) calculated spin Hall conductivity (σ_S^{DFT} ($\hbar/2e$ mΩ^{-1}cm^{-1})) vs. Fermi level.

4.2.3 Spin Hall conductivity in the 'f-in-band' picture

For 'f-in-band' calculations, we included the $4f$ electrons in the variational density function and applied a Hubbard potential U_f to account for correlation effects. The values of the Hubbard parameter for Gd, Dy, Ho and Lu were taken to be 4.6, 5.0, 4.9, and 5.5 respectively [96]. (We discuss the consequences of assuming different values of U_f below.) To highlight the effect of $4f$ electrons on the electronic structure we will compare and contrast Lu and Ho. This is because, from among the four elements we examined, Lu with its full $4f$-shell is expected to display the least contribution of $4f$ electrons to the band at the Fermi level, while Ho is expected to display the most. Dy has a larger U_f than Ho, and Gd has a more stable f^7 shell filling, reducing the expected presence of $4f$ bands near ϵ_F as compared to Ho.

We first focus on Lu, for which the projected density of states and electronic structure are shown in Figs. 4.5a and 4.5b, respectively . The electronic structure of Lu in this 'f-in-band' picture (Fig. 4.6b) is very similar to the one obtained in the 'f-in-core' picture (Fig. 4.5a). We restrict the range of the 'f-in-band' figures to 1 eV above and below the Fermi level ϵ_F to limit the computational complexity. The complete and stable f^{14} filling of the $4f$-level in Lu and the large Hubbard term (U_f = 5.5 eV) help place the $4f$ bands deep below ϵ_F, *i.e.* $\sim$ 5 eV below. This leaves the bands near the Fermi level to originate from $5d, 6s$ electrons alone and makes them very similar to the bands obtained in the earlier 'f-in-core' calculations. As a result, the spin Hall conductivity of Lu from the 'f-in-band' calculations for U_f = 5.5 eV, 410 $(\hbar/2e)$ Ω^{-1} cm^{-1}, is similar to the result 580 $(\hbar/2e)$ Ω^{-1} cm^{-1} from the 'f-in-core' calculation. The difference between these values arises from the difference in the two pseudopotentials.

The influence of the f electrons in Ho is very different than in Lu. The projected density of states and electronic structure for Ho are shown in Figs. 4.7a and 4.7b, respectively. While we can identify the signatures of bands originating in $6s$ and $5d$ electrons, similar to those calculated in 'f-in-core' calculations, these bands are now pushed about 1.0 eV higher in energy. In addition, a host of flat bands originating from the $4f$ levels are present centered near -0.5 eV, giving rise to a large peak in the density of states (DOS) arising from $4f$-electrons ranging in energy from -0.6 to 0.3 eV, with a significant presence at the Fermi level. The largest contribution to spin Berry curvature, shown in Fig. 4.7b, comes from the avoided band crossings around the K point. The calculated spin Hall conductivity of Ho, in the 'f-in-band' framework is 1260 $(\hbar/2e)$ Ω^{-1} cm^{-1}, which is almost double the value obtained in the 'f-in-core' calculation, 640 $(\hbar/2e)$ Ω^{-1} cm^{-1}. Such a large difference between $\sigma^{DFT}_{s,f-\text{in}-\text{core}}$ and $\sigma^{DFT}_{s,f-\text{in}-\text{band}}$ cannot be explained by a difference in the pseudopotentials alone. The central result of this calculation is therefore that, within our theoretical framework, $4f$-electrons do contribute to the spin Hall conductivity of Ho in a significant

way.

Differences in σ_s^{DFT} between the 'f-in-band' and 'f-in-core' calculations can arise, in principle, not only from a direct contribution of the f-electron bands, but also from $5d$-$4f$ interactions that will modify the band structure. Since the $4f$ electrons are largely localized and the $5d, 6s$ bandstructure is altered only to a small extent by the presence of $4f$-electrons, we conclude that these interactions are small. This suggests that most of the difference in σ_s^{DFT} arises from the $4f$ electron contribution, meaning that this $4f$ contribution is large and positive for Ho. This theoretical result agrees with our intuitive discussion of the spin Hall effect from 'LS' coupling detailed earlier in Fig. 4.1 that in the late lanthanides the $4f$ bands should make a positive contribution to the total spin Hall conductivity.

Our DFT calculations for Dy and Gd also show the signatures of shifted $5d, 6s$ bandstructure features and flat $4f$ bands. In the 'f-in-band' picture, the f-DOS at the Fermi level increases in the order Gd, Dy, and Ho. Additionally, the atomic number Z and thus the spin orbit coupling constant also increases in the same order. This results in an increasing trend of spin Hall conductivity from Gd to Dy to Ho. Despite the larger atomic number Z and spin orbit coupling constant displayed by Lu as compared to Ho, the complete absence of $4f$ DOS at ϵ_f leads to a significantly smaller spin Hall conductivity for Lu compared to Ho. Altogether, the spin Hall conductivity trend predicted by the 'f-in-band' calculations is $\sigma_{s,Gd}^{DFT} < \sigma_{s,Dy}^{DFT} < \sigma_{s,Ho}^{DFT} > \sigma_{s,Lu}^{DFT}$, which is in contrast with the prediction of the 'f-in-core' framework for a monotonic increase with atomic number Z. The former agrees with the trend we observe in our experiments.

Given that there is some uncertainty in the literature about the most appropriate values to use for U_f, we also investigated how changes in U_f affect the calculated spin Hall

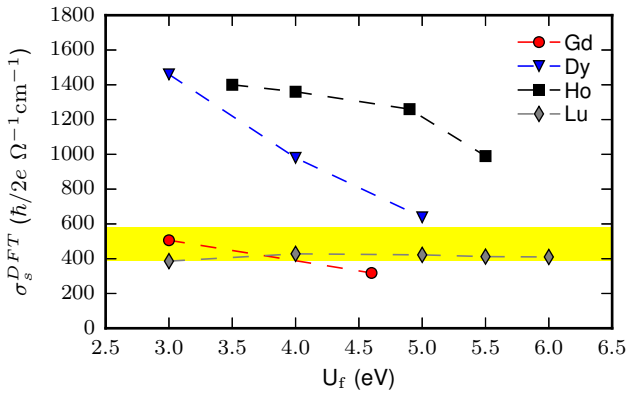

Figure 4.8: The calculated spin Hall conductivity, σ_s^{DFT}, for Dy, Ho and Lu using DFT-LDA with varying U_f ('f-in-band'). As the $4f$ states become more localized with increasing U_f, we find that the calculated σ_s^{DFT} decreases for both Dy and Ho. For Gd and Lu we find only a modest change in the calculated σ_s^{DFT}. The yellow region spans the values of σ_s^{DFT} calculated in the 'f-in-core' picture (Fig. 4.5b)

conductivity, shown in Fig. 4.8. We find that generally σ_s^{DFT} decreases with increasing U_f. In light of the above discussion, this reflects that a higher U_f will promote greater localization, pushing the $4f$ levels well below ϵ_F and lessening their participation in the conduction bands. This diminishes any enhancement to σ_s^{DFT} coming from the $4f$ levels so that in the limit of large U_f the 'f-in-band' σ_s^{DFT} reduces approximately to the 'f-in-core' σ_s^{DFT} values (the region of the yellow band in Fig. 4.8). We find that in the cases of Dy and Ho, σ_s^{DFT} depends quite sensitively upon the choice of U_f. For Dy in particular, decreasing U_f from 5 eV to 3 eV doubles the calculated spin Hall conductivity. This sensitivity to U_f, which depends on the details of electronic structure, highlights how potently the $4f$ bands can enhance σ_s^{DFT}. For our main results, we take values of Hubbard U_f for Gd, Dy, Ho and Lu to be 4.6, 5.0, 4.9, and 5.5 eV from the work of Topsakal and Wentzcovitch [96]. In contrast, van der Marel and Sawatzky [97] propose that U_f for Gd, Dy, Ho, and Lu should be 11, 5.8, 6.8, and 7 eV, respectively. We account for these differences by including estimated error bars in the plot of our final theoretical predictions for σ_s^{DFT}, discussed below and in Fig. 4.10.

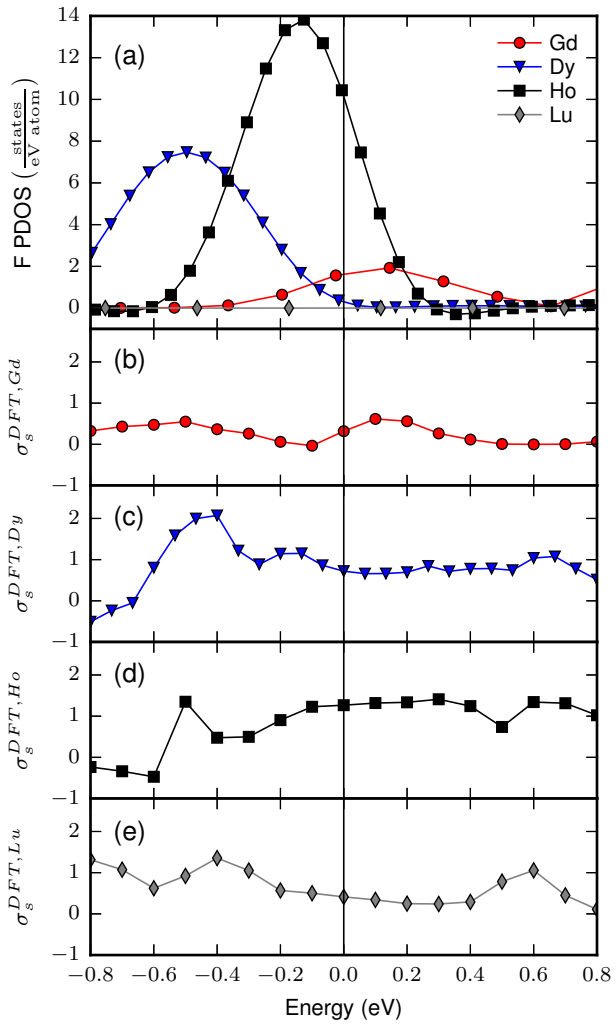

Figure 4.9: (a) Projected density of states of Gd, Dy, Ho, and Lu. (b)-(e) σ_s^{DFT} ($\hbar/2e$ mΩ^{-1} cm^{-1}) vs Fermi level ϵ_f for each element.

We can further analyze the $4f$-electron contributions to spin Hall conductivity by comparing the energy dependence of the DOS for the f electrons (f-DOS) with the variation of spin Hall conductivity as a function of Fermi level ϵ_F, as plotted in Fig. 4.9. A correlation between spin Hall conductivity and the f-DOS is evident in the plot for Dy. Around -0.5 eV, both f-DOS and spin Hall conductivity for Dy attain their maximum value with the latter reaching as high as 2070 ($\hbar/2e$) Ω^{-1} cm^{-1}. This is almost 3 times the value observed at the native Fermi level. The correlation of spin Hall conductivity with the f-DOS is less clear for Ho. This is likely due to the proximity of $4f$ to $5d$ bands and the subsequent

hybridization between them. The largest value of spin Hall conductivity for Ho in the energy range we have examined is 1350 $(\hbar/2e)\ \Omega^{-1}\ \mathrm{cm}^{-1}$, which is close to the value for the native Fermi level. For Lu, the $4f$ bands lie outside of our scanning region of 0.8 eV around the Fermi level and the variation in spin Hall conductivity in our plotting range arises from the $5d$-electrons alone. The spin Hall conductivity peak for Lu at -0.4 eV and for Dy and Ho near 0.6 eV originates from a $5d$ band feature that is shifted to different energies in the two elements because of different interactions with the f levels. In the case of Gd, there is a small but finite presence of f-DOS at the Fermi level. This coincides with the presence of the $5d$ band feature which is responsible for the spin Hall conductivity peak at -0.4 eV in Lu. Together the two contribute to the small spin Hall conductivity value predicted by our calculations. This analysis suggests that engineering the placement of the Fermi level, possibly by alloying, could enhance the spin Hall conductivity significantly if ϵ_F were tuned to place it in better proximity to either a peak in the $4f$ DOS or to an avoided crossing of the $5d, 6s$ bands. The largest value of σ_s^{DFT} we have found by tuning ϵ_F in our four elements is 2070 $(\hbar/2e)\ \Omega^{-1}\ \mathrm{cm}^{-1}$ ($\approx \frac{2}{3}$ that of Pt [5]), for Dy at $\epsilon_F = -0.5$ eV.

4.3 Comparison between Experiments and Theory

We compare in Fig. 4.10 our experimental results of spin torque ratio and spin torque per unit electric field $\sigma_{SH}^{\mathrm{exp}}$ with our theoretical predictions for spin Hall conductivity σ_s^{DFT}. For best consistency in the experimental values, we have used the results for Gd, Dy, and Ho with a 1.5 nm Hf spacer. The Lu sample had no Hf spacer.

As discussed above and shown in Fig. 4.5b, if there were no f orbital participation in the spin Hall effect, we should expect to see only a small monotonic increase in the

spin Hall conductivity from Gd to Lu owing to the increasing spin orbit coupling with Z. Instead, in the experiment we observe a quite sizable increase in measured spin Hall effect going from Gd to Dy to Ho, and then a drop to a much smaller value in Lu that cannot be captured by the 'f-in-core' picture. In contrast, the 'f-in-band' calculations are in good qualitative agreement with this tell-tale drop. The 'f-in-band' calculations can explain the strong variations in the spin Hall conductivity as due in large part to the differing magnitudes of the $4f$ density of states near the Fermi level for the different elements.

Quantitatively, the 'f-in-band' calculations predict values of σ_s^{DFT} that are significantly larger than the experimentally-measured quantities σ_{SH}^{exp}, by a factor of 3-6 depending on the element. That σ_s^{DFT} is larger than σ_{SH}^{exp} is not surprising, because the experimentally-measured torques will be reduced by less-than-ideal spin transmission through sample interfaces and by the presence of the Hf spacer in the Gd, Dy, and Ho samples. The large value of the difference suggests that spin scattering at the rare-earth interfaces may cause significant attenuation of the spin currents generated by the spin Hall effect. Another indication of a large amount of spin scattering at interfaces is the fact that the magnetic damping in the RE/Py and RE/Hf/Py samples is generally much larger than can be explained by the standard theory of spin pumping from the Py layer (see the Appendix). Improvement of the rare-earth interfaces might therefore be able to reduce this spin scattering and enable stronger spin-orbit torques.

We conclude, based on both the measurements and the 'f-in-band' calculations, that the $4f$ electrons do indeed contribute to an enhancement of the spin Hall effect in Ho, and perhaps to a lesser extent in Dy. The amount of enhancement depends on the proximity of the $4f$-electrons to the Fermi level, so that the spin Hall effect in Gd and Lu remains small. We suggest that the spin Hall conductivity might be further enhanced by tuning the Fermi level closer to either the peak in the $4f$ DOS or to a $5d$ avoided band crossing

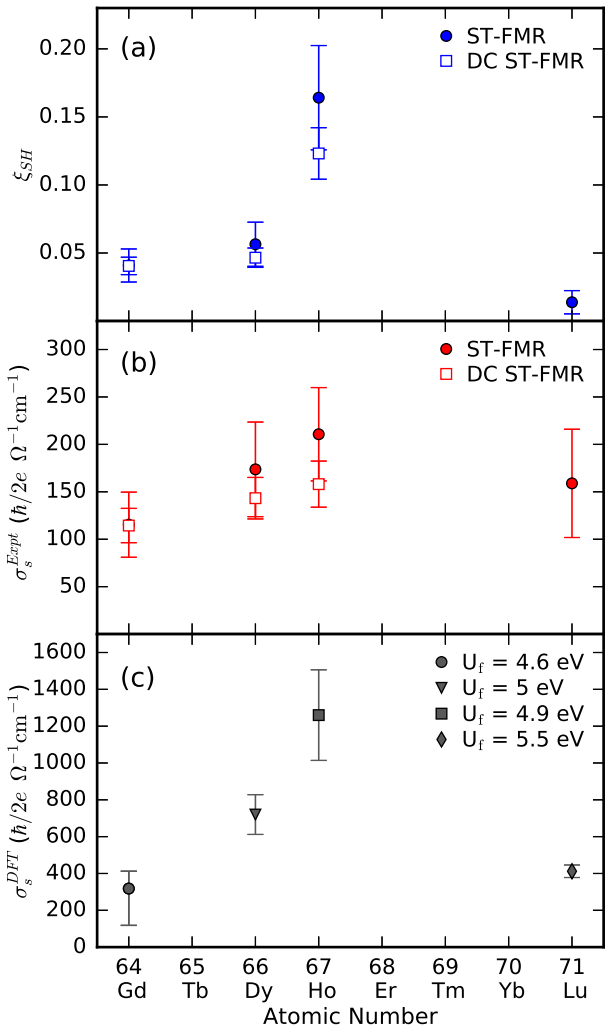

Figure 4.10: Experimentally measured (a) spin Hall torque ratio and (b) spin Hall torque conductivity of Gd, Dy, Ho, and Lu. The Gd, Dy, and Ho devices have a 1.5 nm layer of Hf between the RE metal and ferromagnet. (c) Spin Hall conductivities for the same elements calculated using DFT+U with values of U_f taken from the work of Topsakal and Wentzcovitch [96].

present in the lanthanides. Another mechanism of enhancing SHE in rare-earths could be to promote the delocalization of the $4f$ electrons.

4.4 Analysis of Magnetic Damping

As noted in the main text, the magnetic damping is increased for heterostructures in which a RE layer is placed in proximity to the ferromagnetic layer, even if there is a thin Hf spacer in between. This increase reflects the contributions to magnetic dissipation from spin pumping into the RE layer and any spin relaxation that may occur at the Hf/RE interface. For Gd, Dy, and Ho, we compared the value of the Gilbert damping (α_G) determined by ST-FMR for RE (10 nm)/Hf (1.5 nm)/Py (5 nm)/AlO_x multilayers with the value ($\alpha_G - \Delta\alpha$) for control samples without the RE layer, but still containing the Hf spacer layer. Assuming diffusive spin flow, we can define an effective spin mixing conductance for spin transport from the Py/Hf to the RE as [65]

$$g_{eff}^{'\uparrow\downarrow} = \frac{M_s t_{FM}^{eff}}{\gamma\hbar}\Delta\alpha. \tag{4.1}$$

The results are listed in Table 4.4. The values determined by this technique should be less than the true effective mixing conductance of the interface between Py and Hf because of the spin current attenuation within the Hf. In spite of this, the values for Dy and Ho (in particular) are surprisingly large. In the absence of interfacial spin relaxation mechanisms, the maximum effective spin mixing conductance should be no more than $2\rho_{RE}/\lambda_{RE}$, where ρ_{RE} is the electrical resistivity of the rare-earth material and λ_{RE} is its spin diffusion length, because this quantity determines the ability of the RE layer to absorb a spin current from the precessing ferromagnet. If we assume $\lambda_{RE} \approx 1$ nm, we find for Dy and Ho that $g_{eff}^{'\uparrow\downarrow}$ is much larger than $2\rho_{RE}/\lambda_{RE}$ (see Table 4.4). We therefore conclude that the large values of damping in the Dy and Ho samples are not dominated by conventional spin pumping from the ferromagnet into the RE layer, but rather are more likely the result of interfacial intermixing, and the ability of Dy and Ho impurities to greatly increase spin relaxation [87, 88].

Table 4.4: A summary of the damping enhancement $\Delta\alpha$, the calculated effective spin mixing conductance for each RE (10 nm)/Hf (1.5 nm)/Py (5 nm)/AlO_x heterostructure as described in the Appendix, and an estimated effective spin conductivity $2\rho_{RE}/\lambda_{RE}$ for each rare-earth. α_0 = 0.0077 as measured for a sapphire/Hf (1.5 nm)/Py (5 nm)/AlO_x control sample. λ_{RE} is assumed to be $\approx$ 1 nm.

Element	$\Delta\alpha$ (10^{-3})	$g_{eff}^{'\uparrow\downarrow}$ (nm^{-2})	$2\rho_{RE}/\lambda_{RE}\frac{e^2}{h}$ (nm^{-2})
Gd	1.2	2.9	9.6
Dy	9.3	18.6	10.6
Ho	2.4	6.2	4.4

We also measured the effective Gilbert damping coefficient as a function of Hf spacer thickness in a set of Ho (10 nm)/Hf (t_{Hf})/Py (5 nm)/AlO_X samples for t_{Hf} = 0.5, 1, 2, and 4 nm (Fig. 4.11). The results fit well to a simple exponential function plus an offset, with an effective spin diffusion length in the Hf of 0.81 nm. The offset of 0.0071 gives the limit in which the Hf is so thick that the Ho layer is not relevant to the damping enhancement. This value agrees with the damping for the control sample of sapphire/Hf (1.5 nm)/Py (5 nm)/AlO_X of α_0 = 0.0077 that was used to determine the values of $\Delta\alpha$ in Table 4.4.

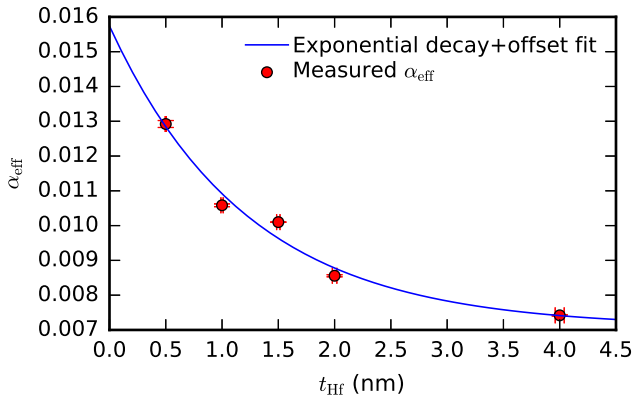

Figure 4.11: Damping of Ho (10 nm)/Hf (t_{Hf})/Py (5 nm)/AlO_x stacks for t_{Hf} = 0.5, 1, 1.5, 2, and 4 nm (red circles). Fitting to α =offset+A$e^{-t/\lambda_{sd}}$ (blue line) yields offset = 0.0071, A = 0.0087, and λ_{sd}=0.81 nm.

CHAPTER 5

YBAL$_3$: EVEN MORE 4*F* PHYSICS

In the previous section, we looked at the pure rare earth metals to understand the effect of "simple" f-orbital physics on the spin Hall effect. The key take away was that it seems that $4f$ orbital-derived states that participate in conduction enhance the spin Hall effect. In this chapter we apply this intuition to a single-crystalline thin film of the Kondo lattice system $YbAl_3$ and refine our understanding as a result.

$YbAl_3$ is a rare earth intermetallic compound with crystal structure of the prototype $CuAu_3$[99][1]. The periodic array arrangement of the Yb atoms gives rise to lattice of localized Yb $4f$ states creating what is known as a Kondo lattice. As a consequence, $YbAl_3$ exhibits a Kondo temperature of 670 K[100, 101], Fermi liquid behavior below ≈37 K[99, 102, 103], and valence fluctuations of its Yb atoms between Yb^{3+} and Yb^{2+} (f^{13} and f^{14}, respectively) with an average of 2.83 at 300 K[104, 105]. Recent success in the growth of high quality epitaxial thin films of $YbAl_3$[99] has in turn enabled high quality imaging of the $YbAl_3$ electronic structure as a function of temperature via angle-resolved photoemission spectroscopy (ARPES)[102]. This direct insight into the electronic structure reveals the enhancement of the spectral weight of the $4f$ near (<50 meV) the Fermi level according to a $\ln(T_0/T)$ dependence as temperature is decreased, consistent with a phenomenological two fluid model[106–108],[2] which may be understood as increasing hybridization of the local $4f$ moments with the conduction states with decreasing temperature. This is accompanied by a shift of the Fermi level towards the $4f$ derived states (schematically shown in Fig. 5.1) understood as transfer of electron from conduc-

[1] This amounts to an FCC structure with Al on the corners. The space group is $Pm\bar{3}m$

[2] The two 'fluids' are electrons which have not been roped into the Kondo screening of the local Yb atom moments and electrons which are involved Kondo screening. The trade off between the fluids scales logarithmically with decreasing temperature until the system is solely composed of electrons involved in screening the Yb moments (the transition to a Fermi liquid at ≈37 K).

tion band states to the Kondo screening cloud around each Yb atom. Taken together, all of this suggests a system in which the transport properties are inextricably linked to the $4f$ orbital states on the Yb atoms. In particular, this system affords us a knob we may turn (temperature) to control the presence of $4f$-derived states at the Fermi level. In light of the previous chapter and its associated work[34], this system then provides a tantalizing test bed for the hypothesis therein proposed, that to first order the mere presence of $4f$ orbital-derived states near the Fermi level enhances conduction. In the following we report on temperature dependent measurements of the spin Hall effect in thin film trilayers of $LuAl_3$/ $YbAl_3$/ Fe using ST-FMR, DC-biased ST-FMR, and MOKE to examine this hypothesis.

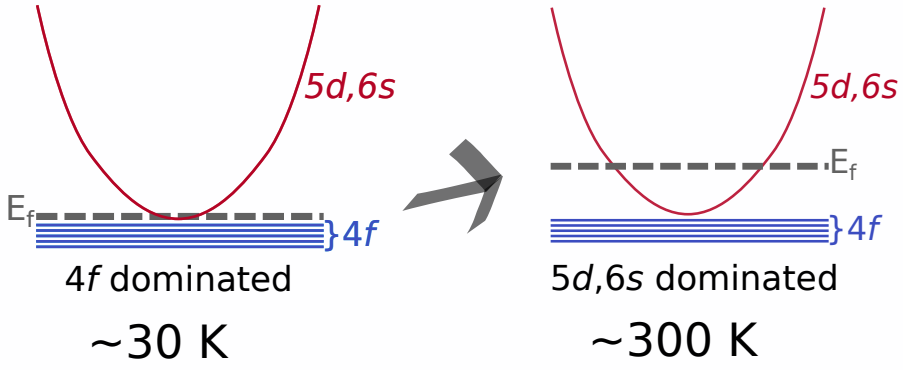

Figure 5.1: A schematic representation of the location of the Fermi level with respect to the $4f$-derived states and conduction states around the Γ point. Note that it not that the energy of the bands that are changing, but that the Fermi level is moving down with decreasing temperature.

5.1 Experimental

5.1.1 Materials Growth and Device Fabrication

Samples were grown using molecular beam epitaxy (MBE) on an MgO (001) substrate after [99]. The inclusion of a two unit cell buffer layer of Al and a 5 nm seed layer of $LuAl_3$ we found necessary to promote the growth of high quality, single crystalline $YbAl_3$ and was consistent across all samples. The $YbAl_3$ follows the orientation of the substrate such that the (100) and (010) directions line up with the substrate edges. Fe was chosen as a magnetic layer because of its availability in the MBE chamber and was deposited at room temperature followed by a 2 nm Al cap to protect the Fe from oxidation. A range of thicknesses were grown of both the $YbAl_3$ (6.73 nm, 15 nm, 18 nm) and the Fe (3 nm, 6 nm, 9 nm, 12 nm) to determine the resistivities of each individual layer as the slope of a plot of sample resistance vs 1/(thickness of the relevant layer). A control sample of MgO(001)/Al (2 u.c.)/$LuAl_3$ (5 nm)/Fe (5 nm)/Al (2 nm) was grown as well to determine the spin Hall of $LuAl_3$. Much like the Gd and Lu samples in the pure rare earth work, Yb is sufficiently close to a fully filled $4f$ shell that its presence near the ferromagnet doesn't lead to the strong damping enhancement in the ferromagnet observed for the Ho and Dy samples in the pure rare earth work, consistent with [87, 88], so no spacer layer is necessary between the Fe and $YbAl_3$.

As with the pure rare earth experiments, we used optical lithography and Ar ion milling to define micron scale bars (5-20 μm x 10-80 μm). Leads of 30 nm Ti and 250 nm of Pt were applied via optical lithography and liftoff.

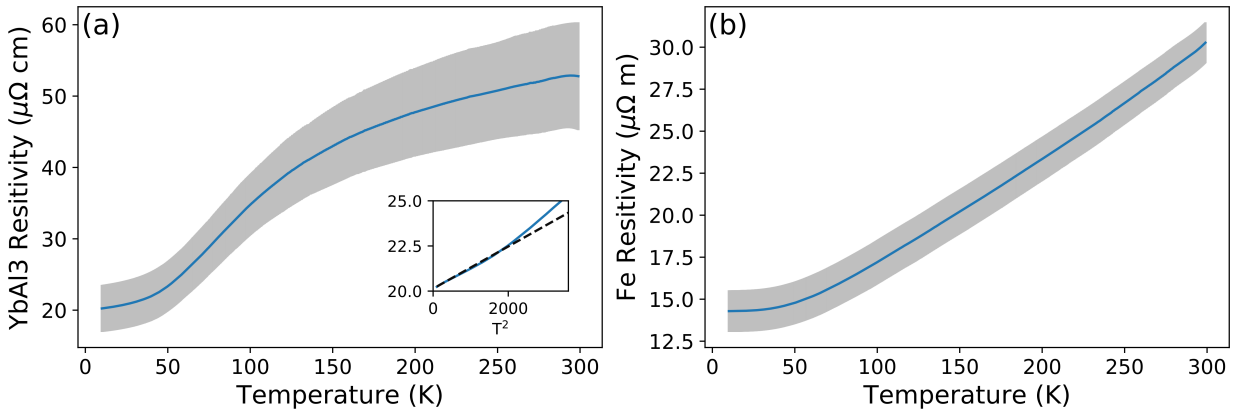

Figure 5.2: Resistivities ($\mu\Omega$ cm) vs T (K) of (a) $YbAl_3$ and (b) Fe determined from the slope of the sample resistance vs 1/thickness. The gray region represents the uncertainty derived from fitting to a line at each temperature. The inset in (a) is plot of ρ_{YbAl_3} vs T^2 from 0 K to 60 K fitted to a line (dashed line) highlighting the Fermi liquid-like behavior below T = 37 K.

5.1.2 Measurements

We determined the resistivity as a function of temperature for the $YbAl_3$ by measuring the resistance vs T for three devices on the same die for the samples MgO(001)/Al (2 u.c.)/$LuAl_3$ (5 nm)/$YbAl_3$ (6.73 nm, 15 nm, 18 nm)/Fe (6 nm)/Al (2 nm) yielding Fig. 5.2 (a). The trend and magnitude of the $YbAl_3$ resistivity vs T is quantitatively consistent with the resistivity determined for thin films without the Fe layer on top. In particular, a plot of the $YbAl_3$ resistivity vs T^2 reveals linear behavior below T=37 K consistent with the crossover to Fermi liquid-like behavior (Fig 5.2 (a) inset). The Fe resistivity was determined similarly using samples with the thicknesses MGO(001)/Al (2 u.c.)/$LuAl_3$ (5 nm)/$YbAl_3$ (10 nm)/Fe (3 nm, 6 nm, 9 nm, 12 nm)/Al (2 nm) and yields a ρ vs T shown in Fig. 5.2(b). To determine ρ vs T for $LuAl_3$ we had four options. The first two were via two control samples grown without $YbAl_3$. Assuming the Fe grew the same on the bare $LuAl_3$ film, we subtract the predicted Fe resistivity to get Figs. 5.3(a) and 5.3(b). Compared to the ρ vs T reported in [99], these results are incorrect; the $LuAl_3$ resistivity should scale similarly to Fe. This strongly indicates that the Fe likely grew differently on the $LuAl_3$

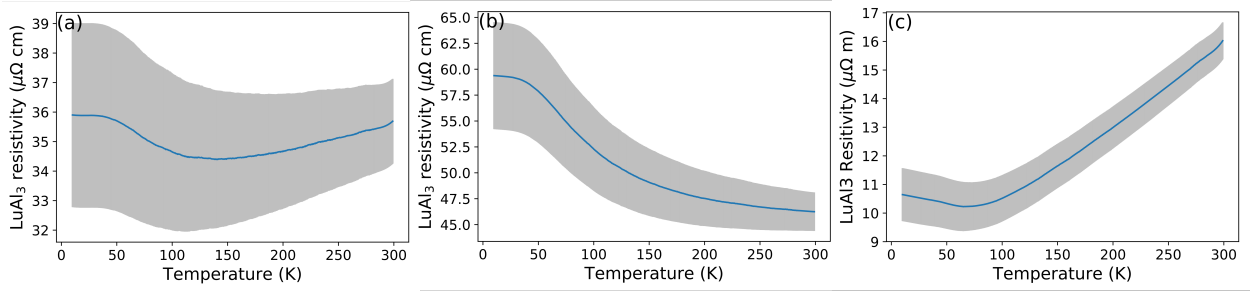

Figure 5.3: Resistivities ($\mu\Omega$ cm) vs T (K) of $LuAl_3$ determined by subtracting the nominal Fe resistance from different control samples ((a) and (b)) and from subtracting off the Fe resistance the intercept of the thickness series used to determine the $YbAl_3$ (c). The gray region represents the uncertainty derived from fitting to a line at each temperature.

than on the $YbAl_3$. The third option was to subtract the $YbAl_3$ resistance from the from the intercept of the Fe vs R 1/thickness series. However, this route yielded nonsense values for the resistivity. The last option was to subtract the Fe contribution from the $YbAl_3$ R vs 1/thickness series intercept, this yields Fig. 5.3(c) and is much more consistent with the previously reported values. For comparison, the resistivities of each layer are plotted together in Fig. 5.4. All of the above measurements were performed on a Quantum Design Physical Properties Measurement System (PPMS).

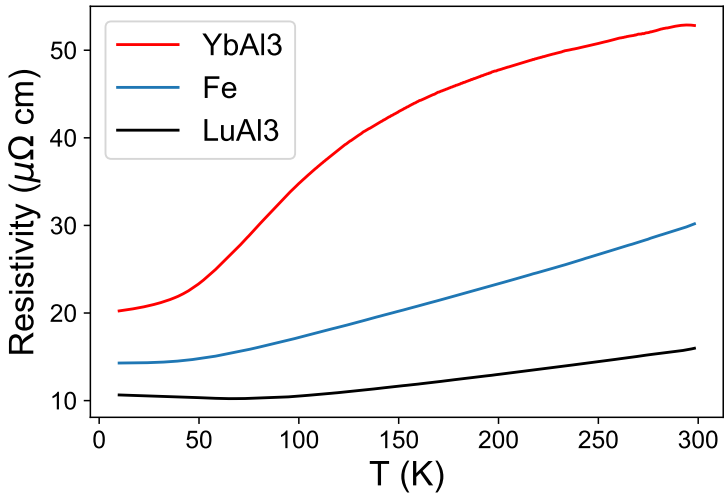

Figure 5.4: Resistivities of $YbAl_3$, Fe, and $LuAl_3$ vs T plotted together. Note that $LuAl_3$ is much more conductive than both Fe and $YbAl_3$ which will lead to non-trivial, unavoidable current shunting through the $LuAl_3$ seed layer.

To measure the spin Hall effect we perform cryogenic versions of ST-FMR and DC-bias ST-FMR using a custom built insert for a Janis He flow cryostat, and cryo-MOKE using a Janis optical He flow cryostat as described in Chapter 3. Because of the non-trivial current shunting through the $LuAl_3$ at all temperatures, we need to correct the S/A for the extra contribution to the Ørsted field that comes from the $LuAl_3$ but contributes nothing the S component. The factor by which the S/A ratio needs to be multiplied is shown in Fig. 5.5(a). Through DC-bias ST-FMR we may determine whether or not there are field-like torques acting on the ferromagnet through the deviation of the resonant field shift from what is expected from just the Ørsted field alone. To get this we also need to determine what fraction of the current flows through the $LuAl_3$ and $YbAl_3$ (Fig. 5.5(b)).

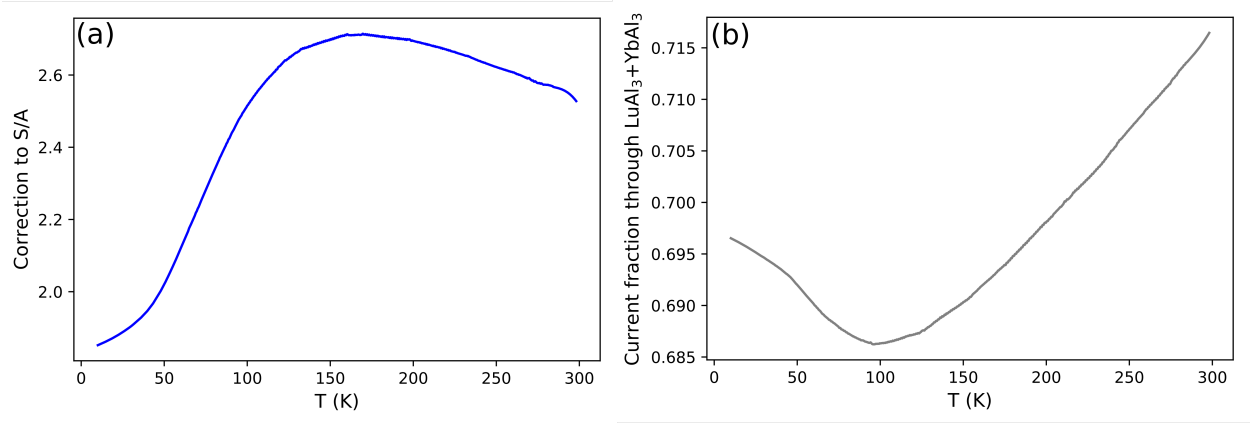

Figure 5.5: (a) Multiplicative correction to the S/A ratio owing to the current shunting through the $LuAl_3$ for a film consisting of $LuAl_3$ 5 nm/$YbAl_3$ 10 nm/Fe 5 nm/Al 2 nm. (b) Fraction of the current which flows through the $LuAl_3$ and $YbAl_3$ vs T.

5.2 Analysis of Measurements

There is a host of interesting physics that becomes evident as we cool down. To start we consider un-biased ST-FMR.

5.2.1 ST-FMR

We measured from typically 20 K to 300 K in non-uniform steps with higher sampling around the Fermi liquid transition at 37 K. We are able to maintain high signal to noise all the way down to 20 K (compare the two traces in Fig. 5.6). The evolution of the resonant field with temperature is shown for two devices on the same sample rotated 45 degrees with respect to each other in Fig. 5.7. From these traces it is evident there is non-trivial magnetocrystalline anisotropy in the Fe layer as the resonant field for a 23 GHz excitation is $\approx$ 0.18 Tesla in the first sample (Fig. 5.7(a), along a magnetic easy axis), but the resonant field for a lower frequency excitation of 19 GHz is *higher* for the device rotated 45

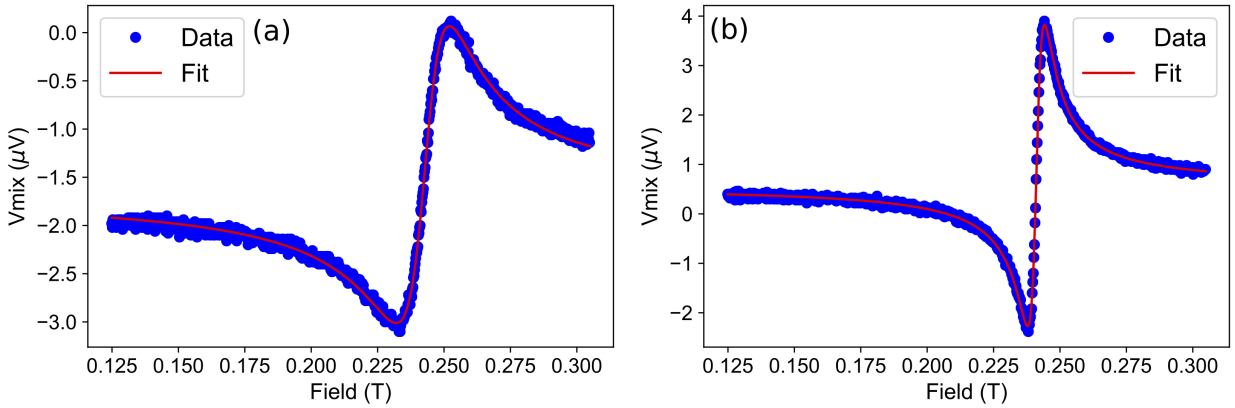

Figure 5.6: ST-FMR traces taken at (a) 20 K and (b) 300 K for a driving frequency of 22 GHz at 45 degrees with respect to the current flow direction (corresponding to (110) crystal direction). Note that the scales are not the same, the amplitude of the 20 K trace is reduced by a factor of two owing to changes in the RF transmission of the cryostat and readout of the ST-FMR voltage.

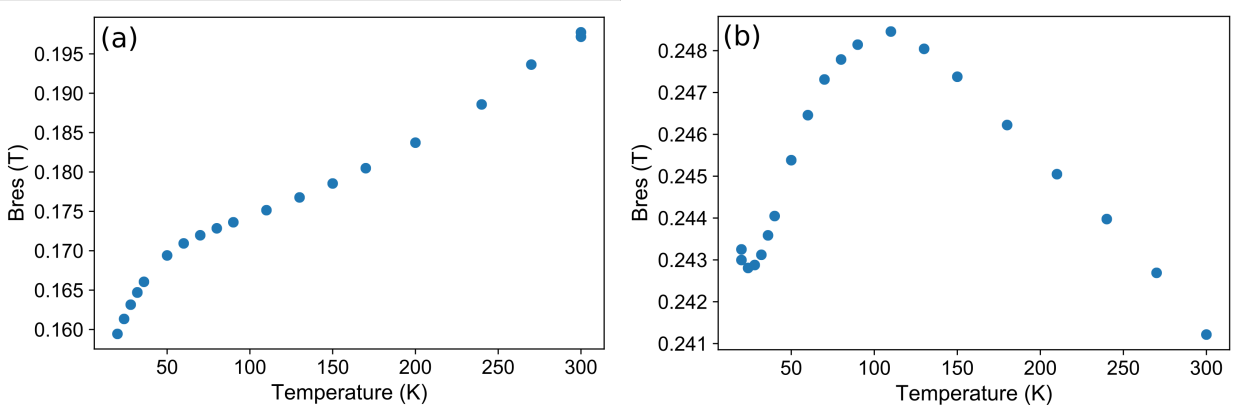

Figure 5.7: (a) Resonant field vs temperature for a device with $LuAl_3$ 5 nm / $YbAl_3$ 15 nm/ Fe 6 nm/Al 2 nm aligned along the (100) direction of the $YbAl_3$ measured with magnetic field applied along the (110) direction at 23 GHz. (b) Resonant field vs temperature for a device aligned along the (110) direction of the $YbAl_3$ measured with magnetic field applied along the (100) direction at 19 GHz. Note that the frequencies are not the same and that the measurements taken at 23 GHz have a lower resonant field than the measurements taken at 19 GHz indicating the presence of sizable magnetocrystalline anisotropy with a strong temperature dependence with easy axis along (110).

degrees with respect to the first ((Fig. 5.7(b), along a magnetic hard axis). On top of this, Fig. 5.7 also reveals a non-trivial variation in the the resonant field with temperature for each orientation. The variation of the resonant field with temperature along the hard axis (Fig. 5.7(b)) qualitatively agrees with the temperature dependence of the paramagnetic susceptibility of $YbAl_3$[109]. Because the resonant field trend tracks the trend of $YbAl_3$'s susceptibility, this suggests that the $YbAl_3$ is antiferromagnetically coupling to the magnetization creating an opposing effective field, driving the resonant field up. Comparison between the resonant field vs T along the magnetic easy axis for the $YbAl_3$ sample in Fig. 5.7(a) and a $LuAl_3$ control sample (Fig. 5.8) reveals that Fig. 5.7(a) is the sum of the effect of the $YbAl_3$ paramagnetism observed Fig. 5.7 (b) and the monotonic enhancement of the Fe magnetocrystalline anisotropy with temperature observed in $LuAl_3$ control sample (Fig. 5.8).[3]

The bandwidth of our cryostat precludes taking enough data to very tightly constrain M_{eff} and H_a by fitting to the resonant field dispersion relation (Eq. 3.23), but we may still get estimates for M_{eff} and H_a with what we are able to measure. From fitting to Eq. 3.23 at each temperature, we find an approximately temperature independent $M_{eff} \approx 1.9 - 2.2$ Tesla (Figs. 5.9(e) and 5.9(f), blue and purple traces) and an temperature dependent anisotropy field of $H_a \approx 0.08 - 0.12$ Tesla. The resonant field vs temperature of a control sample without $YbAl_3$ consisting of $LuAl_3$ 15 nm/Fe 6 nm/Al 2 nm exhibits the same qualitative behavior relating to the biaxial magnetocrystalline anisotropy (monotonic decrease with T) but without the variation additionally seen in the $YbAl_3$. This confirms that the variation with T seen in the $YbAl_3$ resonant fields is indeed a consequence of the non-trivial behavior of the paramagnetism of $YbAl_3$ with T. Of further note is that the estimate for M_{eff} is reduced to ≈ 1.6 Tesla (Figs. 5.9(e) and 5.9(f), green trace), supporting

[3]In the case of in-plane magnetocrystalline anisotropy, the resonance condition is given by the Smit-Suhl equation[110]: $\omega = \gamma\sqrt{(B_{ext} - H_{anis})(B_{ext} + \mu_0 M_{eff})}$ where H_{anis} is the anisotropy field for a given angle. This is straightforward to derive by including an in-plane anisotropy term into our the derivations done in Section. 3.1 and it is so named because Smit and Suhl derived it first.

our earlier assertion that the Fe grew differently on the $LuAl_3$ based on the resistivities of the various samples.

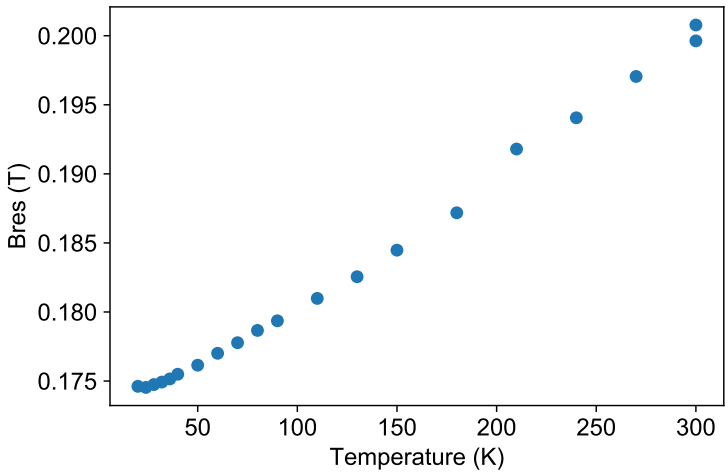

Figure 5.8: Resonant field vs temperature for a device made out of the control sample of $LuAl_3$ 15 nm/Fe 6 nm/Al 2 nm (without $YbAl_3$) aligned along the (100) direction of the $LuAl_3$ measured with magnetic field applied along the (110) direction at 21 GHz.

Examination of the linewidth as a function of temperature reveals a substantial enhancement for the $YbAl_3$ films but not for the $LuAl_3$ control film for which there is only modest enhancement and a broad peak (Figs. 5.9(c) and 5.9(d)). An old report on the damping of single crystal iron thin films notes a similar dramatic enhancement and suggest is may be due in part to inhomogenous strain broadening[111]. While we do not observe peaks for crystalline Fe in XRD, the presence of the biaxial anisotropy suggests at least some (001) texturing. Thus comparing our films and the films of [111] is not unreasonable. In both this work and [111] the enhancement could also be due to the enhancement of the spin mixing conductance as was described in Section 3.4.1 as a consequence of the temperature dependence of the conductivity in light of Eq. 3.108[65]. In our case, we have the $YbAl_3$ which is rapidly become more conductive and thus driving the spin mixing conductance up and in the case of [111] there is a 150 nm Ag film adjacent to the Fe.

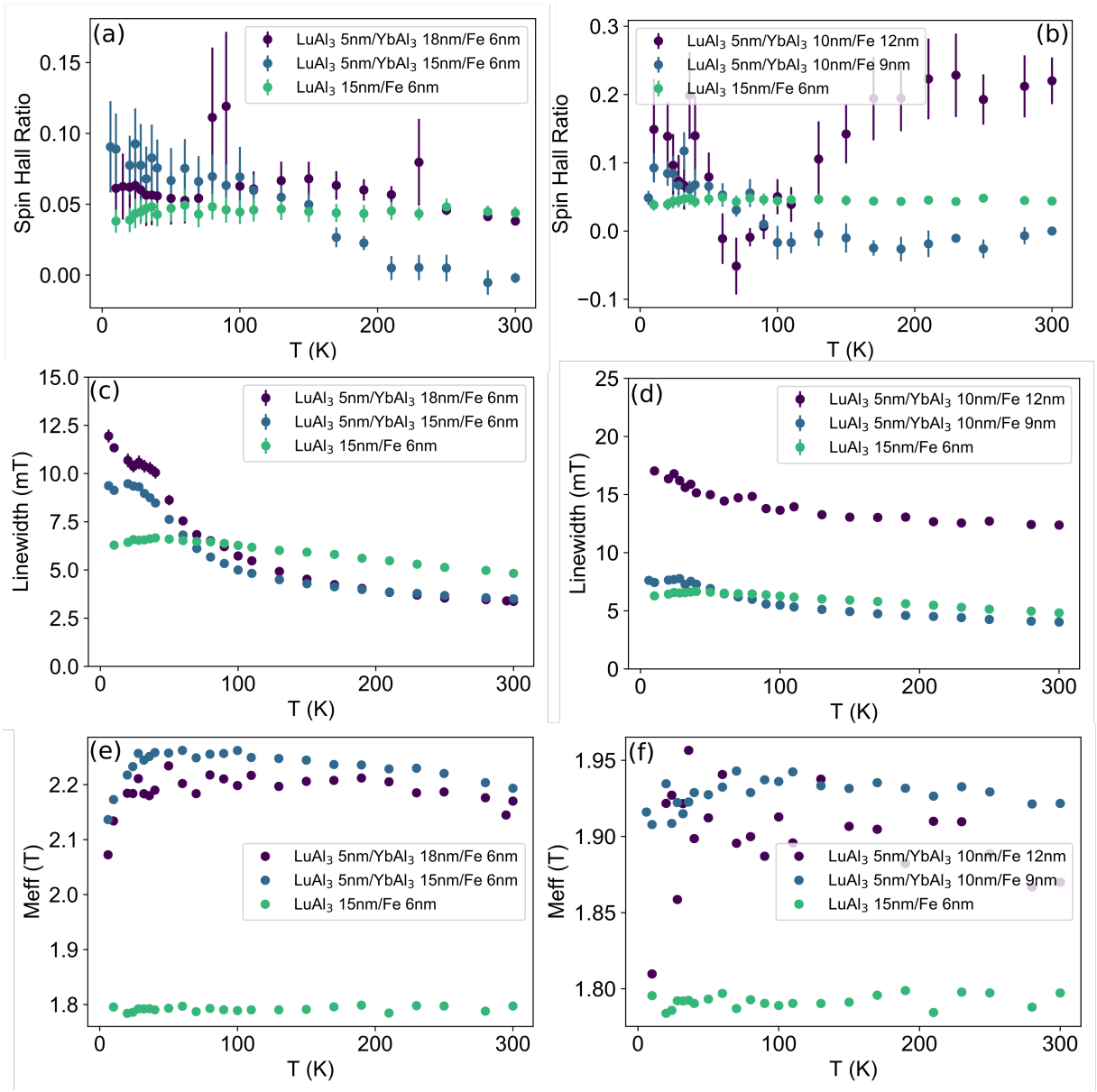

Figure 5.9: Summary of results for ST-FMR using the S/A method to estimate the spin Hall ratio. Figures (a), (c), (e) are for two early series samples plus the control sample without any $YbAl_3$. Figures (b), (d), (f) are for two late series samples plus the control sample without any $YbAl_3$. The linewidth measurements for the samples containing $YbAl_3$ are for 23 GHz and the $LuAl_3$ control at 21 GHz.

With the behavior of the sensor layer with temperature laid out, we now turn to the meat of this thesis. Figs. 5.9(a) and 5.9(b) show the spin Hall ratios derived according to the ratio of symmetric component to the antisymmetric component for traces taken at 45 degrees with respect to the current axis and corrected for the current shunted through the $LuAl_3$. We should keep in mind that an that implicit in this technique is the assumption that the only contribution to the out of plane torque is due to the Ørsted field as discussed in section 3.1.9. Fig. 5.9(a) presents data on a sample series grown on the same day (the "early series" which was used to determine $YbAl_3$ resistivity) and Fig. 5.9(b) shows films grown on the same day some two weeks after the early series (the "late series" used to determine Fe resistivity) in ostensibly the same conditions. Both figures include data from the same sample with no $YbAl_3$ (just $LulAl_3$) grown on yet a different day as a control. Both series' samples exhibit two distinct types of behavior. The first is given by the blue traces which show a monotonic increase from a spin Hall ratio of ≈ 0 to ≈ 0.1 at 20 K. The second is shown by the purple traces which exhibit a nonzero starting value followed by a modest enhancement then decrease to a minimum at ≈80 K, then further enhancement with decreasing temperature. In the case of the later series, this second type of behavior is particularly dramatic and is accompanied by a dramatic increase in the linewidth compared to all other samples (Fig. 5.9(d), purple trace), suggested that the origin of the two different behaviors may perhaps be due differences in the growth of the Fe or the $YbAl_3$/Fe interface.

The first mode of monotonic enhancement is particularly interesting as it is the most simply consistent with the hypothesis that the enhancement of the $4f$ spectral weight near the Fermi level with decreasing temperature observed via ARPES will cause an increase in the spin Hall effect as well. We cannot, however, claim that one behavior is more "correct" than the other. It could be that the differences in behaviors are due to non-Ørsted contributions to the out of plane torque, invalidating the fundamental assumption

of the S/A analysis,[4] or that there are additional in-plane torques with novel temperature dependences confounding our interpretation. To help sort out the possibilities we look towards other techniques.

5.2.2 DC-biased ST-FMR

A natural extension of the ST-FMR experiment is to apply DC-bias on top of the RF excitation as described in Section 3.2. Because DC-bias ST-FMR will allow us to independently measure the field like torques through the resonant field shift, we should be able to corroborate and if necessary correct the S/A ratio for extra contributions to the antisymmetric amplitude not due to the Ørsted field. This is in addition to the pure measurement we get of the spin Hall effect from the DC-bias dependence of the linewidth. Care is taken to ensure that the signal to noise is sufficiently high to constrain the linewidth and resonant field (Figs. 5.10(a) and 5.10(b)). Traces of ΔB vs I_{bias} and B_{res} vs I_{bias} for the "early" series of samples are shown in Figs 5.10(c) and 5.10(e), and Figs. 5.10(d) and 5.10(f), respectively. A couple things are clear at the outset. The deviation of the resonant field shift from what would be expected for just and Ørsted field is substantial and indicates the presence of additional out of plane torques that make the naive S/A calculation of the spin Hall efficiency inaccurate. In addition, the scaling of these additional out of plane torques seems to be matched by the scaling of the in-plane anti-damping torques as measured by the scaling of the linewidth enhancement with bias current.

To extract the spin Hall efficiency from the plots of $d\alpha/dI$ we multiply by the appropriate prefactors described in Eqns. 3.65 to get Fig. 5.11(b). We also correct the S/A-derived spin Hall efficiency according to the discussion at the end of section 3.2 and Eq. 3.69

[4] As was very forcefully pointed out at the end of section 3.1.7

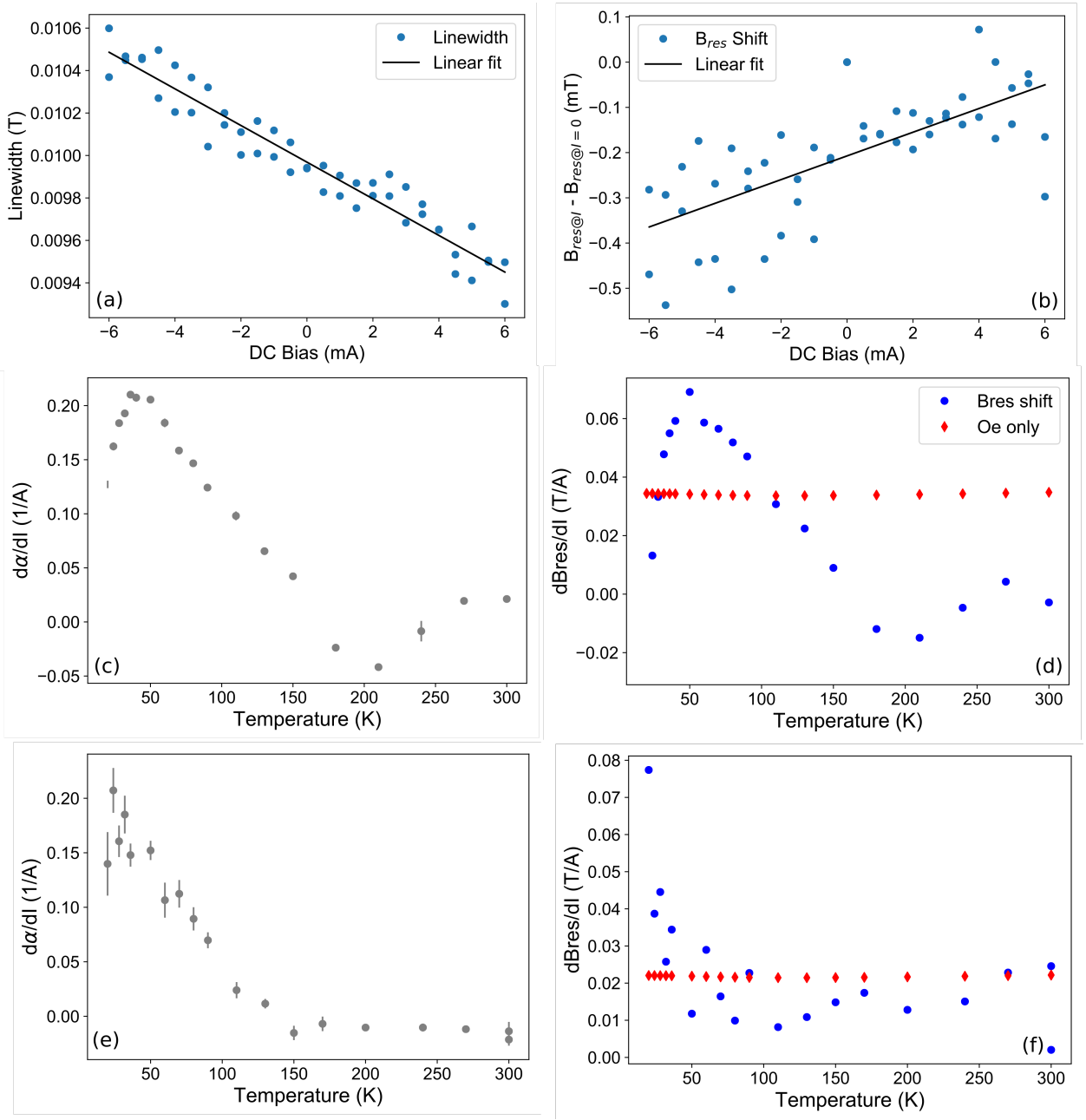

Figure 5.10: Dependence of the (a) resonance linewidth and (b) shift of B_{res} vs DC bias current at 20 K. (c,e) $d\alpha/dI_{bias}$ and (d,f) dB_{res}/dI_{bias} as a function of temperature. Traces (c) and (d) are for the sample from the early series with 15 nm of $YbAl_3$ (blue trace in Fig. 5.9(a)). Traces (e) and (f) are for the sample from the early series with 18 nm of $YbAl_3$ (purple trace in Fig. 5.9(b)). The maximum current applied of 6 mA corresponds to a max current density of $< 4{\times}10^{10}$ A/m^2 through the $YbAl_3$. The red diamonds in (d) correspond to the predicted shift of the resonance field with current in the presence of only Ørsted field.

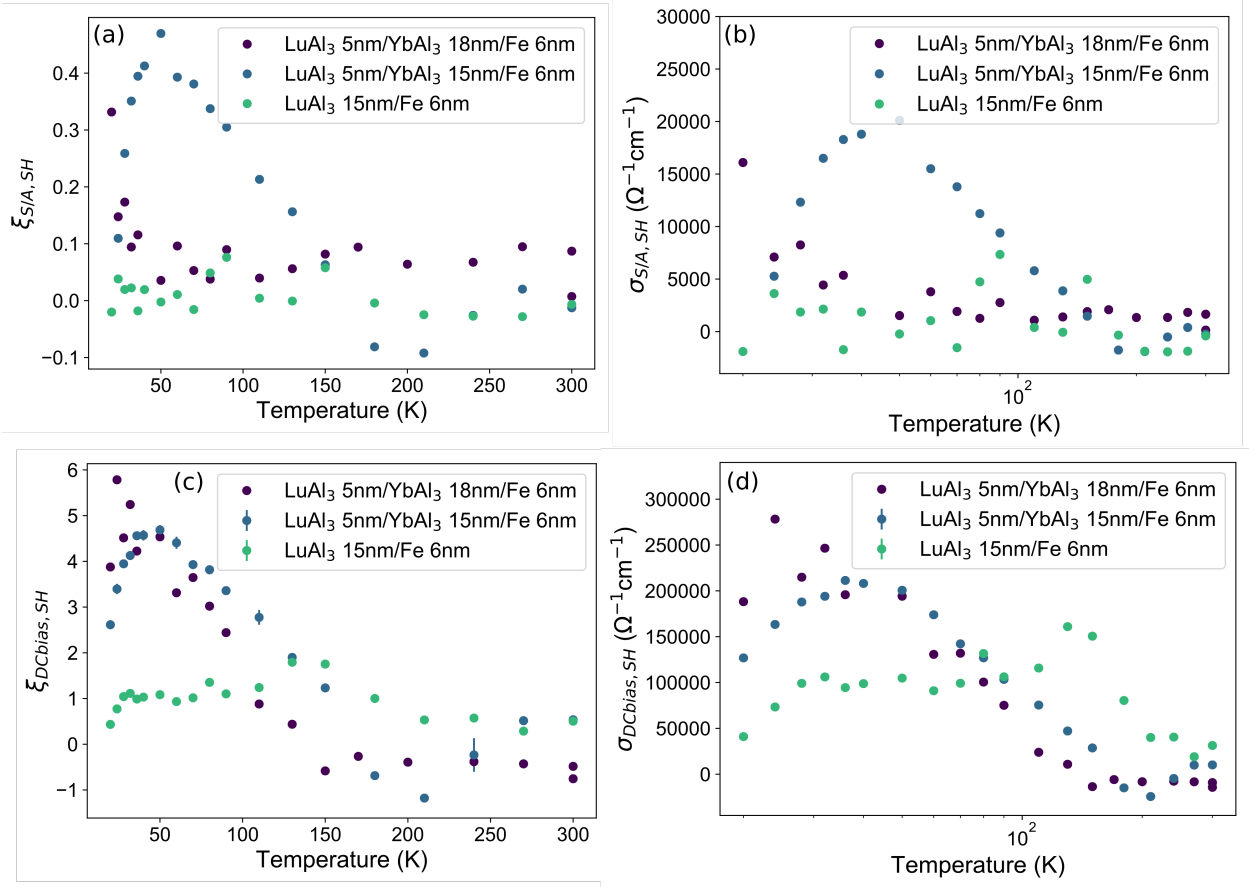

Figure 5.11: Spin Hall efficiency derived from the (a) corrected S/A and (c) the current dependence of the linewidth. The associated spin Hall conductivity is shown in (b) and (d), respectively. These samples are the same as originally shown in left column of Fig. 5.9 associated with the "early series." The color scheme is the same here as in Fig. 5.9.

to get Fig. 5.11(a). The associated spin Hall conductivity is shown in Fig. 5.11(d) and Fig. 5.11(b), respectively, on a logarithmic scale. Again, there is a wealth of information here. Most striking is the approximately logarithmic scaling behavior observable over a region of temperatures of the spin Hall conductivity. While we hypothesized that the spin Hall effect might be enhanced by the logarithmically growing hybridization of the $4f$ orbitals with conduction states with temperature, it was not *a priori* clear that we should expect a similar scaling. This strongly suggests that it is indeed the $4f$ orbital physics that is driving the enhancement of the spin Hall effect. Furthermore, this temperature scaling is completely unlike what one would expect for a naive model of the intrinsic spin

Hall effect ($\sigma_{\text{intrinsic}} \propto$ constant in our single crystalline film) nor from extrinsic channels ($\sigma_{\text{side jump}} \propto$ constant,$\sigma_{\text{skew}} \propto \rho^{-1}$). We do however, see an approximately constant scaling of the spin Hall conductivity of the only $LuAl_3$/Fe control sample which is consistent with an intrinsic spin Hall metal in the very clean metal. This is not unexpected as the $4f$ shell of $LuAl_3$ is extremely localized and is not present to give rise to any exotic physics.

This excitement about the logarithmic temperature scaling, however, must be tempered by the issues that become apparent upon close inspection of Fig. 5.11. Perhaps most glaring is the factor of 10 discrepancy between the corrected S/A results and the DC bias results. Its presence is particularly disturbing in the control sample with $LuAl_3$ as we do not expect any exotic physics to be happening because of its extremely localized $4f$ shell. This suggests that the analysis itself may be fundamentally flawed. Another possible explanation is a conspiracy of extra torques.

One of the reasons why we endured the tempest of algebra that was solving DC-bias ST-FMR for arbitrary torques was to highlight exactly this possibility. If there is an $\hat{m} \times \hat{z}$ torque present then that would show up in the S/A, but not the DC-bias results. If the Rashba-like in-plane torque acts opposite to this in-plane effective field-like torque, then we might get a coincidental cancellation. Again, however, this argument seems somewhat unlikely because a similar effect is observed in the $LuAl_3$. The author will be the first to admit he is not above mistakes, and has entertained the possibility of a lost factor of 10 in the analysis, but two other independent analyses[5] were performed on the data and a similar factor of ten discrepancy was reached. There is also the question of why the corrected S/A for the purple trace sample doesn't display the same logarithmic scaling as the blue trace, a question that persists from when we examined the uncorrected S/A spin Hall efficiency earlier. Before we resign ourselves to despair or hysteria, let us avail ourselves of the last technique I have related in this thesis as being part of the

[5]Thanks to Dan Ralph and Greg Stiehl

experimentalist's toolbox for this system: MOKE.

5.2.3 MOKE

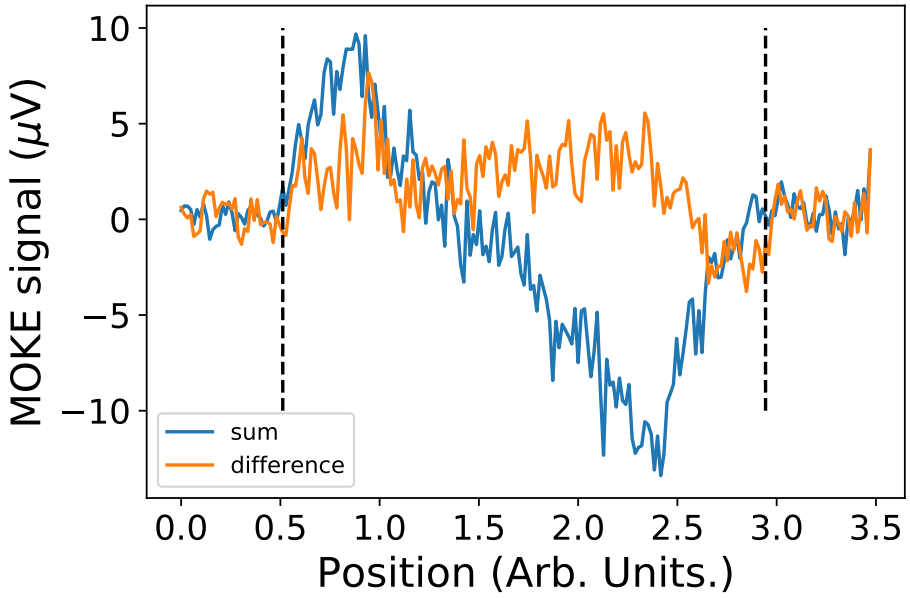

Figure 5.12: The sum and difference of MOKE scans at 20 K across a bar of the $LuAl_3$ 5 nm/$YbAl_3$ 15 nm/Fe 6 nm (blue trace in Fig. 5.11) at opposite external magnetic fields. The vertical dashed lines denote the edges of the sample. Note how the sum trace does is not centered around zero.

MOKE is a unique experiment for this sample system as it is the only non-resonant technique that has a measurable signal. The large magnetization and small magnetoresistances of Fe preclude quasi-static techniques such as second harmonic Hall measurements[112, 113]. As a reminder, the MOKE experiment uses the ratio of area analysis described in Section. 3.3 which was first suggest by Alex Mellnik[62] as a variation on [66]. A representative set of traces at opposite fields and their sum and difference are shown in Fig. 5.12. The resulting spin Hall ratio and spin Hall conductivity are shown in Fig. 5.13(a). The spin Hall ratio/conductivity are smaller than even the S/A ratio derived results, but not

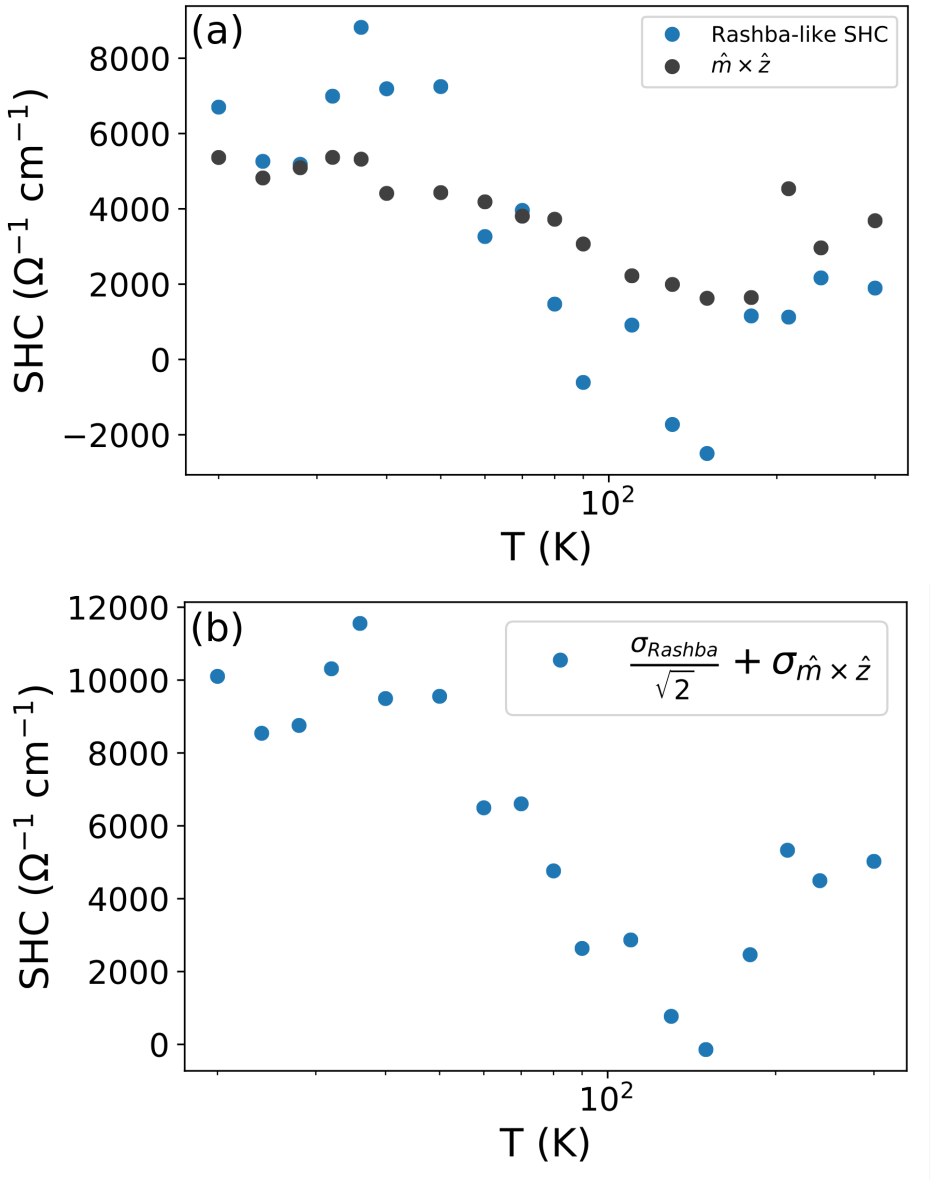

Figure 5.13: (a) Spin Hall conductivity vs temperature for the Rashba-like torque (blue) derived from the difference MOKE signal and the $\hat{m} \times \hat{z}$ (dark gray) derived form the sum offsets. (b) Combination of the spin Hall conductivities of each torque in amounts consistent with the ST-FMR experiments.

too much smaller. Perhaps most hearteningly, we gain see the same logarithmic temperature scaling. This statement is particularly robust coming from MOKE because the MOKE measurements are truly "self-calibrated." The signal due the Ørsted field has a characteristic shape and can thus be confidently identified.

As performed, the MOKE measurements were only sensitive to the spin Hall effect with Rashba-like symmetry (the "classical" spin Hall effect), and an out-of-plane effective field (which is equivalent to an in-plane torque).This is because the magnetic field was applied along the current flow direction, meaning any Dresselhaus-like torques, if present, would be zero.[6] Careful inspection of Fig. 5.12 reveals such a shift; and, in fact, such a shift is present at most temperatures. If we calculate the associated spin Hall conductivity, we get the dark gray data points in Fig. 5.13(a). Clearly this effect is non-trivial with an efficiency comparable to the Rashba-like symmetry spin Hall effect. In addition the logarithmic temperature dependence shows up again, suggesting it shares a similar origin with the classical spin Hall effect. Its presence so elegantly revealed by MOKE, was this extra in-plane torque secretly evident in the previous two techniques? Most definitely.

Because the torques act constructively this revelation brings the S/A results into agreement with the MOKE results. The S/A results were taken at 45 degrees with respect to the current flow direction thus the net torque efficiency would be

$$\xi_{tot} = \xi_{Rashba}\cos(\pi/4) + \xi_{Dresselhaus}\sin(\pi/4) + \xi_z) \tag{5.1}$$

$$= \frac{1}{\sqrt{2}}(\xi_{Rashba} + \xi_{Dresselhaus}) + \xi_z \tag{5.2}$$

If we assume that the Dresselhaus-like symmetry in-plane torque is zero then the equivalent total torque efficiency to compare with the S/A results is shown in Fig. 5.13(b). Comparing to the result obtained for the 15 nm sample in Fig. 5.11(b), we find reasonable quantitative agreement. This validates our assumption that the any Dresselhaus-like symmetry torque is negligible. This still doesn't solve the problem of the factor of 10 discrepancy with the DC-bias ST-FMR results nor does it explain why the 18 nm $YbAl_3$ spin

[6]Recall that the out-of-plane spin-orbit-induced effective field would manifest itself as a constant shift in the sum signal while the Rashba-like spin-orbit-induced torque manifests as the only origin of the difference signal.

Hall ratio vs T is different in Fig. 5.11(b), but at least we now have two techniques which agree on one sample.

Of course, if we had performed ST-FMR scans as a function external field angle at each temperature we could, theoretically, have empirically also discerned the presence and magnitude of torques with symmetry other than the Rashba-like symmetry. Two things precluded such an experiment at the outset. The first reason is a purely practical. Recall from the begin of this section that we observe an anisotropy field of ≈0.08-0.12 Tesla. In order to tightly enough constrain the ST-FMR curves there needs to be a healthy amount of field on either side of the resonance. In case where one is along an easy axis, this corresponds to a frequency choice of 22 GHz to give a resonant field of ≈0.1 Tesla. When the applied field is along a hard axis, this shoots the resonant field up to ≈0.22 T which only has 0.08 T left before it reaches the limit of the field we can apply. All of this is to say that such an experiment is difficult to perform and much more expensive in the first place, taking approximately 15x longer at each temperature; and can be difficult to interpret owing to the shift of the equilibrium angle away from the applied magnetic field angle if the field is along a hard axis.

Such difficulties should not be beyond the realm of the well-funded, competent experimentalist, but the second reason initially suggested such an angular scan experiment would not be a judicious use of tax-payer money nor the experimentalists time. That is, $YbAl_3$ has a cubic crystal structure (space group $Pm\bar{3}m$). Even the reduction of symmetry due to loss of inversion symmetry across the interface is not enough to allow torques with the symmetry other than Rashba-like even at the interface. Clearly, however, there is such a torque based on the MOKE results so it behooves us to endeavor to do an angular dependence of the ST-FMR amplitudes. The resulting symmetric and antisymmetric amplitudes at 300 K are show in Fig. 5.14. Data were taken from 20 K to 300 K. The initial

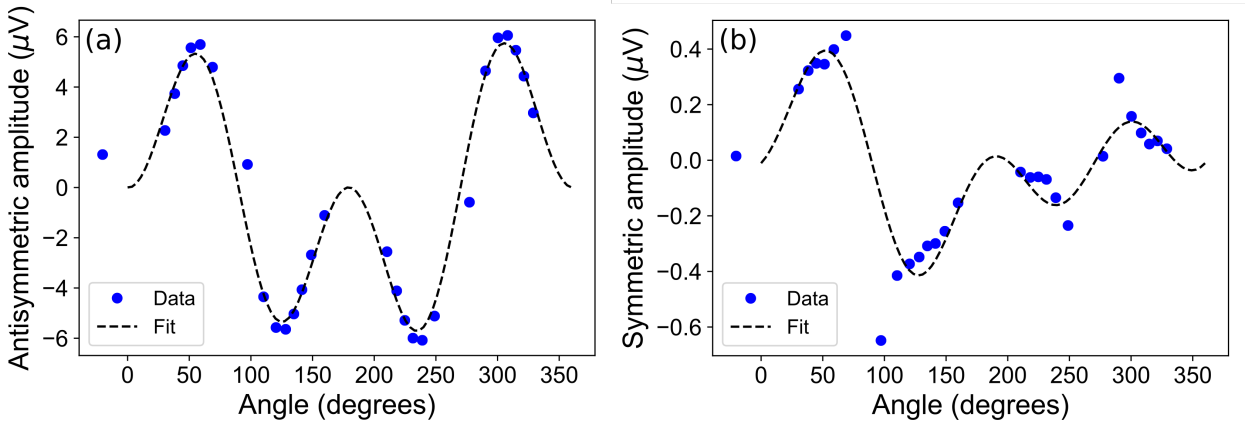

Figure 5.14: Angular dependence of the antisymmetric amplitude (a) and symmetric amplitude (b) from ST-FMR at 300 K in the $LuAl_3$ 5 nm / $YbAl_3$ 18 nm/ Fe 6 nm sample. The dashed black line is a fit that includes terms for and torque with Z symmetry and Rashba-like symmetry.

choice of nominal field angles with respect to the current flow direction combined with the biaxial anisotropy resulted in a clustering of the actual equilibrium angle of the magnetization, as is visible in Fig.. 5.14. This clustering makes quantitative analysis difficult as the sparseness of points in some areas lead to poorly constrained fits. Visual inspection of the symmetric amplitude vs angle, however, reveals a clear deviation from the $\cos^2\phi \sin\phi$ symmetry expected for just a Rashba-like torque from 300 K down to 20 K, corroborating the existence of the extra in-plane torque with Z symmetry we identified in MOKE.

5.3 Pt/Pt control

While this consistency is heartening, this result still doesn't solve the two outstanding mysteries of why a nominally symmetry forbidden torque is present and why there is such dramatic disagreement between the DC bias result and the ST-FMR/MOKE results for the absolute magnitude of the spin Hall effect. To help understand the latter mys-

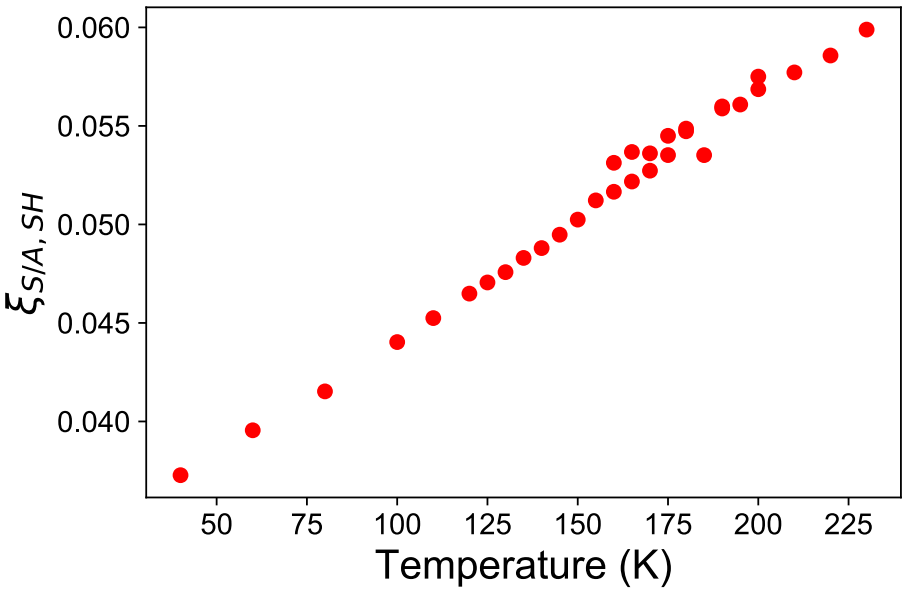

Figure 5.15: Spin Hall efficiency of Pt 8 nm/Py 6 nm/Al 3 nm vs T determined via S/A analysis of ST-FMR

tery, we performed a control DC-bias ST-FMR experiment using the well studied system Pt/Py. As far as the author can discern at the time of writing, there have been no reports of measurements of the spin Hall effect measured via DC-bias STMFR at temperatures below room temperature. Measurements at below room temperature using non-local spin valves[22] reveal a monotonic decrease in the spin Hall ratio which scales with the Pt resistivity, consistent with Pt being an intrinsic spin Hall effect dominated material. Second harmonic measurements[65] report a similar scaling of the in-plane torque for Pt/Co and Pt/CoFe devices. Indeed, in the S/A ratio determination of the spin Hall effect as function of temperature we find similar behavior and excellent agreement with values acquired in other systems at room temperature (Fig. 5.15). Performing DC bias measurements and analysis identically to the $YbAl_3$ analysis yields Fig. 5.16. These results are somewhat surprising given how the S/A scaling in Pt/Py shows the expected behavior. The presence of additional out of plane torques as evidence by Fig. 5.16(a) is not entirely without precedent, Ref. [65] observes it in their low frequency measurements using out of plane

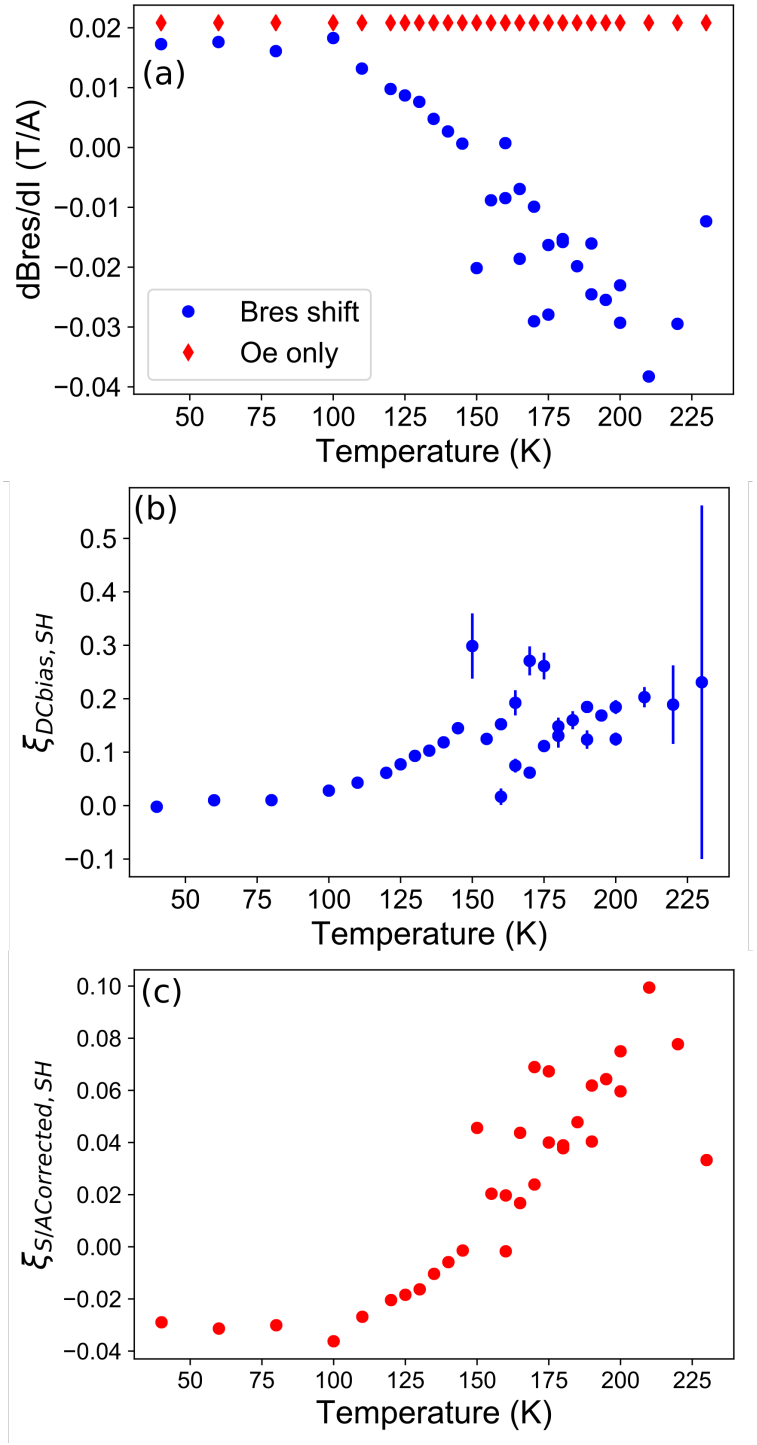

Figure 5.16: (a) Shift of the resonance field vs T compared to predicted shift (red diamonds) from Ørsted field. Spin Hall efficiency of Pt derived from (b) current dependence of the linewidth and (c) corrected Fig. 5.15 according to the apparent extra torques in the resonant field shift.

ferromagnetic layers. Suspiciously, the presence of strongly temperature-dependent non-Ørsted out of plane torques manifests in their Pt/CoFe devices but not their Co devices. This weakly suggests that it may be the Fe (recall that Py is $Ni_{80}Fe_{20}$) that is giving rise to the weird scaling with temperature.

What is happening with regards to the linewidth enhancement? It's hard to say. It might be helpful suggestively comment on what we measure and what our equations of motion predict. What we measure is the enhancement of the damping of a ferromagnet driven to ferromagnetic resonance due to a static DC-bias. Our equations of motion assume that the only damping enhancement is due to the static spin transfer torque that impinges on the magnet as a result of the DC-bias. This does not include other possible current-dependent damping enhancement mechanisms. Microscopically, we also have a spin accumulation at the interface which gives rise to a local magnetic moment. One could perhaps imagine that this local spin accumulation is enhanced by the paramagnetism of (or proximity induced magnetism in) the Pt to introduce a new avenue for magnetic damping enhancement. This could still potentially be linear-in-current as the size of the DC spin accumulation is proportional to current. It is tantalizing to think that it is a statement about paramagnetism as Pt undergoes a transition from local to itinerant paramagnetism with a crossover at around where the signal diverges[114]. The variations in $YbAl_3$'s paramagnetism[109] also trace out the dramatic changes in the current dependence of the linewidth and resonant field. Further investigation is ongoing.

5.4 Conclusion and Future Work

So where do things stand? We have reasonable agreement in magnitude for the spin Hall efficiency for two out of three techniques (corrected S/A and MOKE). While the spin Hall

efficiency derived from this is not the largest, it is respectable and comparable to efficiency β-W, $\xi_{SH}^{\beta-W} = -0.30$ [9]. However, $YbAl_3$ is a much better metal than β-W (by a factor of $\approx$10 at 37 K) so that the spin Hall conductivity of $YbAl_3$ is one of the largest yet reported in a metallic system. All three techniques display a logarithmic temperature scaling that is strongly suggests that the driving physics is in fact the enhancement of the $4f$ orbital hybridization at the Fermi level observed by ARPES. This is consistent with our original hypothesis that $4f$ orbital participation in conduction will lead to an enhanced spin Hall effect, but it does not mean that there isn't more complex physics hiding underneath.

In order to disentangle things, we are going to grow a new series of films with a different magnet (Py) which will alleviate some of the experimental difficulties. Furthermore, we are going to experiment with including a spacer layer to determine if the effect is perhaps due proximity magnetism in the $YbAl_3$ or other interface effects. DFT calculations similar to those performed in the previous chapter would also be illuminating. However, the strong correlations and Kondo physics are challenging for DFT, and current packages do not adequately reproduce the bandstructure observed via ARPES. In fact, it is the author's hope that this work will help serve as a test for new electronic structure calculations to reproduce the observed spin Hall temperature scaling.

APPENDIX A

EXPERIMENTAL DESIGN

Ho there traveler, you have come a long way if you have found yourself in this appendix. I hope you find some comfort around the literal fires of my tribulations and leave more prepared to successfully transmit high frequencies signals to your devices in the presence of a magnetic field at reasonably cold temperatures.

A.1 Probe stations

Cornell is possessed of three "Projected Field Stations." One is owned by CCMR, one is own by the Burhman group, and one is owned by the Ralph group. These stations rely on two electromagnets with upward facing poles to project the magnetic field above the poles. By carefully measuring the magnetic field as a function of the location of the electromagnet under a sample, a magnetic field with arbitrary direction and strength (up to 0.28 T in-plane and 0.2 T out of plane) may be applied to a given sample. Electrical contact can be made to the samples with DC probes and RF probes suitable up to 40 GHz. This versatility of both the frequency of electrical connections that can be made and arbitrary direction of the magnetic field means that this station is capability of almost any experiment used to determine the spin Hall effect.

Of course, the devil is in the details. The magnetic field magnitude and direction can vary dramatically over even a mm (especially out of plane). This point is particularly relevant for the calibration where one typically embeds a 3-axis hall probe in the sample plate which sits just above the surface of the electromagnet. The magnetic sensitive volume lies one mm below the surface of the Hall probe which means that to ensure proper calibration, one should displace the sample plate up 1 mm to account for this. If one really

wants to be precise, that displacement also might include the thickness of the substrate upon which their sample is grown. I belabor this point because this in some sense precludes close loop control of the field without having a correction matrix to account for the field measured by the Hall vs the field at the sample.[1]

The specifics of calibration aside, there is a still a problem of control theory. I subscribed to the one that Graham suggested where one finds the position of the magnet where the field is purely in-plane for all in-plane rotation angles and then calibrates the field vs current for the purely in-plane field. To get the calibration for the out of plane angles, one then moves the magnet along the axis parallel to the in-plane field at max field and records the angle and magnitude of the field at every position. This reveals what position from centered gives a requested out of plane angle and also how much the field decreases, allowing one to correct the base field vs current calibration. To include an in-plane rotation one then just applies a rotation matrix.

In addition to this, the probe arms themselves provide some level of consternation as well. We are in the business of making electrical contact to sample with probes mounted at the end of probe arms themselves mounted to micropositioners then sweeping a magnetic field. This can cause trouble as the the fanciest probe arms with planarization[2] manipulators near the end have magnetic washers. While the magnetic field does fall away quickly from the sample location, the magnetic elements are far away from the the base of the probe arm leading to a nontrivial torque which can cause the probe tips to drift on the sample during a scan. This can cause all sorts of problems especially if the probe tips drift off of the sample pads. One solution was to make our own probe arm out of aluminum which lacks planarization manipulators but is completely non magnetic. Great

[1] I think this is one of the reasons that the Buhrman group station, which uses closed loop control without correction, yields in-plane resonances at higher fields than other systems such as Colin's FMR set up.

[2] Rotating the probe mount at the end of the arm to ensure that the all of the tips of a multi-armed probed engage the sample at the same time. *i.e.* assuring that the plane of the probe tips is parallel to the plane of the sample.

care was taken to ensure that all of the axes were right to one another while machining, and planarization has not been a problem thus far.

A.2 Kavli Rotatable C-Frame Magnet

An inspired purchase by a Kavli foundation postdoc[3] at Cornell let to the acquisition of a GMW C-frame electromagnet with flat faced poles for maximum field homogeneity. The truly inspired aspect of this purchase was that the magnet came mounted to a continuously rotatable base. Granted, there was no automation associated with rotation capability, but as a starting point this allows for more physics than a stationary C-frame would easily admit. However, this being 2018 and all, the author could not countenance manual rotation of the magnet for eminently practical reasons. The precision of manual rotation is limited to at best a degree away from the 10^0 marks on the rotation stage itself. High dimensional scans[4] including magnetic field angle would prove prohibitively time consuming if a graduate student had to manual rotate the magnet every twenty minutes. These considerations in mind, the author endeavored to make what amounts to a one-axis 3D printer using a stepper motor and two optical limit switches move the magnet up to 288 degrees. Closed looped feedback is provided by a quadrature rotatory encoder coupled to the rotary base to accurately determine the true angle rotated with arcminute precision. Coupling of stepper motor to the magnet is achieved using a tooth belt rigid attached at on point on the magnet's circular base. Control is achieved using an arduino pro mini microcontroller and stepper motor driver board. The firmware was designed so that hitting the limits disables all motion past the limits. Communication is via USB and consists of 'GOTO [ANGLE]', 'LOC?', and 'HOME'. The serial port settings are 9600

[3] Marcos Guimarães

[4] That is, sweeping multiple independent variables

BAUD, 8 bits, no parity, no flow control.

A.3 Photolithography Recipes

For device definition I have had great success with Shipley S1805 photoresist spun for 60 seconds at 3000 RPM with an acceleration of 3000 RPM/s and then baked for 60 seconds and 115 degrees C. This leads to an optimal exposure time of 0.21 seconds on the 5x g-line stepper (my minimum feature size is 5 μm). For liftoff, I have abandoned the use of LOR because S1813 has proved suitable by itself and none of my device leads are particularly fine. The spin and bake profile is the same. The optimal exposure time is $\approx$0.40 seconds.

For resist stripping after ion milling I find an overnight soak in 1165 (N-methylpyrolidinone) and then 10 minutes of sonication suitable. For liftoff, I find the highest success if a high pressure stream of acetone from a squirt bottle is first used to remove as much lifted off material as possible and then to clean up the remaining small pieces (if necessary) with a minute or two of sonication.

BIBLIOGRAPHY

[1] M. H. Kryder and C. S. Kim, "After hard drives-what comes next?," *IEEE Trans. Magn.*, vol. 45, no. 10, pp. 3406–3413, 2009.

[2] J. S. Meena, S. M. Sze, U. Chand, and T.-Y. Tseng, "Overview of emerging non-volatile memory technologies," *Nanoscale Res. Lett.*, vol. 9, no. 1, p. 526, 2014.

[3] S. V. Aradhya, R. A. Buhrman, D. C. Ralph, and G. E. Rowlands, "Nanosecond-timescale low-error switching of 3-terminal magnetic tunnel junction circuits through dynamic in-plane-field assisted spin-hall effect," Feb. 1 2018. US Patent App. 15/462,760.

[4] L. Liu, C.-F. Pai, Y. Li, H. W. Tseng, D. C. Ralph, and R. A. Buhrman, "Spin-torque switching with the giant spin Hall effect of tantalum," *Science*, vol. 336, no. 6081, pp. 555–558, 2012.

[5] L. Liu, T. Moriyama, D. C. Ralph, and R. A. Buhrman, "Spin-torque ferromagnetic resonance induced by the spin Hall effect," *Phys. Rev. Lett.*, vol. 106, p. 036601, Jan 2011.

[6] S. Emori, U. Bauer, S.-M. Ahn, E. Martinez, and G. S. D. Beach, "Current-driven dynamics of chiral ferromagnetic domain walls," *Nat. Mater.*, vol. 12, pp. 611–616, 07 2013.

[7] K.-S. Ryu, L. Thomas, S.-H. Yang, and S. Parkin, "Chiral spin torque at magnetic domain walls," *Nat. Nano.*, vol. 8, pp. 527–533, 07 2013.

[8] I. M. Miron, G. Gaudin, S. Auffret, B. Rodmacq, A. Schuhl, S. Pizzini, J. Vogel, and P. Gambardella, "Current-driven spin torque induced by the rashba effect in a ferromagnetic metal layer," *Nat. Mater.*, vol. 9, no. 3, p. 230, 2010.

[9] C.-F. Pai, L. Liu, Y. Li, H. W. Tseng, D. C. Ralph, and R. A. Buhrman, "Spin transfer torque devices utilizing the giant spin Hall effect of tungsten," *Appl. Phys. Lett.*, vol. 101, no. 12, 2012.

[10] M. Cubukcu, O. Boulle, M. Drouard, K. Garello, C. Onur Avci, I. Mihai Miron, J. Langer, B. Ocker, P. Gambardella, and G. Gaudin, "Spin-orbit torque magnetization switching of a three-terminal perpendicular magnetic tunnel junction," *Appl. Phys. Lett.*, vol. 104, no. 4, p. 042406, 2014.

[11] S. V. Aradhya, G. E. Rowlands, J. Oh, D. C. Ralph, and R. A. Buhrman, "Nanosecond-timescale low energy switching of in-plane magnetic tunnel junctions through dynamic oersted-field-assisted spin Hall effect," *Nano Lett.*, vol. 16, no. 10, pp. 5987–5992, 2016.

[12] M.-H. Nguyen, S. Shi, G. E. Rowlands, S. V. Aradhya, C. L. Jermain, D. Ralph, and R. Buhrman, "Efficient switching of 3-terminal magnetic tunnel junctions by the giant spin Hall effect of {Pt} _ {85} {Hf} _ {15} alloy," *arXiv preprint arXiv:1801.00411*, 2018.

[13] W. Kong, Y. Ji, X. Zhang, H. Wu, Q. Zhang, Z. Yuan, C. Wan, X. Han, T. Yu, K. Fukuda, *et al.*, "Field-free spin Hall effect driven magnetization switching in pd/co/irmn exchange coupling system," *Appl. Phys. Lett.*, vol. 109, no. 13, p. 132402, 2016.

[14] T. Taniguchi, J. Grollier, and M. D. Stiles, "Spin-transfer torques generated by the anomalous Hall effect and anisotropic magnetoresistance," *Phys. Rev. Appl.*, vol. 3, no. 4, p. 044001, 2015.

[15] M. Dyakonov and V. Perel, "Current-induced spin orientation of electrons in semiconductors," *Phys. Lett. A*, vol. 35, no. 6, pp. 459 – 460, 1971.

[16] J. E. Hirsch, "Spin Hall effect," *Phys. Rev. Lett.*, vol. 83, pp. 1834–1837, Aug 1999.

[17] R. Karplus and J. M. Luttinger, "Hall effect in ferromagnetics," *Phys. Rev.*, vol. 95, pp. 1154–1160, Sep 1954.

[18] J. Smit, "The spontaneous Hall effect in ferromagnetics i," *Physica*, vol. 21, no. 6-10, pp. 877–887, 1955.

[19] J. Smit, "The spontaneous Hall effect in ferromagnetics ii," *Physica*, vol. 24, no. 1-5, pp. 39–51, 1958.

[20] L. Berger, "Side-jump mechanism for the Hall effect of ferromagnets," *Phys. Rev. B*, vol. 2, pp. 4559–4566, Dec 1970.

[21] A. Crépieux and P. Bruno, "Theory of the anomalous Hall effect from the kubo formula and the dirac equation," *Phys. Rev. B*, vol. 64, p. 014416, Jun 2001.

[22] M. Isasa, E. Villamor, L. E. Hueso, M. Gradhand, and F. Casanova, "Temperature dependence of spin diffusion length and spin Hall angle in Au and Pt," *Phys. Rev. B*, vol. 91, p. 024402, Jan 2015.

[23] Y. Ji, A. Hoffmann, J. S. Jiang, and S. D. Bader, "Spin injection, diffusion, and detection in lateral spin-valves," *Appl. Phys. Lett.*, vol. 85, no. 25, pp. 6218–6220, 2004.

[24] J. Ku, J. Chang, S. Han, J. Ha, and J. Eom, "Electrical spin injection and accumulation in ferromagnetic/au/ferromagnetic lateral spin valves," *J. Appl. Phys.*, vol. 99, no. 8, p. 08H705, 2006.

[25] P. Laczkowski, L. Vila, V.-D. Nguyen, A. Marty, J.-P. Attané, H. Jaffrès, J.-M. George, and A. Fert, "Enhancement of the spin signal in permalloy/gold multiterminal nanodevices by lateral confinement," *Phys. Rev. B*, vol. 85, p. 220404, Jun 2012.

[26] M. Morota, Y. Niimi, K. Ohnishi, D. H. Wei, T. Tanaka, H. Kontani, T. Kimura, and Y. Otani, "Indication of intrinsic spin Hall effect in 4*d* and 5*d* transition metals," *Phys. Rev. B*, vol. 83, p. 174405, May 2011.

[27] V. Vlaminck, J. E. Pearson, S. D. Bader, and A. Hoffmann, "Dependence of spin-pumping spin Hall effect measurements on layer thicknesses and stacking order," *Phys. Rev. B*, vol. 88, p. 064414, Aug 2013.

[28] L. Liu, R. Buhrman, and D. Ralph, "Review and analysis of measurements of the spin Hall effect in platinum," *arXiv preprint arXiv:1111.3702*, 2011.

[29] M. Obstbaum, M. Härtinger, H. G. Bauer, T. Meier, F. Swientek, C. H. Back, and G. Woltersdorf, "Inverse spin Hall effect in $ni_{81}fe_{19}$/normal-metal bilayers," *Phys. Rev. B*, vol. 89, p. 060407, Feb 2014.

[30] A. Azevedo, L. H. Vilela-Leão, R. L. Rodríguez-Suárez, A. F. Lacerda Santos, and S. M. Rezende, "Spin pumping and anisotropic magnetoresistance voltages in magnetic bilayers: Theory and experiment," *Phys. Rev. B*, vol. 83, p. 144402, Apr 2011.

[31] J.-C. Rojas-Sánchez, N. Reyren, P. Laczkowski, W. Savero, J.-P. Attané, C. Deranlot, M. Jamet, J.-M. George, L. Vila, and H. Jaffrès, "Spin pumping and inverse spin Hall effect in platinum: The essential role of spin-memory loss at metallic interfaces," *Phys. Rev. Lett.*, vol. 112, p. 106602, Mar 2014.

[32] W. Zhang, V. Vlaminck, J. E. Pearson, R. Divan, S. D. Bader, and A. Hoffmann, "Determination of the Pt spin diffusion length by spin-pumping and spin Hall effect," *Appl. Phys. Lett.*, vol. 103, no. 24, p. 242414, 2013.

[33] A. Mellnik, J. Lee, A. Richardella, J. Grab, P. Mintun, M. H. Fischer, A. Vaezi, A. Manchon, E.-A. Kim, N. Samarth, *et al.*, "Spin-transfer torque generated by a topological insulator," *Nature*, vol. 511, no. 7510, p. 449, 2014.

[34] N. Reynolds, P. Jadaun, J. T. Heron, C. L. Jermain, J. Gibbons, R. Collette, R. Buhrman, D. Schlom, and D. Ralph, "Spin Hall torques generated by rare-earth thin films," *Phys. Rev. B*, vol. 95, no. 6, p. 064412, 2017.

[35] D. Xiao, M.-C. Chang, and Q. Niu, "Berry phase effects on electronic properties," *Rev. Mod. Phys.*, vol. 82, no. 3, p. 1959, 2010.

[36] T. Tanaka, H. Kontani, M. Naito, T. Naito, D. S. Hirashima, K. Yamada, and J. Inoue, "Intrinsic spin Hall effect and orbital Hall effect in 4*d* and 5*d* transition metals," *Phys. Rev. B*, vol. 77, p. 165117, 2008.

[37] M. Gradhand, D. V. Fedorov, P. Zahn, and I. Mertig, "Extrinsic spin Hall effect from first principles," *Phys. Rev. Lett.*, vol. 104, p. 186403, May 2010.

[38] Y. Niimi, Y. Kawanishi, D. H. Wei, C. Deranlot, H. X. Yang, M. Chshiev, T. Valet, A. Fert, and Y. Otani, "Giant spin Hall effect induced by skew scattering from bismuth impurities inside thin film cubi alloys," *Phys. Rev. Lett.*, vol. 109, p. 156602, Oct 2012.

[39] Y. Niimi, M. Morota, D. H. Wei, C. Deranlot, M. Basletic, A. Hamzic, A. Fert, and Y. Otani, "Extrinsic spin Hall effect induced by iridium impurities in copper," *Phys. Rev. Lett.*, vol. 106, p. 126601, Mar 2011.

[40] M. V. Berry, "Quantal phase factors accompanying adiabatic changes," *Proc. R. Soc. A*, vol. 392, p. 45, 1984.

[41] F. Pientka, *Geometrical Concepts in the band theory of solids*. University Halle-Wittenberg, 2010.

[42] R. Resta, "Theory of the electric polarization in crystals," *Ferroelectrics*, vol. 136, no. 1, pp. 51–55, 1992.

[43] R. D. King-Smith and D. Vanderbilt, "Theory of polarization of crystalline solids," *Phys. Rev. B*, vol. 47, pp. 1651–1654, Jan 1993.

[44] J. Sinova, D. Culcer, Q. Niu, N. A. Sinitsyn, T. Jungwirth, and A. H. MacDonald, "Universal intrinsic spin Hall effect," *Phys. Rev. Lett.*, vol. 92, p. 126603, Mar 2004.

[45] M. Marder, *Condensed Matter Physics*. John Wiley & Sons, Inc, 2010.

[46] M.-C. Chang and Q. Niu, "Berry curvature, orbital moment, and effective quantum theory of electrons in electromagnetic fields," *J. Phys.: Condens. Matter*, vol. 20, no. 19, p. 193202, 2008.

[47] D. Xiao, M.-C. Chang, and Q. Niu, "Berry phase effects on electronic properties," *Rev. Mod. Phys.*, vol. 82, no. 3, p. 1959, 2010.

[48] M. Gradhand, D. Fedorov, F. Pientka, P. Zahn, I. Mertig, and B. Györffy, "First-principle calculations of the berry curvature of bloch states for charge and spin transport of electrons," *J. Phys.: Condens. Matter*, vol. 24, no. 21, p. 213202, 2012.

[49] R. Shindou and K.-I. Imura, "Noncommutative geometry and non-abelian berry phase in the wave-packet dynamics of bloch electrons," *Nucl. Phys. B*, vol. 720, no. 3, pp. 399–435, 2005.

[50] J. Franklin, *Advanced Mechanics and General Relativity*. Cambridge University Press, 2010.

[51] M. Gradhand, D. V. Fedorov, F. Pientka, P. Zahn, I. Mertig, and B. L. Györffy, "Calculating the berry curvature of bloch electrons using the KKR method," *Phys. Rev. B*, vol. 84, p. 075113, Aug 2011.

[52] A. Vernes, B. L. Györffy, and P. Weinberger, "Spin currents, spin-transfer torque, and

spin-Hall effects in relativistic quantum mechanics," *Phys. Rev. B*, vol. 76, p. 012408, Jul 2007.

[53] T. Tanaka and H. Kontani, "Intrinsic spin and orbital Hall effects in heavy-fermion systems," *Phys. Rev. B*, vol. 81, p. 224401, Jun 2010.

[54] K. Gottfried and T.-M. Yan, *Quantum mechanics: fundamentals*. Springer Science & Business Media, 2013.

[55] M. Seemann, D. Ködderitzsch, S. Wimmer, and H. Ebert, "Symmetry-imposed shape of linear response tensors," *Phys. Rev. B*, vol. 92, no. 15, p. 155138, 2015.

[56] Y. K. Kato, R. C. Myers, A. C. Gossard, and D. D. Awschalom, "Observation of the spin Hall effect in semiconductors," *Science*, vol. 306, no. 5703, pp. 1910–1913, 2004.

[57] C. Stamm, C. Murer, M. Berritta, J. Feng, M. Gabureac, P. M. Oppeneer, and P. Gambardella, "Magneto-optical detection of the spin Hall effect in Pt and W thin films," *Phys. Rev. Lett.*, vol. 119, no. 8, p. 087203, 2017.

[58] D. MacNeill, G. Stiehl, M. Guimaraes, R. Buhrman, J. Park, and D. Ralph, "Control of spin–orbit torques through crystal symmetry in wte 2/ferromagnet bilayers," *Nat. Phys.*, vol. 13, no. 3, p. 300, 2017.

[59] D. MacNeill, G. M. Stiehl, M. H. Guimarães, N. D. Reynolds, R. A. Buhrman, and D. C. Ralph, "Thickness dependence of spin-orbit torques generated by wte 2," *Phys. Rev. B*, vol. 96, no. 5, p. 054450, 2017.

[60] J. C. Sankey, Y.-T. Cui, J. Z. Sun, J. C. Slonczewski, R. A. Buhrman, and D. C. Ralph, "Measurement of the spin-transfer-torque vector in magnetic tunnel junctions," *Nat. Phys.*, vol. 4, no. 1, p. 67, 2008.

[61] H. Kubota, A. Fukushima, K. Yakushiji, T. Nagahama, S. Yuasa, K. Ando, H. Maehara, Y. Nagamine, K. Tsunekawa, D. D. Djayaprawira, *et al.*, "Quantitative measurement of voltage dependence of spin-transfer torque in MgO-based magnetic tunnel junctions," *Nat. Phys.*, vol. 4, no. 1, p. 37, 2008.

[62] A. Mellnik, *Measurements of Spin Torques Generated by Topological Insulators and Heavy Metals*. PhD thesis, Cornell University, 2015.

[63] J. N. Kupferschmidt, S. Adam, and P. W. Brouwer, "Theory of the spin-torque-driven ferromagnetic resonance in a ferromagnet/normal-metal/ferromagnet structure," *Phys. Rev. B*, vol. 74, p. 134416, Oct 2006.

[64] J. C. Slonczewski, "Current-driven excitation of magnetic multilayers," *J. Magn. Magn. Mater.*, vol. 159, no. 1-2, pp. L1–L7, 1996.

[65] C.-F. Pai, Y. Ou, L. H. Vilela-Leão, D. C. Ralph, and R. A. Buhrman, "Dependence of the efficiency of spin Hall torque on the transparency of Pt/ferromagnetic layer interfaces," *Phys. Rev. B*, vol. 92, p. 064426, Aug 2015.

[66] X. Fan, A. R. Mellnik, W. Wang, N. Reynolds, T. Wang, H. Celik, V. O. Lorenz, D. C. Ralph, and J. Q. Xiao, "All-optical vector measurement of spin-orbit-induced torques using both polar and quadratic magneto-optic kerr effects," *Appl. Phys. Lett.*, vol. 109, no. 12, p. 122406, 2016.

[67] J. Kerr, "Xliii. on rotation of the plane of polarization by reflection from the pole of a magnet," *The London, Edinburgh, and Dublin Philosophical Magazine and Journal of Science*, vol. 3, no. 19, pp. 321–343, 1877.

[68] J. Zak, E. Moog, C. Liu, and S. Bader, "Universal approach to magneto-optics," *J. Magn. Magn. Mater.*, vol. 89, no. 1-2, pp. 107–123, 1990.

[69] Z. Qiu and S. D. Bader, "Surface magneto-optic Kerr effect (SMOKE)," *J. Magn. Magn. Mater.*, vol. 200, no. 1-3, pp. 664–678, 1999.

[70] H. L. Wang, C. H. Du, Y. Pu, R. Adur, P. C. Hammel, and F. Y. Yang, "Scaling of spin Hall angle in 3d, 4d, and 5d metals from $y_3fe_5o_{12}$/metal spin pumping," *Phys. Rev. Lett.*, vol. 112, p. 197201, May 2014.

[71] C. Du, H. Wang, F. Yang, and P. C. Hammel, "Systematic variation of spin-orbit coupling with *d*-orbital filling: Large inverse spin Hall effect in 3*d* transition metals," *Phys. Rev. B*, vol. 90, p. 140407, Oct 2014.

[72] H. Wang, C. Du, P. Chris Hammel, and F. Yang, "Spin current and inverse spin Hall effect in ferromagnetic metals probed by y3fe5o12-based spin pumping," *Appl. Phys. Lett.*, vol. 104, no. 20, 2014.

[73] C.-F. Pai, M. Mann, A. J. Tan, and G. S. D. Beach, "Determination of spin torque efficiencies in heterostructures with perpendicular magnetic anisotropy," *Phys. Rev. B*, vol. 93, p. 144409, Apr 2016.

[74] E. M. Chudnovsky, "Intrinsic spin Hall effect in noncubic crystals," *Phys. Rev. B*, vol. 80, p. 153105, Oct 2009.

[75] A. Fert and P. M. Levy, "Spin Hall effect induced by resonant scattering on impurities in metals," *Phys. Rev. Lett.*, vol. 106, p. 157208, Apr 2011.

[76] Y. Niimi, H. Suzuki, Y. Kawanishi, Y. Omori, T. Valet, A. Fert, and Y. Otani, "Extrinsic spin Hall effects measured with lateral spin valve structures," *Phys. Rev. B*, vol. 89, p. 054401, Feb 2014.

[77] J. Smit, "The spontaneous Hall effect in ferromagnets ii," *Physica*, vol. 24, p. 39, 1958.

[78] T. Tanaka and H. Kontani, "Extrinsic spin Hall effect due to transition-metal impurities," *Prog. of Theor. Phys.*, vol. 128, p. 805, 2012.

[79] J. Sinova, S. O. Valenzuela, J. Wunderlich, C. H. Back, and T. Jungwirth, "Spin Hall effects," *Rev. Mod. Phys.*, vol. 87, pp. 1213–1260, Oct 2015.

[80] H. Kontani, T. Tanaka, D. S. Hirashima, K. Yamada, and J. Inoue, "Giant orbital Hall effect in transition metals: Origin of large spin and anomalous Hall effects," *Phys. Rev. Lett.*, vol. 102, p. 016601, Jan 2009.

[81] C. Du, H. Wang, P. C. Hammel, and F. Yang, "Y3fe5o12 spin pumping for quantitative understanding of pure spin transport and spin Hall effect in a broad range of materials (invited)," *J. Appl. Phys.*, vol. 117, no. 17, p. 172603, 2015.

[82] B. Johansson, "Energy position of $4f$ levels in rare-earth metals," *Phys. Rev. B*, vol. 20, pp. 1315–1327, Aug 1979.

[83] P. Strange, A. Svane, W. Temmerman, Z. Szotek, and H. Winter, "Understanding the valency of rare earths from first-principles theory," *Nature*, vol. 399, pp. 756–758, May 1999.

[84] G. Meurant, *Vacuum Physics and Technology*. Methods in Experimental Physics, Elsevier Science, 1980.

[85] K. Ando, S. Takahashi, K. Harii, K. Sasage, J. Ieda, S. Maekawa, and E. Saitoh, "Electric manipulation of spin relaxation using the spin Hall effect," *Phys. Rev. Lett.*, vol. 101, p. 036601, Jul 2008.

[86] K. Ueda, C.-F. Pai, A. J. Tan, M. Mann, and G. S. D. Beach, "Effect of rare earth metal on the spin-orbit torque in magnetic heterostructures," *Appl. Phys. Lett.*, vol. 108, no. 23, p. 232405, 2016.

[87] W. Bailey, P. Kabos, F. Mancoff, and S. Russek, "Control of magnetization dynamics in ni81fe19 thin films through the use of rare-earth dopants," *IEEE Trans. Magn.*, vol. 37, pp. 1749–1754, Jul 2001.

[88] S. G. Reidy, L. Cheng, and W. E. Bailey, "Dopants for independent control of precessional frequency and damping in ni81fe19 (50 nm) thin films," *Appl. Phys. Lett.*, vol. 82, no. 8, p. 1254, 2003.

[89] C.-F. Pai, M.-H. Nguyen, C. Belvin, L. H. Vilela-Leão, D. Ralph, and R. Buhrman, "Enhancement of perpendicular magnetic anisotropy and transmission of spin-Hall-effect-induced spin currents by a Hf spacer layer in W/Hf/CoFeB/MgO layer structures," *Appl. Phys. Lett.*, vol. 104, no. 8, p. 082407, 2014.

[90] M. Akyol, J. G. Alzate, G. Yu, P. Upadhyaya, K. L. Wong, A. Ekicibil, P. Khalili Amiri, and K. L. Wang, "Effect of the oxide layer on current-induced spin-orbit torques in Hf—CoFeB—MgO and Hf—CoFeB—TaOx structures," *Appl. Phys. Lett.*, vol. 106, no. 3, p. 032406, 2015.

[91] M. Akyol, G. Yu, J. G. Alzate, P. Upadhyaya, X. Li, K. L. Wong, A. Ekicibil, P. Khalili Amiri, and K. L. Wang, "Current-induced spin-orbit torque switching of perpendicularly magnetized Hf—CoFeB—MgO and Hf—CoFeB—TaOx structures," *Appl. Phys. Lett.*, vol. 106, no. 16, p. 162409, 2015.

[92] R. Ramaswamy, X. Qiu, T. Dutta, S. D. Pollard, and H. Yang, "Hf thickness dependence of spin-orbit torques in Hf/CoFeB/MgO heterostructures," *Appl. Phys. Lett.*, vol. 108, no. 20, p. 202406, 2016.

[93] B. Min, H. Jansen, T. Oguchi, and A. Freeman, "Local density total energy description of ground and excited state properties of the rare earth metals," *J. Magn. Magn. Mater.*, vol. 61, no. 1, pp. 139 – 150, 1986.

[94] O. Eriksson, M. Brooks, and B. Johansson, "Calculated cohesive properties of lanthanide and lanthanide-like actinide elements," *J. Less-Common Met.*, vol. 158, no. 2, pp. 207 – 220, 1990.

[95] P. Strange, A. Svane, W. M. Temmerman, Z. Szotek, and H. Winter, "Understanding the valency of rare earths from first-principles theory," *Nature*, vol. 399, pp. 756–758, 06 1999.

[96] M. Topsakal and R. Wentzcovitch, "Accurate projected augmented wave (PAW) datasets for rare-earth elements (RE=La–Lu)," *Comp. Mater. Sci.*, vol. 95, pp. 263–270, 2014.

[97] D. van der Marel and G. A. Sawatzky, "Electron-electron interaction and localization in *d* and *f* transition metals," *Phys. Rev. B*, vol. 37, pp. 10674–10684, Jun 1988.

[98] H. Kontani, M. Naito, D. S. Hirashima, K. Yamada, and J. Inoue, "Study of intrinsic spin and orbital Hall effects in Pt based on a (6s, 6p, 5d) tight-binding model," *J. Phys. Soc. Jpn.*, vol. 76, no. 10, p. 103702, 2007.

[99] S. Chatterjee, S. H. Sung, D. J. Baek, L. F. Kourkoutis, D. G. Schlom, and K. M. Shen, "Epitaxial growth and electronic properties of mixed valence YbAl3 thin films," *J. Appl. Phys.*, vol. 120, no. 3, p. 035105, 2016.

[100] A. Cornelius, J. Lawrence, T. Ebihara, P. Riseborough, C. Booth, M. Hundley, P. Pagliuso, J. Sarrao, J. Thompson, M. Jung, *et al.*, "Two energy scales and slow crossover in YbAl3," *Phys. Rev. Lett.*, vol. 88, no. 11, p. 117201, 2002.

[101] T. Ebihara, E. Bauer, A. Cornelius, J. LawrencYbAl3e, N. Harrison, J. Thompson, J. Sarrao, M. Hundley, and S. Uji, "Dependence of the effective masses in YbAl3 on magnetic field and disorder," *Phys. Rev. Lett.*, vol. 90, no. 16, p. 166404, 2003.

[102] S. Chatterjee, J. P. Ruf, H. I. Wei, K. D. Finkelstein, D. G. Schlom, and K. M. Shen, "Lifshitz transition from valence fluctuations in YbAl3," *Nat. Commun.*, vol. 8, no. 1, p. 852, 2017.

[103] L. Tjeng, S.-J. Oh, E.-J. Cho, H.-J. Lin, C. Chen, G.-H. Gweon, J.-H. Park, J. Allen, T. Suzuki, M. Makivić, *et al.*, "Temperature dependence of the Kondo resonance in YbAl3," *Phys. Rev. Lett.*, vol. 71, no. 9, p. 1419, 1993.

[104] J. Lawrence, G. Kwei, P. Canfield, J. DeWitt, and A. Lawson, "L iii x-ray absorption in Yb compounds: temperature dependence of the valence," *Phys. Rev. B*, vol. 49, no. 3, p. 1627, 1994.

[105] L. Moreschini, C. Dallera, J. Joyce, J. Sarrao, E. Bauer, V. Fritsch, S. Bobev, E. Carpene, S. Huotari, G. Vankó, *et al.*, "Comparison of bulk-sensitive spectroscopic probes of Yb valence in Kondo systems," *Phys. Rev. B*, vol. 75, no. 3, p. 035113, 2007.

[106] Y.-f. Yang and D. Pines, "Universal behavior in heavy-electron materials," *Phys. Rev. Lett.*, vol. 100, no. 9, p. 096404, 2008.

[107] Y.-f. Yang, Z. Fisk, H.-O. Lee, J. Thompson, and D. Pines, "Scaling the Kondo lattice," *Nature*, vol. 454, no. 7204, p. 611, 2008.

[108] Y.-f. Yang and D. Pines, "Emergent states in heavy-electron materials," *Proceedings of the National Academy of Sciences*, vol. 109, no. 45, pp. E3060–E3066, 2012.

[109] A. Hiess, J. Boucherle, F. Givord, and P. Canfield, "Magnetic susceptibility and magnetization measurements of an YbAl3 single crystal for groundstate investigations," *Journal of alloys and compounds*, vol. 224, no. 1, pp. 33–35, 1995.

[110] H. Suhl, "Ferromagnetic resonance in nickel ferrite between one and two kilomegacycles," *Phys. Rev.*, vol. 97, no. 2, p. 555, 1955.

[111] R. Meckenstock, K. Harms, O. Von Geisau, and J. Pelzl, "Temperature-dependent FMR investigations on epitaxial Fe (001) films with different thicknesses," *J. Magn. Magn. Mater.*, vol. 148, no. 1-2, pp. 139–140, 1995.

[112] M. Hayashi, J. Kim, M. Yamanouchi, and H. Ohno, "Quantitative characterization of the spin-orbit torque using harmonic Hall voltage measurements," *Phys. Rev. B*, vol. 89, p. 144425, Apr 2014.

[113] C. O. Avci, K. Garello, M. Gabureac, A. Ghosh, A. Fuhrer, S. F. Alvarado, and P. Gambardella, "Interplay of spin-orbit torque and thermoelectric effects in ferromagnet/normal-metal bilayers," *Phys. Rev. B*, vol. 90, p. 224427, Dec 2014.

[114] W. Sänger and J. Voitländer, "Interpretation of the magnetic susceptibility of Pd and Pt by using the spin fluctuation model," *Z. Phys. B: Condens. Matter*, vol. 38, no. 2, pp. 133–138, 1980.